Investigation of the Mechanisms and Control Measures for Fireside Corrosion in Eskom Fossil Fuel Boilers

MSc DISSERTATION

Prepared by

Kediemetse Gloria Moloko (9808755G)

Submitted to

School of Chemical and Metallurgical Engineering, Faculty of Engineering and the Built Environment, University of the Witwatersrand, Johannesburg, South Africa

02 October 2019

DECLARATION

I declare that this dissertation is entirely my own work and that all sources, used or referred to, have, by means of complete references, been listed and acknowledged. It is being submitted for the degree of Master of Science in Engineering to the University of the Witwatersrand, Johannesburg. It has not been submitted before for any degree or examination in any other University.

Signature: K. G. Moloko

……

02 October 2019

ABSTRACT

Fireside corrosion in fossil-fired boilers is still amongst the damage mechanisms that contribute toward the most boiler tube failures. It was first identified in South African power generation utilities in the early 1990s when a number of coal-fired subcritical boilers (600 MW power generation per Unit) experienced tube failures on the furnace walls. Molten alkali sulphate corrosion and sulphidation have been identified as possible mechanisms through several failure investigations, but not ascertained. This study aims to close this gap by conducting an in- depth investigation into the mechanism underwhich fireside corrosion occurs on the furnace wall tubes, and the conditions of the furnace that enable this type of attack in Eskom coal fired 600 MW subcritical boilers. This research describes the process followed in sampling the furnace wall tubes from three coal-fired power stations (A, B and C) subjected to fireside corrosion, as well as outlining techniques employed in analyzing the fireside deposits and the findings thereof. SEM-EDS analysis revealed high concentrations of oxygen, iron and sulphur. QEMSCAN and XRD revealed coexistence of Fe-oxide and Fe-sulphide in a form of Fe_3O_4 and Fe_2O_3, FeS, and FeS_2. DTA showed thermal activities at temperatures of 500-600°C, 900-1100°C and 1100-1250°C which are associated with FeS_2 oxidation into FeS and Fe_2O_3, which occurs between 475°C and 525°C, formation of aluminosilicates such as mullite at 925°C to 1100°C and the melting of FeS around 1190°C. The coexistence of FeS and iron oxide in the fireside deposit of the tubing is indicative of the substoichiometric conditions in the furnace and on the surface of the boiler tubes. The detection of pyrite in the fireside deposit suggests that the pyrite is not completely burnt which points to poor combustion process. This was confirmed by the gas analysis of Unit 1 of station A where very high levels of CO were measured at the furnace wall ($\geq$ 14000 ppm) and furnace exit ($\geq$ 3500 ppm). The high CO concentrations are indicative of limited combustion caused by limited O_2. These reducing conditions promote formation of FeS rich deposits, which are evident on all analysed tubes. The absence of primary elements that form alkali sulphates, viz. sodium and potassium, eliminates the involvement of molten alkali sulphates but affirms that the type of fireside corrosion taking place on furnace walls from power stations A, B and C is by sulphidation due to iron-sulphide-rich deposition. The mitigation of sulphidation fireside corrosion can be achieved through better control of the combustion process. In addition, thermal spray coatings and weld overlays have proven to protect the tubes from fireside corrosion for a specific period of time.

ACKNOWLEDGEMENTS

The author wishes to thank the following people for their contribution:

My supervisor

My supervisor, Professor Josias Van Der Merwe, for the support and guidance received throughout the time span of this research. I will remain grateful to you for your effective mentorship, dedication and supervision.

Technical assistance

Mr Keith Northcott for his technical support and motivation into the sponsorship of my studies.
Dr Thobeka Pete and Ms Mantsaye Raseroka for reviewing my reports and your motivation.
Dr Fortune Moyo for assistance with XRD analysis.
Dr Chris Van Aphen for assistance with QEMSCAN.
Ms Govishnee Ramharakan for assistance with SEM.

Institutions

The management of Eskom Research, Testing and Development (RT&D) for allowing and sponsoring this study.
RT&D for providing facilities and also performing various analyses.
University of Pretoria for performing DTA.

My family

Thanks to my mother for your love and support. Thanks to my husband for believing in me and being my pillar in times of need. Thanks to my children for being patient and understanding. Thanks to Alice for stepping in to care for my children in times of need. I love and appreciate all of you.

TABLE OF CONTENTS

LIST OF FIGURES

LIST OF TABLES

LIST OF EQUATIONS

LIST OF ACRONYMS

ASTM	American Society for Testing and Materials
BS EN	British Standard European Norm
CFD	Combustion Fluid Dynamic
DIN	Deutches Institut fur Normung (which means German Institute for Standardization)
DTA	Differential Thermal Analysis
DW	Division Wall
EDS	Energy Dispersive X-ray Spectroscopy
FA	Fly ash
FEL-QUANTA	Field Electron and Ion Quantification
FW	Front Wall
HV	Hardness Vickers
MW	Mega Watt
NDE	Non Destructive Examination
PF	Pulverized Fuel
QEMSCAN	Qualitative Evaluation Mineralogy Scanner
SEM	Scanning Electron Microscopy
UT	Ultrasonic Testing
UTS	Ultimate Tensile Strength
XRD	X-Ray Diffraction

1. INTRODUCTION

1.1 FOSSIL FUEL FIRED POWER GENERATION INDUSTRY

Fossil fuels are still one of the major sources of energy in our society because of their capacity to generate huge amounts of electricity. However, unforeseen failures in boilers cause them to shut down and stop electricity generation. Main failures in boilers stem from severe damage in boiler tubes which can be affected by the tube material, tube position, temperature, pressure and chemical composition of the fossil fuel (Asnavandi et al., 2017, Harding and O'Connor, 2007).

Statistics on thermal power plant equipment accidents in China in 1992 showed that accidents caused by the bursting of furnace wall tubes accounted for 27.8% of the total boiler accidents (Yu et al., 2017, Wu, 2003). These numbers have been seen to increase as the capacity of coal fired boilers increases. Meanwhile, the environmental pollution generated from coal-fired power plant is now drawing attention all over the world, and a strict limitation has been set for the NOx emissions. To comply with air pollution control laws, coal fired power generation industries find it is necessary to apply technologies that reduce the emissions of the NOx and SOx. Low excess air combustion and two-stage combustion are commonly applied as means of realizing low-NOx combustion (Shirai et al., 2012). However, a strong reducing atmosphere is formed in the region between burners and airports in the case of two-stage combustion. This atmosphere promotes the formation of hydrogen sulphide (H_2S), which causes sulphidation corrosion at the boiler wall (Kihara et al., 1998, Morinaga et al., 2010). To control H_2S formation, one strategy is to raise the excess air ratio and another is to lower the two-stage combustion ratio, however, NOx emission increases in both cases (Shirai et al., 2012).

Co-firing of biomass with coal is amongst the techniques considered for reduction of NOx and SOx. Generally, biomass has lower sulphur levels than coal; therefore co-firing of coal with biomass will result in reduced sulphur oxides (SOx) levels in the combustion gases. Syed et al. (2011) found that compared to firing coal alone, co-firing coal and biomass can cause significant changes in the chemistry of the flue gas stream and the deposits that form on the

surfaces of heat exchangers, which can in turn lead to increased corrosion damage to the heat exchangers.

From literature, as presented above, the problem of fireside corrosion in fossil fuel fired power generation industries is likely to exacerbate with introduction of NOx and SOx reducing technologies. The introduction of supercritical coal-fired boilers as means of achieving high generation of electricity has the likelihood of increasing the degree/magnitude of fireside corrosion due to increased tube temperatures. It is that the effect of fireside corrosion will not be limited to historically conventional coal fired power stations but will still exist in the future coal fired power generation.

1.2 FIRESIDE CORROSION

Fireside corrosion is the metal loss of tubes due to chemical attack on the furnace of fireside of heat exchanging surfaces in fossil fuel-fired furnaces. It is characterized by the relatively high temperatures and the unique environment encountered in the furnaces such as the formation of slagging and fouling. The corrosive environment in the furnace is brought about by the complex interaction of the combustion gases with temperature varying between 400 and 1200°C (Syed et al., 2011), the distribution of pulverized fuel, through elements released from the fuel, and the type and nature of the ash being carried over in the gas stream, together with the materials of construction of the boiler (Valero and Cortes, 1996).

Fireside corrosion in boilers is commonly divided into two categories by location namely waterwall corrosion in the lower furnace and fuel ash corrosion of superheaters in the upper furnace. The mechanism of fireside corrosion depends on the fuel composition, firing conditions (gas and metal temperatures) and the resultant local chemistry of combustion gases and deposits. Fireside corrosion is a detrimental form of corrosion, if undetected it can result in the disruption of the normally protective oxide layer, leading potentially to rapid corrosion and wall thinning, eventually followed by the catastrophic rupture of high pressure tubing, causing extensive damage to the surrounding plant. Coal composition and the subsequent release of gaseous, molten, or solid

components via the combustion process are primary determinants of the potential severity of fireside corrosion.

Gaseous species released by the combustion of coal contain a number of potential corrodents. The most important are (i) sulphur, present as sulphur dioxide, sulphur trioxide, or as hydrogen sulphide, (ii) vapours of alkali metal salts in the form of oxides, hydroxides, or sulphates, and (iii) chlorine compounds. The condensable vapour species will deposit on contact with surfaces that are at temperatures lower than their respective condensation temperatures. This in turn results in the deposit of fly-ash and the accumulation of alkali and sulphur species. Ash deposits are formed from the coal minerals present in the fuel and the common minerals observed in coal are quartz, pyrite, kaolinite, illite and calcite (Harb and Smith, 2010). Knowing the mineralogy of the ash deposit is important in understanding the fireside deposits and their relation to corrosion. As identified by Dooley and McNaughton (2007), the nature of fireside corrosion process is commonly determined by:

i. Collecting and evaluating samples of fireside deposit. Analysis of the fireside deposit samples employs various techniques including Energy Dispersive X-ray Spectroscopy (EDS) to map out the concentration and pattern of elements within each layer of the fireside deposit, X-ray diffraction to determine what compounds are present, and either thermogravimetric or differential thermal analysis to determine the melting points of compounds in the fireside deposits.
ii. Monitoring corrosion online through the use of probes in susceptible locations.
iii. Evaluating the local environment in the furnace by monitoring for levels of O_2, CO, and H_2S, and performing field testing (e.g. gas analysis) to determine the combustion conditions in regions that are experiencing severe fireside corrosion.

1.3 BACKGROUND

Fireside corrosion of boiler heat exchanger materials was first recognized as a serious problem in the early 1940s when some of the power stations in the United States using pulverized coal fired furnaces, experienced an increased number of furnace wall tube failures (Harb and Smith, 2010).

For superheaters and reheaters this damage phenomenon has been an issue to the power generation industry since the 1950 (Shamanna and Schobert, 1997, Reid, 1971).

Fireside corrosion was first identified in South African power generation utilities in the early 1990s when a number of coal-fired subcritical boilers (600 MW power generation per Unit) experienced tube failures on the furnace walls. Since then it has been managed by measuring and monitoring the remaining wall thickness of the tubes during Unit outages by performing ultrasonic tests (UT). Despite the efforts to manage the effects of fireside corrosion, the level and extent of damage has been increasing and the existing control measure of replacing tubing below the minimum allowable wall thickness has become unsustainable due to high costs and extensive outage times. In addition, future trends such as (i) the installation of low NOx burners to control SOx and NOx emissions, and (ii) an increase in the steam temperatures to raise the thermal efficiency, i.e. through the construction of supercritical boilers, has the likelihood of further increasing fireside corrosion within Eskom boilers as has been seen in other power plants globally (Moore, 1995, Hatt, 1990).

1.4 RATIONALE FOR STUDY AND RESEARCH OBJECTIVES

Based on the limited knowledge and understanding regarding the actual mechanisms under which this phenomenon exhibits itself in Eskom boilers, in three power stations specifically, this research was initiated with the aim of conducting in-depth studies looking into the mechanism and potential drivers and contributors thereof as well as finding ways to manage this mechanism of attack effectively within Eskom fossil fuel boilers. The investigation was aimed at answering the questions on (i) whether the fireside corrosion attack within the boiler units of power stations A, B and C is by sulphidation and/or by formation of low melting alkali sulphate salts, (ii) what is the connection thereof to the environment in the furnace and (iii) the role that combustion process has played in promoting the existence of this fireside corrosion mechanism. Subsequently to the investigation of the fireside mechanism, the study involved a search into the control measures that are commercially available and applicable for power utility boiler tubes.

1.5 RESEARCH OBJECTIVES

The aim was met by evaluating the furnace wall tubes from the three power stations reported of fireside corrosion and analysing the chemistry, mineralogy and thermal properties of their fireside deposit as well as linking the results thereof to the relevant control measures in order to mitigate or effectively manage the fireside corrosion phenomenon.

2. LITERATURE REVIEW

2.1 INTRODUCTION

This literature review chapter includes a brief discussion on the basics of combustion process with the focus on pulverized fuel process and combustion of coal. An extensive corrosion review, particularly fireside corrosion and related reaction mechanisms, detection and analysis of fireside corrosion and factors affecting fireside corrosion, are the central point of this chapter. Mitigation and control measures for fireside corrosion are also reviewed in this chapter.

2.2 COMBUSTION PROCESS

2.2.1 Pulverised Fuel Process

Coal is supplied from the mine to the power station and stored in bunkers. In order to produce the desired coal particle size, coal is fed to the mills and mixed with hot primary air, 240 and 320ºC (Moore, 1995), to reduce moisture in the coal and crushed to the desired pulverized fuel (PF) size as shown in Figure 2.1. Pulverized coal increases the surface area which accelerates ignition and burnout; more intimate mixing of the fuel and air produces higher combustion efficiencies as reported by Reid (1984).

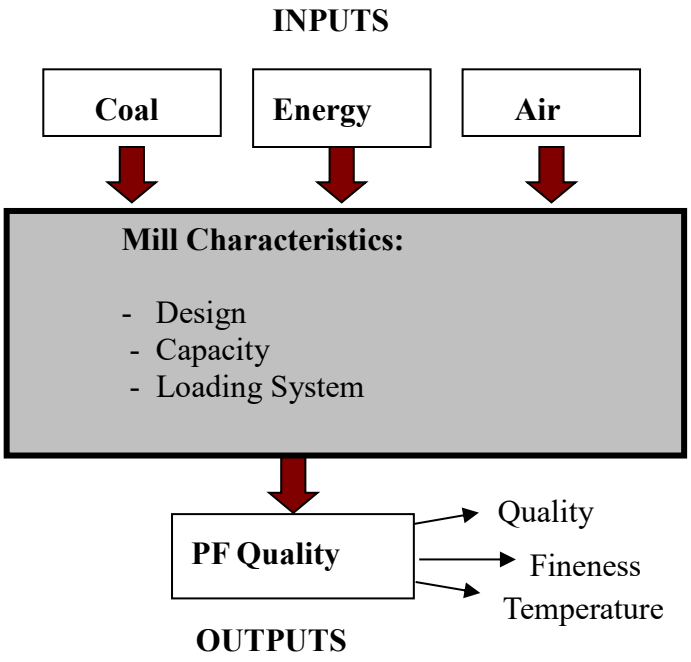

Figure 2.1: Typical milling process (Van Alphen C., 2016).

2.2.2 Coal Combustion

Once the coal has been milled it is then transported to the furnace. Fuel oil is introduced into the furnace to assist with ignition of the coal and producing the PF flame. The air/PF mixture is rapidly heated from ±80ºC to ignition temperature and fed into the furnace to stabilize the PF flame. After the fuel oil fires have been stopped, ignition of the PF flame is sustained by recirculating products of combustion (i.e. volatiles) and radiation. The ignition temperature is controlled by obtaining a balance of heat generation and heat loss to ignite char and surrounding wall tubes. Char burns for longer periods and is affected by the rank of coal and particle size. For an example bituminous coals burn longer than the lignites and coarse particulate will burn longer than a fine particulate as O_2 uptake increases with decreasing particle size (Reid, 1984). Figure 2.2 gives an overview of the combustion process involved in the coal-fired power station.

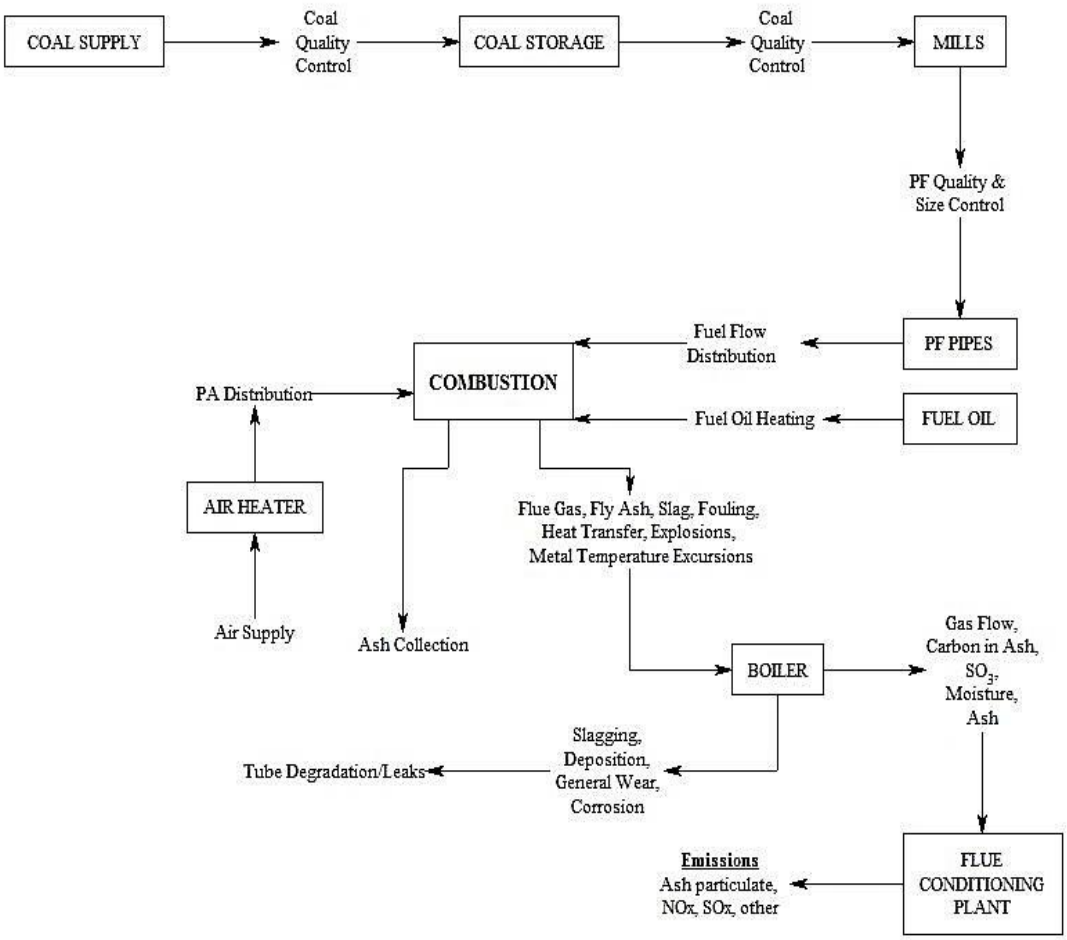

Figure 2.2: Combustion process overview.

The inorganic material in coal reacts, melts, vaporises, and eventually separates from burning coal particles to be entrained in fly ash, which can deposit on boiler tubes (Dooley and McNaughton, 2007). The low quality coal has a low heat value and high ash content and as the ash passes over into the gas stream causes slagging and fouling in furnace wall, superheater and reheater boiler tubes (Broodryk, 1995). In slagging, bonding is produced by melting or fusion of the ash particles, whereas in fouling, the ash particles are bound together by sulphate salts (Samms and Smith, 1961).

The amount and rate of fouling and slagging deposit accumulation and the tenacity of the deposits to remain stuck to the heat transfer surfaces are dependent on the size of the PF, chemistry and temperature of the entrained ash material and the properties of the deposition surface (Otsuka, 2010). The more fuel is pulverized, the higher content of smaller particles in the flue

gases and the higher probability of their deposition. The higher the temperature of the flue gas the more particles are carried by the gases, and the greater thermo-diffusion forces (Borio and Levasseur, 1986). The higher radiative heat flux in the boiler leads to the surface melting of the deposit which helps in sticking of new particles.

2.3 MATERIALS OF COAL FIRED BOILER TUBES

The role of a boiler tube is to transfer heat generated by the combustion process to the water and/or steam within the tube. The boiler consists of a complex network of pipes and tubes: the heat exchangers carry water that boils into a highly pressurised steam due to heat transfer from the hot flue gases around them. The hottest tubes in the steam boiler are superheaters and reheaters. The other, lower temperatures, heat exchangers in the boiler are the economizer and the water walls. Figure 2.3 is a representation of the coal-fired steam boiler. The power generation industry relies on various grades of steels for different heat-exchangers in the boiler depending on their location, operational temperature, conditions and other mechanical functions. In order to achieve its basic requirement, the tube must have sufficient mechanical strength to contain the internal pressure, as well as adequate resistance to corrosion on both fluid and fireside surfaces. These requirements must be continuously met over the required life of the boiler, usually well in excess of 100,000 operating hours (Bryers, 1995). Finally, economic considerations require that the cheapest adequate materials be used. Worldwide these demands are met by a number of international materials and design codes.

Material choice is a function of expected temperature of operation. Under normal conditions in furnace wall tubes for subcritical boilers, the steam-water temperature is limited to the saturation temperature for the given boiler pressure and thus the tube temperatures are typically less than 400°C (Bryers, 1995). In supercritical units, the furnace wall materials typically operate to slightly higher temperatures, 454°C. As a result, high temperature creep is not a consideration and furnace wall tubes are designed on the basis of short term tensile strength properties and for indefinite life, although in practice this goal is not always achievable. Plain carbon steels, such as 15Mo3, are most often used for furnace wall tubes in subcritical boilers , with low chromium ferritic steels such as 13CrMo4-4 and 10CrMo9-10, being used in some cases for reheater tube. The latter are

also the materials of choice for supercritical units. For supeheaters, high chromium austenitic alloys with high creep and oxidation resistance are used; these include grades of Cr-Mo-V such as X20CrMoV11-1 (Bryers, 1995). More recently, Ni-based alloys are being considered as candidate materials for the main superheaters and reheaters (Zhao et al., 2005) as the industry is moving towards higher performance targets (supercritical boilers with steam temperature ~700°C and pressure ~ 375 bars).

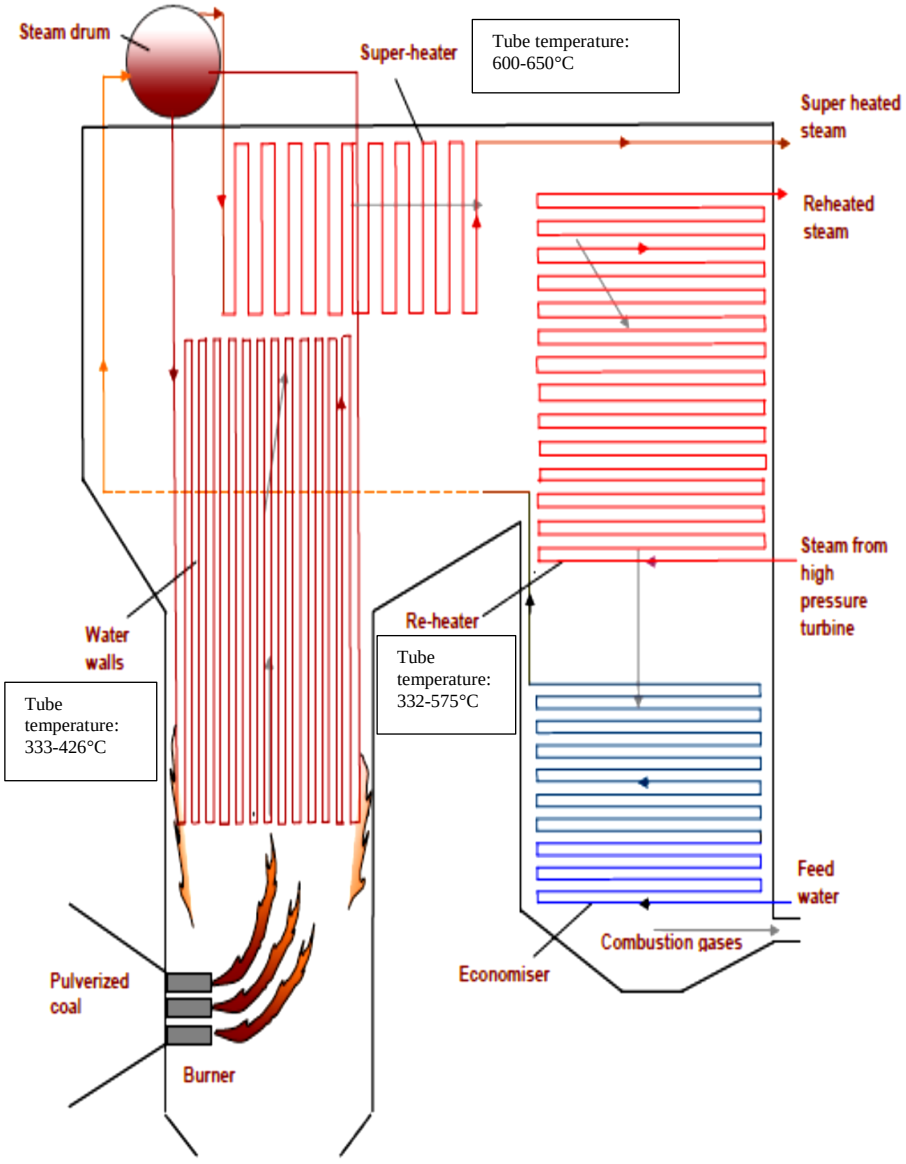

Figure 2.3: Schematic of coal-fired boiler (Syed et al., 2011).

2.4 FORMS OF FIRESIDE CORROSION

Fireside corrosion in boilers is commonly divided into two categories by location namely waterwall corrosion in the lower furnace and fuel ash corrosion of superheaters in the upper furnace as indicated in Figure 2.3. The mechanism of fireside corrosion depends on the fuel composition, firing conditions (gas and metal temperatures) and the resultant local chemistry of combustion gases and deposits. Gaseous species released by the combustion of coal contain a number of potential corrodents (Hatt, 1990) including i) sulphur, present as sulphur dioxide, sulphur trioxide or hydrogen sulphide, ii) vapours of alkali metal salts, and iii) chlorine compounds, particularly where coal has chlorine which is not the case in coal produced in South Africa. As a result, fireside corrosion has been associated with liquid and gas phase reactions, and corrosion by sulphide rich deposits.

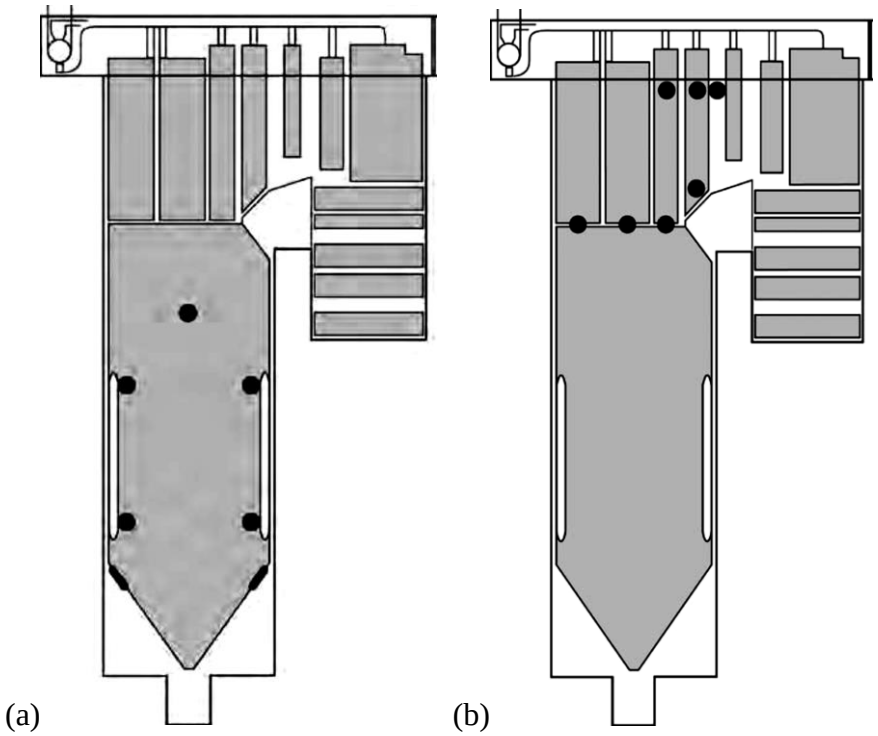

Figure 2.4: Steam generator side elevation showing areas susceptible to corrosion in the (a) furnace walls with tube temperatures of 333-426°C and (b) superheaters with tube temperatures of 600-650°C, (Dooley and McNaughton, 2007).

Figure 2.5 illustrates how the rate of corrosion varies with the gas temperature and how different types of corrosion are caused on different parts of the boiler when coal is used as a fuel.

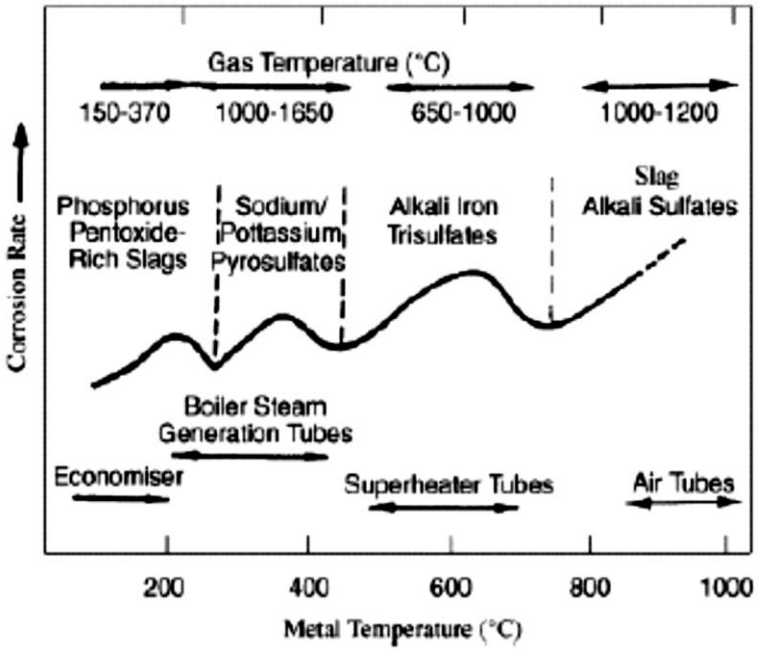

Figure 2.5: Regimes of fireside corrosion in coal-fired boilers (Natesan and Park, 2007).

The causes of ash corrosion in the high temperature portions of the superheater and reheater are better understood than ash corrosion of furnace walls. The conventional understanding of superheater and reheater corrosion by constituents within coal ash centers on the alkali trisulphates ($Na_3Fe(SO_4)_3$) and ($K_3Fe(SO_4)_3$). French (1982), Reid et al. (1945), and Corey et al. (1949) report that sodium and potassium iron trisulphates melt at about 621°C and have frequently been identified in corrosion areas. Mixtures of these two sulphates have melting points as low as about 554°C. The composition of these two will be dependent upon the relative amounts of sodium and potassium in the coal. Again, once the liquid phase forms, the protective iron oxide is dissolved and tube wastage occurs. Corrosion proceeds either by the participation of iron oxide in the formation of the trisulphate of the ease of transport of oxygen to the tube metal surface by the liquid phase to form iron oxide at the expense of the tube.

While the understanding of high temperature corrosion in superheaters and reheaters by liquid phases within the coal ash is reasonably well understood, no comparable understanding of furnace

wall corrosion is available. Furnace tube metal temperatures are about 358-426°C, well below the melting point of either of the trisulphates previously mentioned. Since a liquid phase is presumed necessary, it has been convenient to blame furnace corrosion on sodium or potassium pyrosulphate ($Na_2S_2O_7$ and $K_2S_2O_7$) but no definite evidence has been presented (French, 1982).

2.4.1 Furnace Wall Fireside Corrosion

The corrosion behaviour of the furnace wall tubes is closely linked to conditions in the furnace. Figure 2.4 shows the location of furnace wall corrosion in the combustion zone where the principal mode of heat transfer is by radiation, and flame temperatures reach 1400 to 1600°C (Reid et al., 1945).

Furnace wall tubes affected by fireside corrosion will demonstrate significant wall thinning on on the crown of the fireside of the tube. As shown in Figure 2.6, the thinned area is usually covered with hard deposits and loosely bonded ash on the outer layers. Corrosion often occurs in definite patterns associated with the direction of the flame, and has been linked to flame impingement (Reid et al., 1945). Flame impingement creates severely reducing conditions, high heat fluxes, and leads to the generation of corrosive species. The damage usually affects more than one tube at any given location and may cover extensive areas.

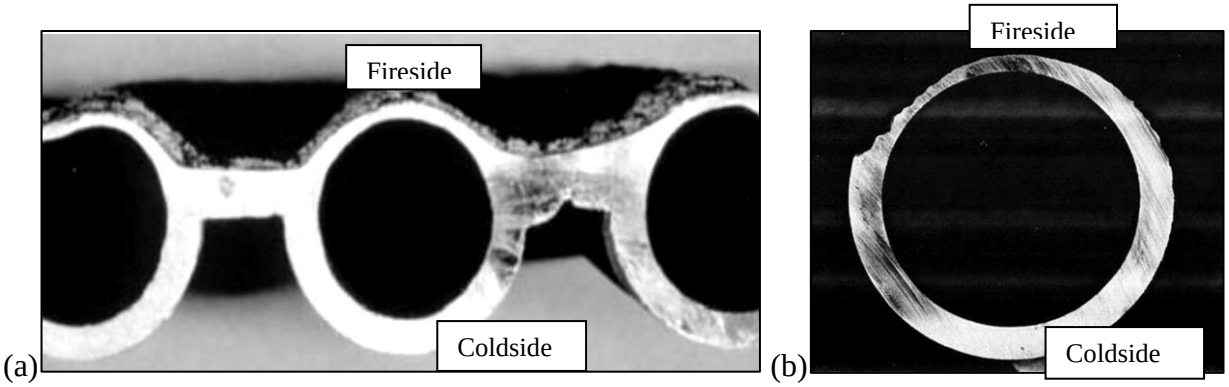

Figure 2.6: Typical appearance fireside corrosion showing (a) wall thinning and hard scale, (b) significant wall loss underneath the scale on the fireside (Dooley and McNaughton, 2007).

The precise morphology of the attack will vary somewhat with the particular environment and tube material. In general, however, the attack occurs on the crown of the tube where thick magnetite scales containing sulphide bands and islands are formed as shown in Figures 2.7. Unburned coal particles from the furnace, iron oxides, and iron sulphides are found in scale overlaid by sintered deposits. If a tube burst occurs, it is often in this location. Cracks perpendicular to the longitudinal direction may be evident as illustrated in Figure 2.7.

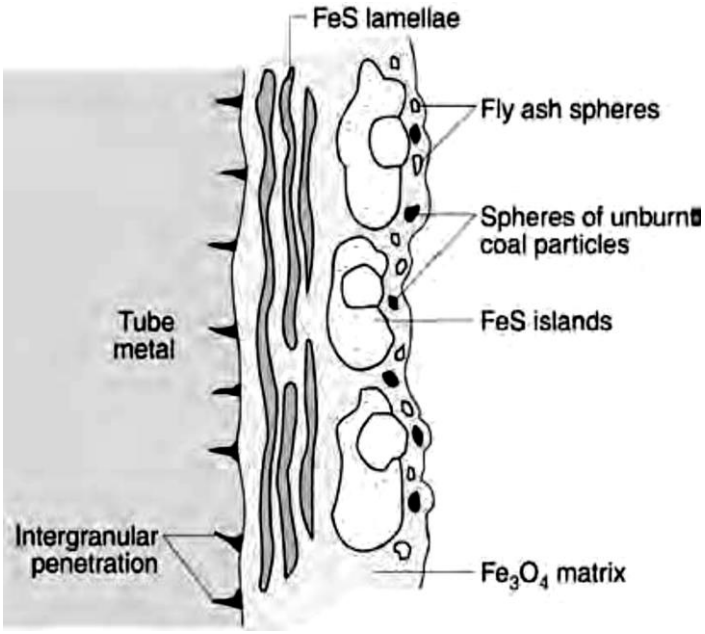

Figure 2.7: General structure of the fireside corrosion scale formed on a furnace wall tube under reducing environments (Wells et al., 1997).

Poor combustion conditions, e.g. with insufficient oxygen, produce a fuel-rich corrosion environment in a reducing atmosphere which contains high levels of CO and delivers unburnt coal particles to the tube surface. In addition, coarse PF increases the likelihood of unburned coal in ash deposits. The corrosion of the furnace walls can occur as a result of low melting salts and corrosive deposits.

French et al. (1982) bases his perspective of the furnace wall fireside corrosion on the failure investigations done on several furnace wall tubes over a period of approximately a decade.

Through analyses of the corrosion product performed by SEM/EDS and Differential Scanning Calorimeter, the only elements detected are sulphur, oxygen, iron, silicon and chromium. X-Ray diffraction revealed lines only attributed to the iron oxides. No sodium, potassium or chlorine was observed. Although sodium and potassium were not detected in the ash deposit, the presence of both elements in the ash suggests that pyrosulphates are possible. The suggestion made from the findings of the investigations was that the corrosion attack on the furnace wall tubes is associated with sulphides and requires strongly reducing conditions at the tube surface, but less so where SO_3 and pyrosulphates exist. French further states that carbon is required so the sulphites that form are stable. Carbon can enter the ash deposit either as unburned coal or the deposition from carbon monoxide. French et al. (1982) proposed that the corrosion occurs in several stages:

1) Na and K in the coal become oxides – in the flame
   a) $4Na + O_2 = 2Na_2O$ Equation 1
   b) $4K + O_2 = 2K_2O$ Equation 2
2) Sulphur in the coal becomes sulphur dioxide – in the flame
   a) $S + O_2 = SO_2$ Equation 3
3) Sulphur dioxide becomes the trioxide – catalysed on the tube surface or occurs in the low temperatures near the furnace wall.
   a) $2SO_2 + O_2 = 2SO_3$ Equation 4
4) Pyrosulphates form on the tube surface
   a) $Na_2O + 2SO_3 = Na_2S_2O_7$ Equation 5
   b) $K_2O + 2SO_3 = K_2S_2O_7$ Equation 6
5) Carbon deposits within the as either by:
   a) Unburned coal
   b) $2CO = CO_2 + C$ Equation 7
6) Tube wastage occurs by either:
   a) SO3 (from pyrosulphate) + 3C + Fe = FeS + 3CO Equation 8
   b) SO3 (from pyrosulphate) + 9C + Fe_2O_3 = FeS + 9CO Equation 9

Where chlorine is present in the coal, the alternative scheme involves chlorides that would form low melting point iron chloride or mixtures with other metals. Once these liquids form at the tube

surface, the corrosion proceeds in a similar fashion, SO_3 is transported by the liquid to the ash-metal interface where tube wastage occurs by the same reactions as given in item 6 above.

2.4.1.1 Corrosion due to Molten Alkali Sulphates

During combustion of the coal, pyrite (FeS_2) component of the mineral matter and organic sulphur compounds in the coal are oxidised to form sulphur oxides, SO_2 and SO_3 (Stringer, 1983). Alkali oxides, K-oxides or Na-oxides, react with SO_3 in the furnace atmosphere to form alkali sulphates, K_2SO_4 or Na_2SO_4, on the oxide scale. Some of the SO_3 diffuses through the alkali sulphates, and reaction occurs at the oxide-sulphate interface to form alkali-iron-trisulphates, $K_3Fe(SO_4)_3$ or $Na_3Fe(SO_4)_3$, according to the following two chemical reactions, (Harb and Smith, 2010):

$$3K_2SO_4 + Fe_2O_3 + 3SO_3 \rightarrow 2K_3Fe(SO_4)_3 \qquad \text{Equation 10}$$

$$3Na_2SO_4 + Fe_2O_3 + 3SO_3 \rightarrow 2Na_3Fe(SO_4)_3 \qquad \text{Equation 11}$$

where all of the species are in the solid phase at furnace wall conditions.

Corey, 1964, proposed a mechanism for external fireside corrosion which began with the formation of an alkali-metal sulphate layer on the tube surface. The source of the alkali metals were volatile species formed in the flame or from the molten slag. It was postulated that as the alkali sulphate layer thickened, the surface temperature would increase until ash began to stick to the surface as illustrated by Figure 2.8. The ash would subsequently sinter and eventually form a molten slag. Reactions in the ash during the melting process would result in the evolution of SO_3 as shown by equations 10 and 11. The enrichment of SO_3 is the result of melting of the outer (fireside) ash layer.

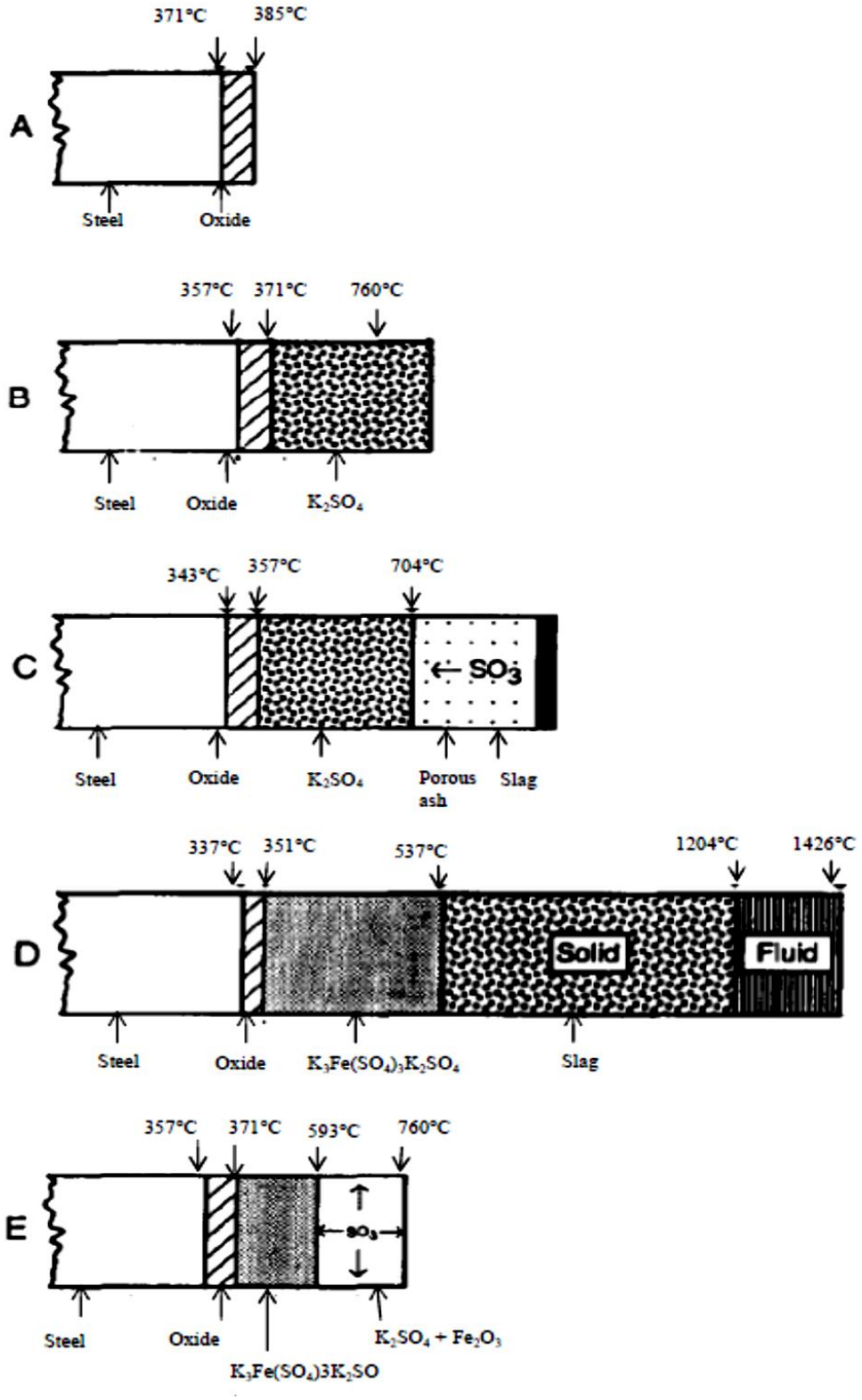

Figure 2.8: A mechanism for external fireside by alkali sulphates proposed by Corey (1964).

In addition to the formation of alkali-iron-trisulphates as shown in equations 1 and 2, Harb and Smith (2010) also suggest that one or two liquid pyrosulphates may form on the surface of the tube by the reaction of SO_3 with the alkali-metal sulphates through equations 12 and 13:

$$K_2SO_4 + 3SO_3 \rightarrow K_2S_2O_7 \qquad \text{Equation 12}$$

$$Na_2SO_4 + 3SO_3 \rightarrow Na_2S_2O_7 \qquad \text{Equation 13}$$

Pyrosulphates are molten in a temperature range of 370°C to 430°C and therefore affect furnace wall tubes. They are formed in the ash deposit under reducing conditions and also react with the oxide layer and the exposed substrate according to the following reactions (Bakker, 1998):

$$3X_2S_2O_7 + Fe_2O_3 \rightarrow 2X_3Fe(SO_4)_3 \qquad \text{Equation 14}$$

$$3X_2S_2O_7 + Fe_2O_3 \rightarrow 3X_2SO_4Fe(SO_4)_3 \qquad \text{Equation 15}$$

$$4X_2S_2O_7 + Fe_3O_4 \rightarrow 4X_2SO_4 + FeSO_4 + Fe_2(SO_4)_3 \qquad \text{Equation 16}$$

where X is either K or Na.

2.4.1.2 Sulphidation due to Iron Sulphide rich Deposits

Fireside corrosion on furnace wall tubes may occur without the presence of a liquid phase. Reid et al. (1971), observed corrosion in a dry-bottom furnace despite the fact that no flowing layer of slag was present. Perceptible roughening of the tube surface existed in a region on both side walls, with most of the loss occurring on the tube quadrant facing the burner. The corrosion was associated with a deposit which was principally iron sulphide as opposed to the alkali metal deposits. The deposit contained 0.5% carbon, indicating the presence of highly reducing conditions. In the quadrant away from the burner where corrosion was not significant, the adherent deposit was gray to greenish white in color and was of the sulphate type. Severe attack was also seen where there was poor distribution of coal from the burners (Reid et al., 1945). This was exhibited by thick black deposits on the walls which contained a high percentage of carbon.

Clarke and Morris (1980) found that in areas of persistently high corrosion, the furnace wall tubes formed thick magnetite scales containing distinct sulphide islands and bands, leading to high rates of metal dissolution, Fig. 2.9.

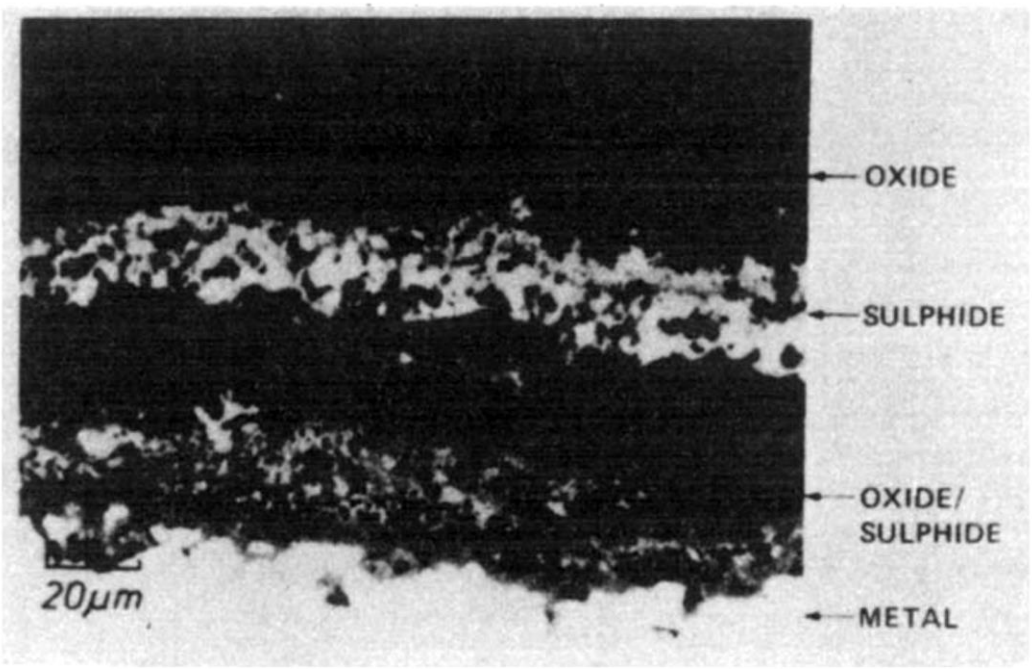

Figure 2.9: Thick oxide/sulphide corrosion scale from area of high CO concentration (Clarke and Morris, 1980).

Under normal oxidizing operating conditions, low alloy or carbon steel furnace wall tubes are protected from rapid corrosion attack by the formation of an iron oxide, usually Fe_3O_4 scale:

$$3Fe + 2O_2 \rightarrow Fe_3O_4 \qquad \text{Equation 17}$$

The Fe_3O_4 scale that forms is dense, impermeable to gases and strongly adheres to the tube. Such a favourable scale grows slowly and the growth rate decreases with time. It is also not easily removed by normal soot blowing operations or mechanical and thermal cycling.

Under reducing conditions, i.e. when the flue gas in contact with the furnace walls does not contain excess oxygen and contains significant amounts of CO, the following scenarios are possible (Reid et al., 1945):

The unburned pyrite (FeS_2) may further react directly with the iron in the tube walls to form more FeS through sulphidation reaction 18.

$$Fe + FeS_2 \rightarrow 2FeS \qquad \text{Equation 18}$$

Sulphur in the coal, i.e. unburnt FeS_2 and organic sulphur, may be partially converted into H_2S instead of SO_2 through reactions with H_2 present in the flue gas.

$$FeS_2 + H_2 \rightarrow FeS + H_2S \qquad \text{Equation 19}$$

$$S(org) + H_2 \rightarrow H_2S \qquad \text{Equation 20}$$

Although reaction (9) assumes that unburned FeS_2 is transferred to the tube surface, it is more likely that the species hitting the wall is a thermal decomposition product of the pyrite. Pyrite begins to lose sulphur at about 350°C and under flame conditions will decompose to form FeS in a reducing environment or iron-oxide in the presence of oxygen (Reid et al., 1945).

When H_2S is present in the flue gas, it will preferentially react with iron in the waterwall tubes, through molecular diffusion, to form FeS as follows (Norton, 1984):

$$Fe + H_2S \rightarrow FeS + H_2 \qquad \text{Equation 21}$$

By solid-state diffusion, already formed Fe_3O_4 may also be transformed into FeS,

$$Fe_3O_4 + 3H_2S \rightarrow 3FeS + 3H_2O + \tfrac{1}{2}O_2 \qquad \text{Equation 22}$$

FeS is known to wet the oxidized surfaces of furnace wall tubes. If subsequently exposed to oxygen, both FeS_2 and FeS on the wall will react to form iron oxide (Cutler and Grant, 1975). The

local sulphur activity is increased as the oxides are formed, resulting in an increase in the local concentration of SO_3. Therefore, the presence of iron sulphides on the tubes may influence the formation of corrosive deposits by increasing the local sulphur activity. Thus, depending on the relative amounts of H_2S, SO_2, CO and CO_2 present in the flue-gas, the scale formed on the steel may consist of iron oxide (Fe_3O_4), mixtures of Fe_3O_4 and FeS or nearly pure FeS (iron sulphide).

Sulphide scales allow higher rates of transport of iron cations than oxides, the strength and adherence of the scale decrease with increasing FeS content, while its growth rate and permeability increase significantly (Chou, 1984-1986). These scales are also brittle and poorly adherent, so they readily crack and spall. The weak, sulphur rich scale is also more easily removed by soot blowing or thermal cycling, which may further increase metal loss.

Hong and Yong (2002) state that high temperature corrosion of the water-cooled wall caused by sulphur in a coal-fired power plant can be divided into two types, namely sulphide type and sulphate type. Through this investigation of fireside corrosion at water-cooled wall from a coal-fired power plant in China, Yu et al. (2017) found that the corrosion products were composed mostly of iron-containing sulphide and magnetite and as a result classified the corrosion in this power plant as the sulphide. The general elemental distribution (including S, Fe, Si, Al, Na, K, and Ca) in the different layers of the corrosion product is shown in Fig. 2.10. He further states that the main reason for high temperature corrosion from the sulphide type is due to the large amount of H_2S, detached sulphur, and the unstable FeS that would be formed in the oxygen-deficient ambience when a high sulphur coal is burned.

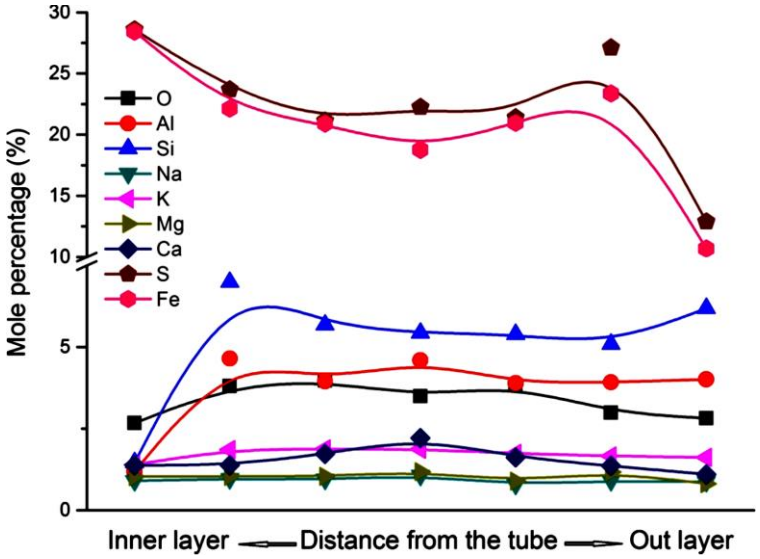

Figure 2.10: Elemental distributions of corrosion products along the section layer (Yu et al., 2017).

The performance of different alloys in corrosive combustion environments was shown by Chou et al. (1985), who investigated the corrosion resistance of various alloys in simulated low-NOx combustion gases at furnace wall temperatures. Scales consisting of two layers were formed on carbon steel and all but the most protective alloys. The outer layer was porous and non-adherent. X-ray diffraction analysis showed that the layer was FeS, which grew by outward diffusion of iron cations. The inner layers were compact and adherent, consisting of a mixture of Fe_3O_4 and FeS (Cr_2O_3 for the alloys). Corrosion rates increased rapidly with temperature. The addition of 1% oxygen to the reducing gas caused a significant decrease in the corrosion rate. Specimens were covered with a synthetic 'reducing' ash in order to examine the effect of ash deposit on the corrosion rate. No appreciable increase in the corrosion rate was observed for ash covered samples. No liquid deposits were formed. The presence of alternately oxidizing and reducing conditions increased the corrosion of carbon steel tubes.

Clarke et al. (1980) also observed a correlation between furnace wall corrosion and reducing conditions. Large concentrations of CO were almost always present in areas with persistently high corrosion rates and the furnace wall tubes formed thick magnetite scales containing distinct sulphide islands and bands, leading to high rates of metal dissolution. In one 120 MW front-wall fired boiler, high corrosion rates were measured when the CO concentration ranged from 0.61 to

4.3%. When the concentration of CO was greater than 3%, the H_2S concentration became significant (> 300ppm). Flatley (1981) reported that the solids reaching the furnace wall contained up to 50% combustible matter in areas where the CO level was high and significant corrosion was observed.

2.4.2 Super-heater and Re-heater Corrosion

The nominal steam temperature in the super-heater tubes is typically 538°C. The corresponding maximum metal surface temperature is in the order of 605°C, owing to additional temperature gradients through the tube wall. The gas temperature is considerably higher and is dependent on the position of the super-heaters. It may be as high as 1426°C if the super-heater tubes are in the roof of the radiant section, or as low as 1093°C for super-heaters further back in the convection pass (Dooley and McNaughton, 2007). Deposition build-up is most severe on the lead tubes where direct impaction of ash occurs.

Fireside corrosion of superheater and reheater tubes in a pulverised coal power plant is very much dependent on the coal chemistry, combustion conditions and operating temperatures. The amounts of chlorine, sulphur and ash, as well as the composition of the ash, in the coal are key factors (Syed et al., 2011). Super-heater and re-heater corrosion is normally associated with the deposition of a liquid alkali-metal trisulphate such as alkali-iron trisulphate $(Na, K)_3Fe(SO_4)_3$ onto the metal surface (Shreir et al., 1994). Alkali iron trisulphates form by the reaction of alkali sulphates with iron oxide in the presence of SO_3 as indicated by reactions 1 and 2. These salts can have melting temperatures as low as 552°C but are generally in the range of 600-650°C. This compares with the much higher melting points of the simple sulphates, for example at 884°C for Na_2SO_4 and 1069°C for K_2SO_4. Two conditions must be present to form alkali iron trisulphate. A source of Na or K must be present, and enough iron oxide must be in the deposit to catalyze the oxidization of SO_2 to SO_3. The formation of alkali iron trisulphates has an upper temperature bound set by their stability, which is a function of the partial pressure of SO_3 at the ambient temperature (Dooley and McNaughton, 2007).

Figure 2.11 shows melting behaviour of an alkali-iron-trisulphate. It is clearly seen that the liquid phase is stable at super-heaters/re-heaters tube temperatures and that the stability decreases with increasing temperature.

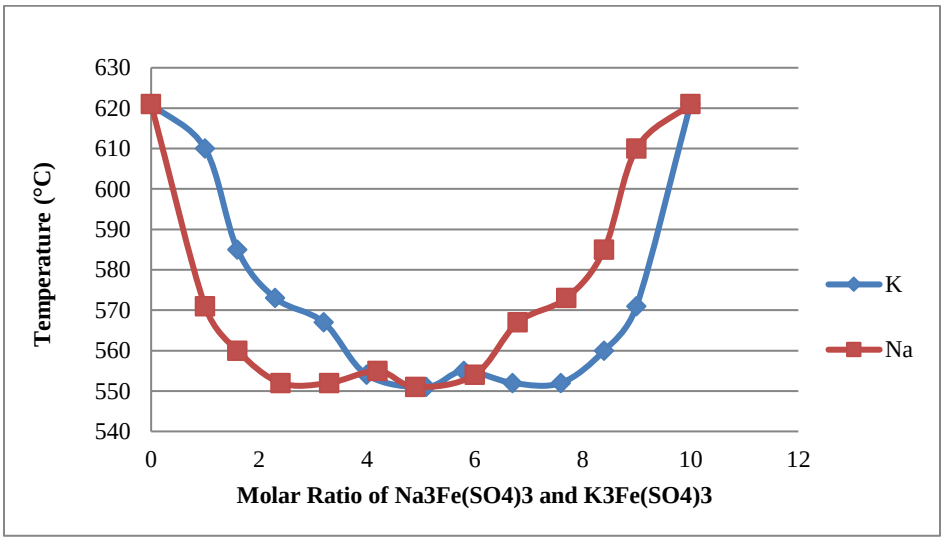

Figure 2.11: Melting points in the $Na_3Fe(SO_4)_3$-$K_3Fe(SO_4)_3$ system (Dooley and McNaughton, 2007).

The concentration of these sulphates increases at the metal surface by absorption onto the porous fly ash particles. The salts formed are usually molten in the range of 560°C to 730°C and contain free sulphur trioxide which dissolves the protective oxide film to form iron and chromium based sulphates (Chou et al., 1985). Tube wall loss will often be evident and manifested as flat spots on the tube in the positions where low melting point liquid phases of the alkali metal-induced iron-based materials form. A typical illustration of this damage and the presence of significant deposits can be seen in Figure 2.12 (Chou et al., 1985). Tube thinning is evident at the 10 o'clock and 2 o'clock positions (12 o'clock is the upstream position) around the edges of the deposit. Alternatively, the maximum wastage can occur at the 12 o'clock position.

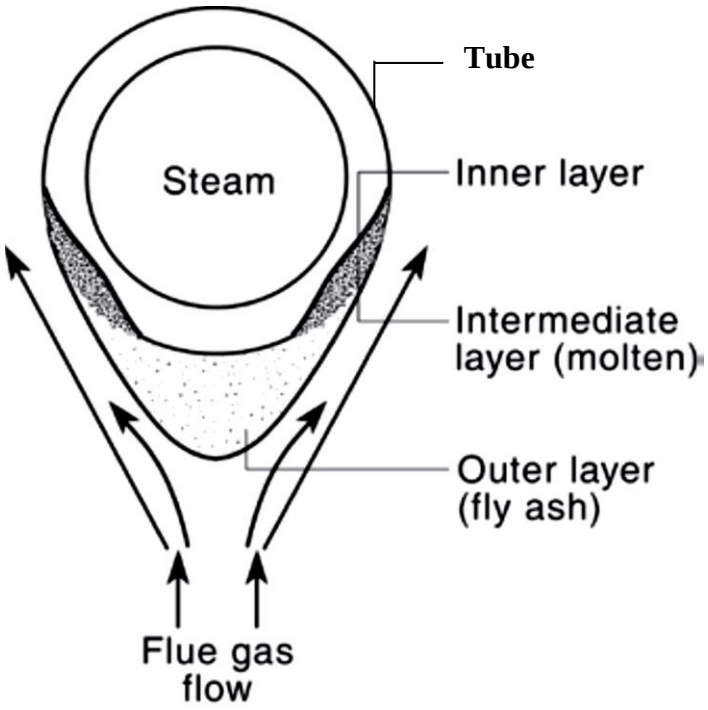

Figure 2.12: Fireside corrosion development for superheater and reheater tubes involving a molten intermediate layer (alkalis, sulphates) (Chou et al., 1985).

2.4.2.1 Superheater Corrosive Deposits

In the conventional pulverised coal power plant the heat exchangers tubes are exposed to combustion products and incombustible minerals in the flue gas, which deposit and enable volatile components to condense on tube surfaces resulting in severe metal loss (much higher than expected in simple oxidation). The deposits' corrosiveness is dependent on the flue gas and deposit chemical composition. Figure 2.13 illustrates the schematic of scales and deposits on superheater tube. The Figure 2.13 shows that sulphate deposits are molten where the corrosion rate is higher and follow a sulphidation mechanism (Syed et al., 2011, Cutler and Raask, 1981, Hendry and Lees, 1980).

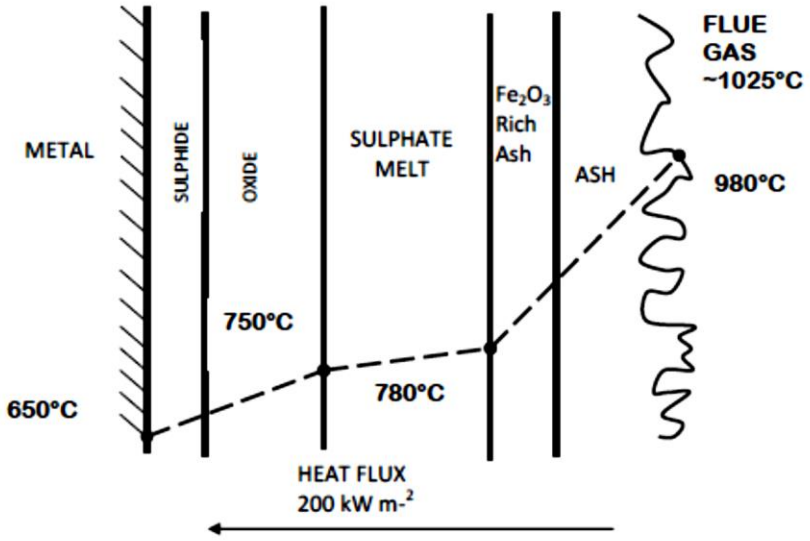

Figure 2.13: Schematic representation of ash deposit and temperature gradient at the super heater tubes in coal-fired power plants (Syed et al., 2011).

2.4.2.2 Alkali Iron Tri-sulphates

A wide range of literature shows the presence of molten alkali iron tri-sulphates [$Na_3Fe(SO_4)_3$ and $K_3Fe(SO_4)_3$] play a key role in fireside corrosion (Sidhu et al., 2006, Stringer, 1983, Viswanathan and Bakker, 2000). Bryers et al. (1995), and Reid et al. (1945), identified the presence of alkali-iron tri-sulphates and pyrosulphates on superheaters and furnace walls respectively, as responsible for tube wall loss. The mechanism believed for the formation of alkali iron trisulphate is not just one chemical reaction that leads metal loss. Instead, various different chemical reactions and mechanisms occur on the metal surface. Natesan and Park (2007), and Srivastava et al. (1997) explain that with an increase in temperature due to the thermal gradient that builds up, alkali sulphate becomes sticky at the outside surface, and more fly ash is captured. With further increase in temperature these sulphate compounds are decompose. The SO_3 required for the formation of alkali-iron-trisulphates, is generated by reaction of SO_2 with O_2 over Fe_2O_3. The resulting SO_3 migrates toward the cooler surface of the metal. With further build-up of the deposits the temperature of this sulphate layer falls and SO_3 at the tube reacts with iron oxides in the ash to form alkali-iron-tri-sulphate. An increase in SO_3 also increases the acidity of the molten salt and results in increased solubility of the oxide layer on the metal (Shamanna and Schobert, 1997). The

formation of mixed alkali iron tri-sulphates through the reaction of iron oxide and SO_3 is illustrated in equations 1 and 2 in section 2.4.1.1.

Molten alkali iron tri-sulphates are stable in the range of 600-700°C where high corrosion reaction rates occur, with a maximum at 670°C, (Khanna, 2002). At higher temperatures, the tri-sulphate dissociates and causes a decrease in the corrosion rate. These compounds are stabilised by SO3 and melt at a lower temperature in the range of 600-650°C but as a mixture can melt at temperature as low as 552°C (Stringer and Wright, 1995, Reid, 1971). The corrosion rates increase with temperature in the presence of these deposits, but then decrease when these complex compounds become unstable (due to a reduction of SO_3 levels with increasing temperature). This corrosion rate has been reported in several publications to be at its highest between 650-670°C (Khanna, 2002, Natesa and Park, 2007, Reid, 1971).

2.4.2.3 Pyrosulphates:

Alkali-pyrosulphates ($Na_2S_2O_7$ and $K_2S_2O_7$) are other sulphate products involved in metal loss by dissolving metal oxides. Srivastava et al. (1997) explained molten pyrosulphates exist at lower temperatures and perform corrosion reaction in the range between 400-482°C. Both the pyrosulphates ($Na_2S_2O_7$ and $K_2S_2O_7$) are likely to exist as deposits on heat-exchangers in the presence of sufficient SO_3. Figure 2.14 shows the melting point of alkali pyrosulphates (temperature range of 370°C to 430°C) and their dependence on SO_3 concentration.

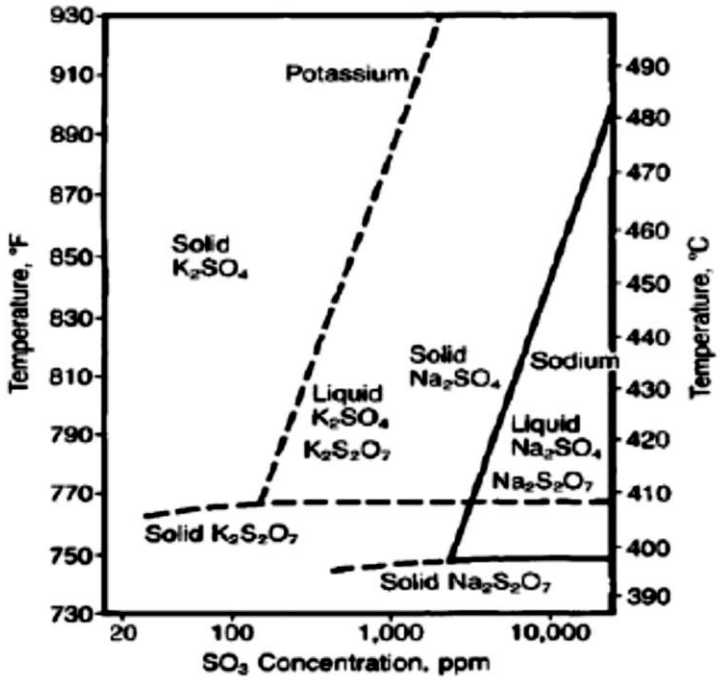

Figure 2.14: Melting points in system Na_2SO_4-SO_3 and K_2SO_4 (Reid, 1971).

The corrosion mechanism consists of the deposition of alkali sulphates on exposed metal surfaces followed by conversion of these to $Na_2S_2O_7$ and $K_2S_2O_7$ by reaction with SO_3 and then reaction with oxide films on metal surfaces as shown by equations 3, 4 and 7 in section 2.4.1.1.

2.5 DETECTION AND ANALYSIS OF FIRESIDE CORROSION

There are a number of actions that can be taken to confirm fireside corrosion or to monitor its progress; these include (Dooley and McNaughton, 2007):

i. Collecting and evaluating samples of fireside deposit. Analysis of the fireside deposit samples employs various techniques including Energy Dispersive X-ray Spectroscopy (EDS) to map out the concentration and pattern of elements within each layer of the fireside deposit, X-ray diffraction to determine what compounds are present, and either thermogravimetric or differential thermal analysis to determine the melting points of compounds in the fireside deposits.

ii. Monitoring corrosion online through the use of probes in susceptible locations. Monitor temperatures using thermocouples permanently installed across the superheater/reheater outlet legs in the vestibule can provide an indication of the hottest platens across the boiler.

iii. Evaluating the local environment in the furnace by monitoring for levels of O_2, CO, and H_2S, and performing field testing (e.g. gas analysis) to determine the combustion conditions in regions that are experiencing severe fireside corrosion.

iv. Using NDE measures, primarily UT testing, to identify wall thinning. When the ratio of wall loss to the build-up of steam side oxide scale is large (typically greater than a factor of three and certainly greater than five), then fireside corrosion (or erosion), not long-term overheating, is the dominant damage mechanism. Fireside corrosion will not occur simply because the tube temperature is elevated above the oxidation limit as with long-term overheating. For fireside corrosion to occur there needs to be a corrosive coal that produces low melting point deposits on the tube. Increasing the temperature of the tube will, of course, then increase the corrosion rate.

2.6 FACTORS AFFECTING FIRESIDE CORROSION

Generally, the factors that contribute to fireside corrosion of furnace walls and superheater/reheater areas are high tube metal temperatures, a reducing environment in the furnace, flame impingement, poor PF distribution, and poor quality of the coal (Chou et al., 1985).

2.6.1 High Tube Metal Temperature

Tube metal temperatures are an important factor in the mechanism of boiler tube failures. Tube metal temperatures depend on the heat flux from the fireside, the internal flow rate, and the condition of the working fluid. Heat transfer through the tube wall is mainly by conduction and involves several temperature gradients, as shown schematically for a subcritical furnace wall in Figure 2.15, (Bryers, 1995).

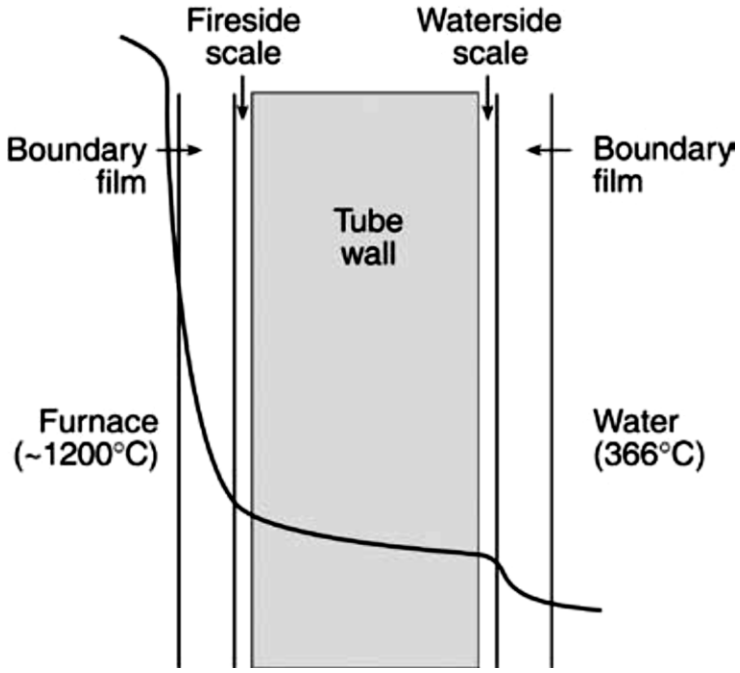

Figure 2.15: Typical temperature profile through a subcritical furnace wall tube (Bryers, 1995).

Furnace gas temperatures near to the wall are typically around 1200°C but a dramatic temperature gradient exists to the tube metal, mainly due to the cooling effect of the internal fluid, but also due to the low conductivity of the gas boundary layer and fireside scale (Bryers, 1995). Parameters that affect temperature of the tube include:

- Temperature of the water/steam flowing inside the tubes: If this temperature is too high, the tube material will not be cooled adequately and as a result overheating can occur.
- Internal oxide thickness: A thick oxide reduces the ability of the water or steam to cool the tube due to the heat transfer resistance of the oxide scale. The build-up of internal tube deposits can significantly raise tube temperatures.
- Flow restrictions in tubes: Flow restrictions in tubes removed from the location of corrosion damage can cause downstream overheating.
- External fouling: This can result in localised areas where tube metal temperatures allow for the precipitation of stable molten salts.

- Excessive flue gas temperature or heat flux: Areas of high heat flux and high thermal shocks have the greatest tendency of protective oxide exfoliation which leads to higher corrosion rates.
- Poor design: The length of the boiler tube exposed to the flue gasses greatly influences the temperature.

2.6.2 Furnace and Tube Reducing Environment

Under uniformly, constant oxidizing conditions, protective oxides form and fireside corrosion is not a problem. However, the development of reducing (substoichiometric) conditions from a variety of causes, can lead to deposition, primarily of iron sulphide and alkali sulphates. When the local environment subsequently becomes oxidizing, a variety of corrosive products are formed. The various causes of reducing conditions in the combustion chamber may include:

- Poorly adjusted or worn burners that create locally reducing conditions
- Improper air and fuel mixing
- Deposition of carbon rich deposits: The impingement of incompletely combusted coal particles can cause corrosive attack as they can continue to burn slowly on the tubes, creating an enhanced locally reducing environment. This could be caused by defective pulverization or classification
- Operating changes such as load changes that result in alternating between locally oxidizing and reducing conditions.

Reducing conditions can be prevented when the oxygen level is controlled between 2 and 9% during normal operation (Dooley and McNaughton, 2007). Higher excess oxygen will prevent generation of excess carbon monoxide. On the contrary, high oxygen content can (i) increase furnace exit, steam, and boiler exit temperatures, (ii) reduce boiler efficiency, (iii) cause overheating of tube material, and (iv) increase wear rates on tubes.

Clarke and Morris (1980) observed a correlation between furnace wall corrosion and reducing conditions. Large concentrations of CO were almost always present in areas with persistently high corrosion rates. They found corrosion rates exceeding 150 nm/h in a 120 MW front wall fired boiler when the CO concentration ranged from 0.61-4.3%. Reid et al. (1945) found CO concentrations of 0.9-4.9% in areas of corrosion. No corrosion was observed in areas where carbon monoxide was absent or present in quantities of less than 0.2%.

2.6.3 Flame Impingement and Poor PF Distribution

The size distribution of pyrite in the coal will affect the deposition of FeS. Coarse grinds will increase carbon in ash and on the tube surface, distorted oxygen distribution at the furnace outlet, high CO distribution at the furnace outlet, uneven steam temperature distribution and increased deposition of FeS.

Fireside corrosion often occurs in definite patterns associated with the direction of the flame and has been linked to flame impingement. Flame impingement creates severely reducing conditions, high heat fluxes, and leads to the generation of corrosive species. This implies that severe furnace wall corrosion of carbon steel is a consequence of poor local combustion conditions associated with flame impingement and the delivery of unburnt coal particles to the tube surface.

Lees and Whitehead (1983) reported that, under reducing conditions, the solid matter extracted through furnace wall ports may contain up to 50% combustibles or partially burnt pulverized fuel. This high density of particulate matter was often related to identifiable problems with the nearest burner or its associated milling and classification plant. The presence of combustible matter on the tube was associated with a sudden rise in mild steel corrosion rates. Two instances were cited where corrosion rates of 400 nm/h and 530 nm/h were observed at power stations where the coal particle density in the tube deposits was unusually high. It is clear, then, that furnace wall corrosion is associated with reducing conditions, i.e. low oxygen concentrations, increased levels of CO, the presence of H_2S, and the presence of partially burnt coal particles in the wall deposits. These conditions are often the result of poor combustion and flame impingement.

2.7 MITIGATION AND CONTROL MEASURES

Depending on the underlying root cause, the control measures of the fireside corrosion damage of coal fired boiler tubes may require immediate actions, long-term actions and prevention of repeat failures.

2.7.1 Immediate Actions

Immediate actions may include (i) replacements of failed tubes, (ii) repairs of damaged tubes, (iii) burner adjustments to prevent flame impingement, (iv) changing coal fineness to prevent deposition of carbon particles or to improve the combustion of pyrite, (v) chemical cleaning to remove build-up of waterside deposits, or (vi) modifying soot blowing operations (Dooley and McNaughton, 2007).

2.7.2 Long-term Actions and Prevention of Repeat Failures

There are three primary and not mutually exclusive routes that can be followed (i) materials solutions, (ii) fuel solutions, and (iii) operating options (Dooley and McNaughton, 2007).

2.7.2.1 Material Solutions

Replacement with the same material of either the same thickness, increased thickness, or a changed geometry: If the corrosion rate is only slightly higher than that required to reach the desired life as determined from a remaining life assessment, tube replacement can be made in-kind. If significantly higher corrosion rates than allowable are being experienced, then the options might be thicker tubes of the same alloy or a change of tube geometry.

Change to a more resistant material: If it is necessary to go to a more resistant replacement alloy, experience has shown that the ferritic materials with Cr levels greater than 9% provide sufficient resistance. Therefore, it has been recommended that a change in alloy be made to a material such

as 9Cr-1Mo or higher. The principal disadvantage is cost, which can be several times the cost of the original material. It is possible to use tubes that are co-extruded so that an inner layer of load-bearing mild steel is metallurgically bonded with an outer layer of corrosion resistant material, usually one that forms Cr_2O_3 in the furnace environment, as this restricts the formation of sulphides. The objective is to take advantage of the corrosion resistant outer material without the expense incurred by using it for the entire tube.

Weld overlays and thermal spraying: Thermal spray coatings and weld overlays can be used to provide a layer of corrosion resistant material to the furnace wall tubes. Good surface preparation prior to coating is crucial if this approach is to be effective. These two processes have also been used in shop fabrications to provide replacement tubes with improved corrosion resistance. These solutions use alloys with high chrome, 25 - 30% or higher, or chrome-nickel (45Cr-50Ni) content. The life expectancy of metal spraying is 3 to 5 years depending on the corrosivity of the environment, thermal cycles (which lead to spalling) and the quality of the application. Weld overlays, using Cr-Ni alloys can add between 7 - 15 years of life depending on the alloy used.

Thermal spray coatings are thin, typically 0.25 - 0.375 mm and are therefore most appropriately used when the anticipated corrosion rates are modest for temporary or emergency situations. To partially overcome the thinness of the protective layer, higher chromium contents (> 25 %) are typically needed. As with any coating technology, applying the coating is critical to obtaining a good result.

In the application of weld overlays, utility experience has determined that a minimum chromium content of at least 20% in the material of choice is required to slow furnace wall corrosion to acceptable levels (Sherlock, 1997). The higher the Cr content, the better the corrosion resistance and thus surface protection methods, or replacement materials are chosen with this in mind. The most commonly used alloys for weld overlay are stainless steels such as austenitic Type 309, duplex stainless steel Type 312, traditional nickel-based alloys such as alloy 625 and alloy 622, and some less traditional nickel alloys such as alloys 52 and 72 (Dooley and McNaughton, 2007).

2.7.2.2 Fuel Solutions

Fuel change, blending, and washing: It may be technically desirable to switch fuels or to blend to, for example, lower pyrite levels to minimize the formation of FeS. However, such procedures can often be economically prohibitive and further, there are usually overriding considerations not related to corrosion, such as SO_2 requirements.

There are methods that can be employed to investigate the potential effects of coal changes, blending, and washing. Such a method will provide information on the total economic impact as well as about the potential for fireside corrosion.

Change coal particle size: Reducing the coal particle size can ensure complete combustion and thus reduce the amount of unburnt carbon and residual ash in the flyash. This change has generally been found to have a lesser effect than combustion modifications.

2.7.2.3 Operating Options

Combustion process changes: Combustion system modifications may be helpful in reducing fireside corrosion rates. Unfortunately, the results of modeling and the efficacy of combustion modifications have been found to be boiler and burner system specific so that universal prescriptions are not available (Sherlock, 1999).

Combustion modelling is a tool mostly used to introduce changes in the combustion process. Combustion Fluid Dynamic (CFD) modelling simulates all known reactions occurring during the combustion process in a boiler and is also able to track trajectories of ash and coal particles (Bakker, 1998). Thus, it can predict flue gas temperatures and compositions anywhere in the boiler as well as deposit formation and the composition thereof. These predictions can be compared with known areas of high corrosion rates to determine if there are any correlations.

For problematic units, the following steps are indicated:

i. Establish a combustion fluid dynamics (CFD) model using current operating parameters.
ii. Confirm that the results of the model predict the locations of highest corrosion damage or locations of highest FeS deposition.
iii. Compare the model predictions to easily measured boiler parameters such as NOx emissions, fly ash rate, and furnace exit temperature.
iv. Evaluate the effect of changes in parameters such as air/fuel ratios, coal grind, and flame direction.
v. Some of the parameters that can be evaluated and adjusted are:

Bakker (1998) made a model for a supercritical, tangentially fired boiler, suffering from corrosion primarily on the front and rear wall. The combustion model showed that the area of high corrosion did not correlate very well with areas where the flue gas near the wall was reducing and contained high levels of H_2S. However, the corrosive areas correlated quite well with the areas where deposits of FeS and unburned carbon are likely to occur.

Improve cleanliness of tube internal surface by chemical cleaning and employing appropriate cycle chemistry controls: If the excessive temperatures in furnace wall tubes are caused by internal deposits, chemical cleaning should be conducted followed by a campaign to optimize the feed water chemistry.

3. EXPERIMENTAL DESIGN AND METHODOLOGY

The investigation into the mechanisms of fireside corrosion existing in the Eskom's fossil fired boilers at power stations A, B and C was conducted by firstly removing tubing samples from the affected locations of the boiler, followed by the evaluation of the tubes material and analysis of the fireside deposit. The fireside deposit was analysed visually, macroscopically and microscopically through the application of various techniques. Visual examination and stereomicroscopy were used to identify the features of the fireside deposit and areas with localised

wall thinning, whereas SEM (EDS), QEMSCAN and XRD were used to characterise the composition of the fireside deposit, and DTA was applied to determine the thermal behaviour of the fireside deposit particularly with focus.

3.1 SAMPLING

During plant shut-downs at power stations A, B and C, tubing samples were removed from the areas that are historically known to suffer from fireside corrosion. The selection of the samples was made from the following categories:

- Tubing that failed during operation,
- Tubing with wall thickness as measured below the minimum during Ultrasonic Testing (UT).

The sampling areas selected were where fireside corrosion related failures occurred or tube replacements were required due to low remaining wall thicknesses. A minimum of two units per power station was sampled for representability and repeatability of results. From each unit, at least two tubes were investigated. Table 3.1 outlines the boiler tubes considered in the investigation.

In order to ensure that the fireside deposit is preserved during sampling, the in-house procedure for cutting, storage and transportation of samples was applied. The tubes were cut to a minimum of 1 m length with a saw and at least 300 mm away from damage in order to prevent debris from contaminating the damaged area as well as preventing it from overheating. Subsequent to cutting, tubes were marked clearly to show boiler unit number, location, level, tube number and sample orientation. The tubes were restricted from movement during transportation in order to avoid spalling off the fireside deposit; the tubes were also kept away from contact with water or any other liquid during storage or transportation.

A check list, see Table 3.1, with all the important points was also put together for the site engineers in order to simplify the process of ensuring that sampling of fireside corrosion affected tubing is carried out properly. In all three power stations, the areas sampled included the side walls, division walls, front and rear wall, as per the outline in Table 3.2.

Table 3.1: Checklist for Tube Identification and Labelling

GENERAL INFORMATION			
POWER STATION			
CONTACT PERSON			
UNIT NO.		**BOILER SECTION**	
ELEVATION (m)		**ROW NO.**	
CHECKLIST <u>ONLY TICK WHAT IS DONE</u>			
Tube has an identification, orientation has been marked, e.g. water flow			
There was no overheating during cutting of the sample(s)			
Cutting oils have not been used			
Tube section is at least 1 m long			
Flame cut sample has additional 300 mm of material per each end			
SPECIAL PRECAUTIONS			
(a) During storage and transportation, there must be no contact with water or any other liquid.			
(b) During transportation, movement of tubes must be restricted to prevent spalling of deposit.			

Table 3.2: Tubing Sample Description

Power Station	**Boiler number**	**Number of tube sections**	**Tube identity and location**
A	Unit 1	2	SW and DW
	Unit 2	2	FW
	Unit 3	1	SW,
	Unit 4	3	SW and DW
B	Unit 1	2	FW and DW
	Unit 3	2	DW
	Unit 8	1	DW
	Unit 10	2	DW
C	Unit 4	1	SW
	Unit 6	1	DW

SW: Side wall DW: Division wall FW: Front Wall

3.2 TESTING AND ANALYSIS

Techniques applied in the testing and analyses processes were kept constant for all three power stations, however, this consistency could not be extended to the level of Units due to the limitations in the availability and accessibility of the boiler tube samples. Table 3.3 shows the tests and analyses done per boiler Unit.

The schedule for planned outages varied from one station to another and at other times this was not implemented as per plan. There were postponements and cancellations of some of the planned outages and this affected the availability of the tubes and the logistics around the testing and analysis. Therefore, the same techniques and equipment for testing and analysis could not be applied to tubing samples.

Table 3. 3: Techniques Performed for Boiler Tube Evaluation and Fireside Deposit Analysis

Power Station	Visual Inspection	Chemical Analysis	Hardness Evaluation	Light Microscopy	SEM	QEMSCAN	XRD	DTA
Station A								
Unit 1	Y	N	N	Y	Y	Y	Y	N
Unit 2	Y	N	Y	Y	N	Y	Y	Y
Unit 3	Y	N	N	Y	Y	Y	Y	Y
Unit 4	Y	N	N	Y	N	Y	N	Y
Station B								
Unit 1	Y	N	Y	Y	Y	N	Y	Y
Unit 3	Y	N	Y	Y	Y	N	Y	N
Unit 8	Y	N	Y	Y	N	N	N	N
Unit 10	Y	N	Y	Y	N	N	N	N
Station C								
Unit 4	Y	N	N	N	Y	Y	Y	N
Unit 6	Y	N	Y	N	N	N	Y	N

Y = Yes, testing or analysis was performed **N = No,** testing or analysis was not performed.

3.3 CONDITION OF THE TUBES INVESTIGATED

Specimens were sectioned from the tubes for testing and verification of the material. The material of the tubes was verified by means of chemical analysis with spark emission spectroscopy, microstructural examination and harness testing with Leco Macro Vickers Hardness Tester. The results obtained were benchmarked against the standard specification BS EN 10216-2 (2013), which is equivalent to the original code used in the design of the tubes.

3.3.1 Visual Inspection

The tubes were inspected in the as-received condition in order to ensure that the samples are in an acceptable state for laboratory testing and analysis, with the correct identification. Visual examination of the damaged or failed tube can give the investigator a rough idea of the most likely causes of damage or failure. All the relevant observations were recorded in written form and photographs were taken and documented.

3.3.2 Material Identification

A specimen was prepared by cutting out a ring from each tube with an abrasive cutter, ground with 80 micron silicon carbide paper to remove burs and sent for chemical analysis. Optical emission spectrometer was used on each specimen to determine the elemental composition. Standard specifications, BS EN 10216-2 (2013), ASTM A106 (2018), and ASTM A105 (2018) were used to verify the chemical compositions of materials 15Mo3/16Mo3, SA106 and SA105 respectively.

3.3.3 Hardness Test

Another ring was removed from each tube and metallographically prepared to determine the hardness properties of the tubing material. Metallographic preparation was performed according to ASTM E3, 1995, by grinding each ring cross section with silicon carbide papers ranging from 80 micron to 1200 micron to remove burs and scratches. Subsequent to grinding, the specimens were polished using aluminium diamond suspensions from 3 micron to 1 micron to achieve a

smooth surface finish. The polished specimens were then cleaned under running water, dipped in alcohol (acetone) and dried.

The hardness of the polished specimens was measured using a macro Leco Macro Vickers Hardness tester at a load of 10 kg as per ASTM E92, 2017. The hardness results presented in HV units were converted to ultimate tensile strength in MPa using hardness conversion tables outlined in ASTM A370 (2019) and benchmarked against the respective materials standard specifications.

3.3.4 Microstructural Examination

A third ring cross section was removed from each tube and metallographically prepared in the same way as in the hardness test. Subsequent to polishing and cleaning, the specimens were etched with 5% Nital to reveal the general microstructure of the steel. The etched samples were then examined under an optical microscope for the following information:

- Microstructural morphology and phases present
- Microstructural degradation
- Tube wall thinning
- Other forms of corrosion, e.g. pitting, intergranular corrosion
- Other forms of damage mechanisms, e.g. cracks or cavities
- Morphology and thickness of fireside deposits.

All the relevant observations were recorded in written form and also photographs were taken and documented.

3.4 DEPOSIT ANALYSIS

Mechanical, cutting and scraping, and metallographic methods, grinding, polishing and etching, were employed during the preparation of the fireside deposit specimens. The analysis and characterisation of fireside deposit were performed using the following analytical tools and methodologies:

- Scanning Electron Microscopy (SEM) with Energy Dispersive X-ray Spectroscopy (EDS) to study the morphology, scale layer thickness and map out the concentration and elemental distribution within each layer of the fireside deposit.
- Qualitative Evaluation Mineralogy Scanner (QEMSCAN) and X-Ray Diffraction (XRD) to determine the mineralogy (compounds content) of the fireside deposit.
- Differential Thermal Analysis (DTA) to determine the thermal behaviour of the compounds in the fireside deposit.

3.4.1 SEM and EDS Analysis

Cross sections of the tubes with attached fireside deposit were prepared for SEM-EDS. Two tube ring cross sections with the deposit still intact were removed from each tube using dry cutting to avoid contamination from fluids and metallographically prepared. Figure 3.1 illustrates the way the fireside deposit was analysed and characterised.

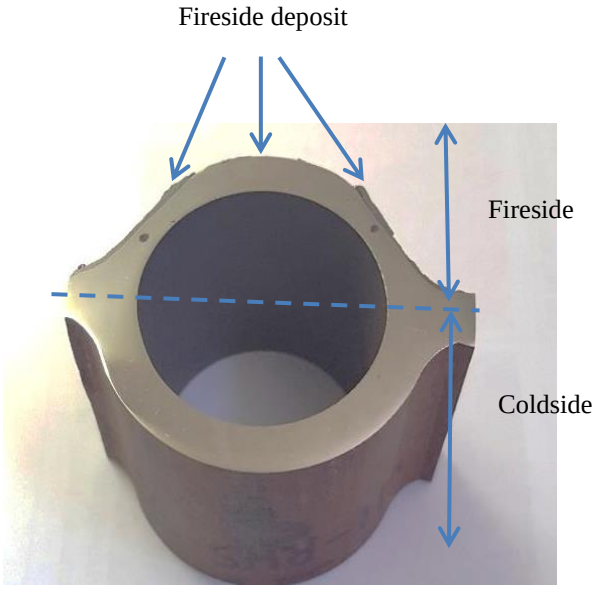

Figure 3.1: Cross section samples of the tube prepared for microstructural examination and SEM analysis of the fireside deposit at 10 o'clock, 12 o'clock and 2 o'clock positions.

Tube specimens were characterised with a SEM of model FEI – QUANTA 600 and the fireside deposits were analysed and mapped along the cross section as shown in Figure 3.2. The data generated from the analysis was processed and interpreted using software INCA Feature version 1.1.

The chemical compositions of the deposits and corrosion products on the metal surfaces were studied using EDX by elemental mapping. However, EDX mapping only gives qualitative data and so quantitative data were generated using EDX line profiles.

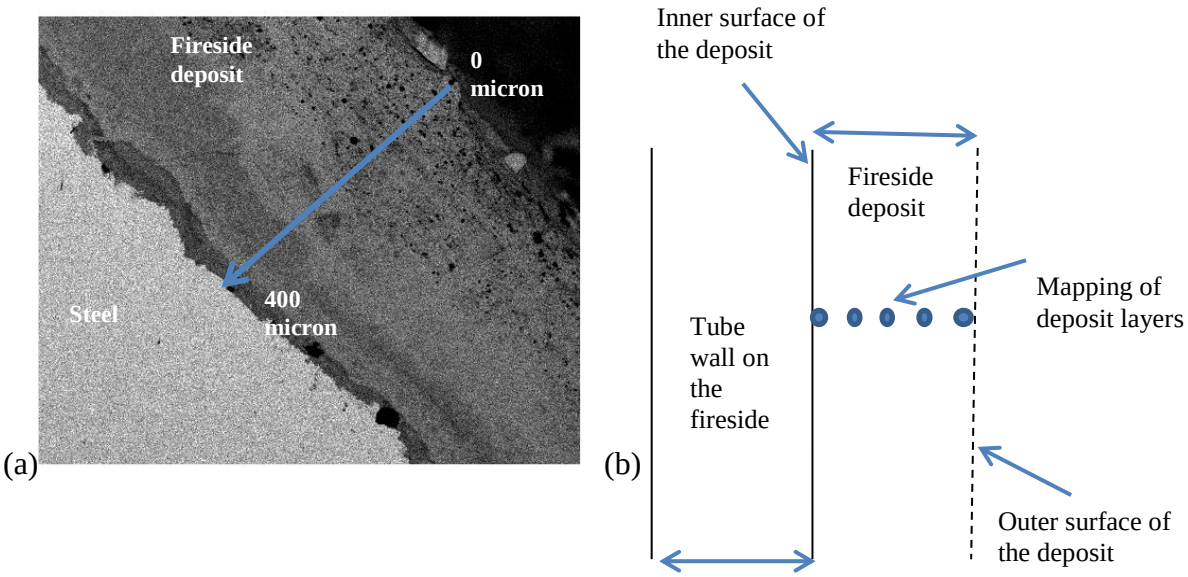

Figure 3.2: (a) SEM fireside deposit mapping from outer later to inner layer, (b) Analysis and mapping of the SEM and QEMSCAN deposit on the fireside of the steel surface.

3.4.2 QEMSCAN

QEMSCAN is a form of scanning electron microscope with finer increment of analysis, and a based system configured to automatically determine the mineralogical characteristics of any particulate sample. Originally QEMSCAN was developed to determine the mineral proportions and characteristics of base metal and precious mineral samples. However, in the power utility it is mainly used to determine the mineral and phase proportions in coal, clinkers, fouling deposits and fly ash. The model used for the analysis of the fireside deposits is QEMSCAN 650F.

The specimens for QEMSCAN were sectioned to 10 x 50 mm and then mounted in a cold mounting resin as shown in Figure 3.3. Prior to the analysis the mounted specimens were coated with carbon to create a conductive surface to minimise charging during the testing. The data generated from the analysis was processed with Discover version 5.3 software. Figure 3.4 and 3.5 illustrate how the fouling particles were characterized.

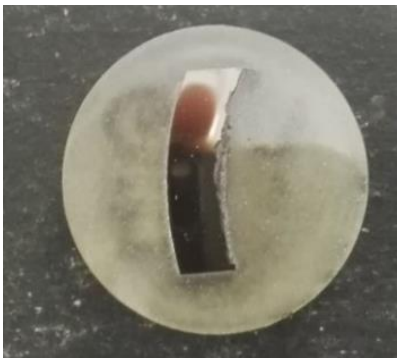

Figure 3.3: A cross section specimen of the tube prepared for QEMSCAN analysis, mounted in cold mounting resin, external surface with the fireside deposit on the left, and the internal surface (waterside) on the right.

The entire thickness of the fireside deposit was examined and characterized as illustrated in Figure 3.4. The compounds comprised in the deposit are presented in colour categories and modal proportions as shown in Figure 3.5.

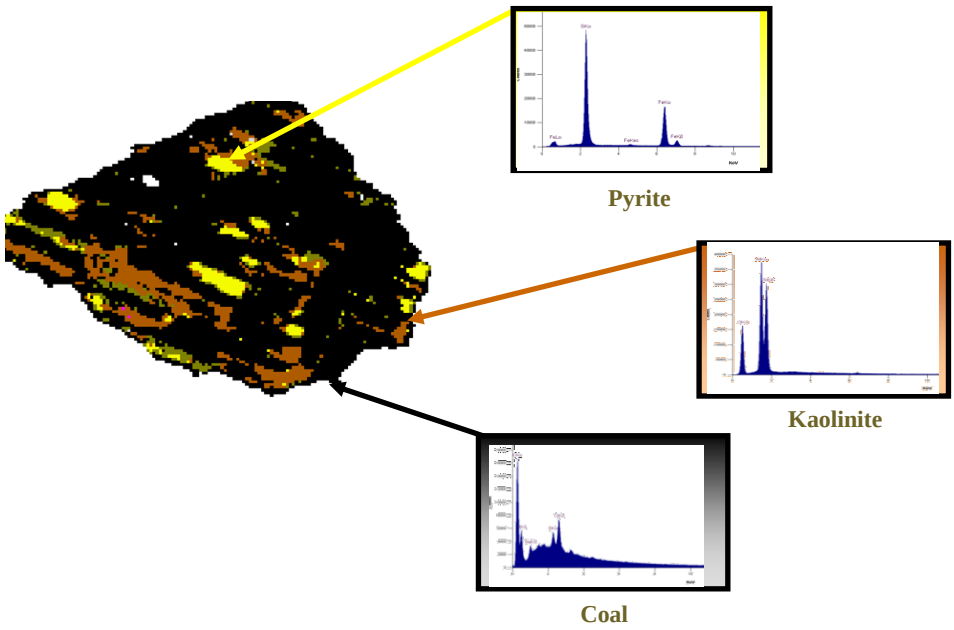

Figure 3.4: Automatic mineral identification and image creation.

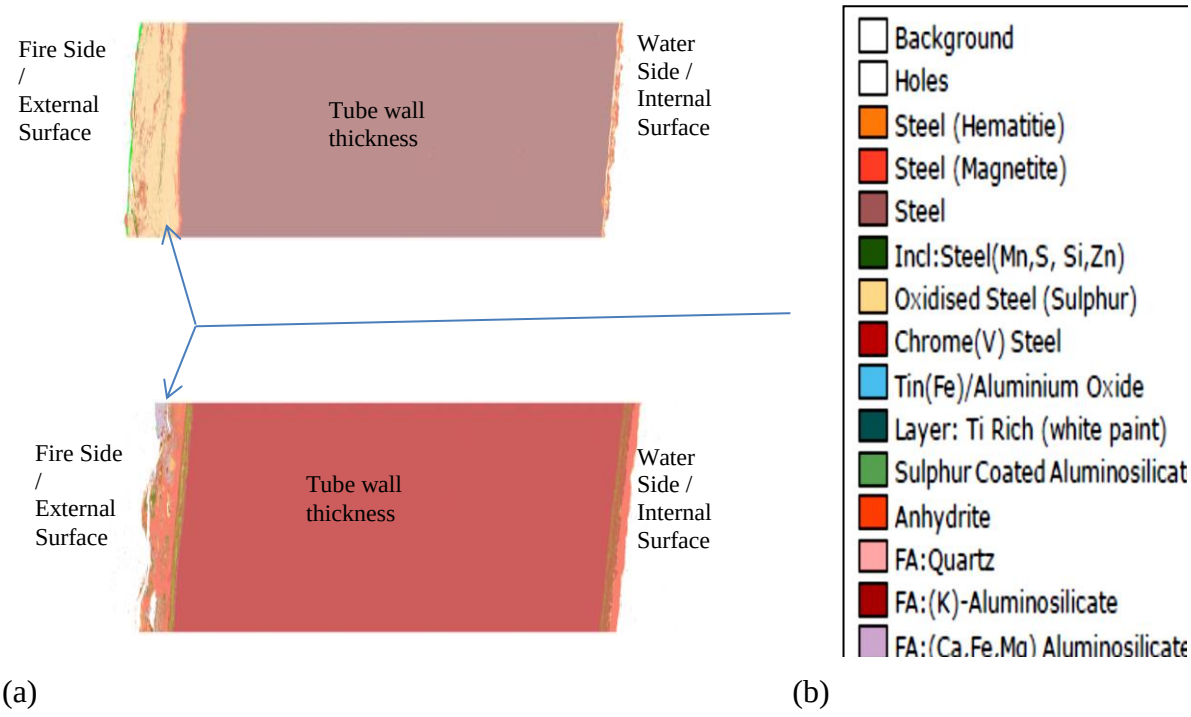

(a) (b)

Figure 3.5: QEMSCAN image of a cross section showing (a) the entire thickness of the tube from internal to external surfaces, (b) colour legend used for qualitative characterisation of the deposit.

3.4.3 XRD Analysis

X-Ray Diffraction (XRD) was also used to detect the phases present in the fireside scale and was used as a complementary tool to the QEMSCAN analysis. The specimens were prepared by scraping off 12g of the ash deposit from the fireside of the boiler tubes and grinding it into a powder. The powder specimens were mounted onto sample holders, Figure 3.6, and analysed with a Single Crystal X-Ray Diffraction (SC-XRD) with a Bruker D8 Venture Photon CMOS. The data generated from the analysis was processed, and interpreted using the Diffrac.Suite EVA version 4.2.2 (Bruker brand) software.

Figure 3.6: Sample holder for powder specimen to be analysed with XRD.

3.4.4 DTA

The aim of the thermal analysis was to track any phase changes that may have occurred in the fireside deposit and determine whether these phase changes are linked to low melting salts, e.g. tri-sulphates complexes.

Differential thermal analysis (DTA) is a thermoanalytic technique in which the temperature difference between a substance and a reference material is measured as a function of temperature whilst the substance and reference material are subjected to the same controlled temperature conditions (e.g. heating rate, furnace atmosphere, composition, shape and size) (Haines, 2001). This differential temperature is then plotted against time, or against temperature. Changes in the sample (e.g. phase transitions, dehydration, and decomposition, redox, or solid-state reactions),

either exothermic or endothermic, which lead to the absorption or evolution of heat, can be detected relative to the inert reference (Haines, 2001). Figure 3.7 shows the key features of a differential thermal analysis kit are as follows:

- Sample holder comprising thermocouples, sample containers (crucibles) and a ceramic or metallic block.
- Furnace.
- Temperature programmer.
- Recording system.

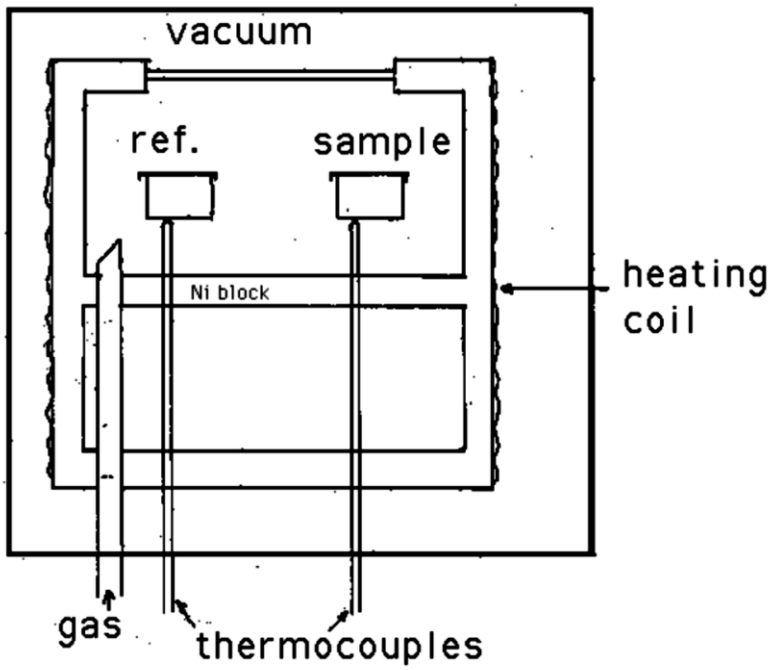

Figure 3.7: Schematic illustration of a DTA cell (Haines, 2001).

The scraped off fireside deposit specimen of 10 g was placed inside a crucible and put on the sample holder inside the DTA chamber. The sample holder assembly consists of a thermocouple each for the sample and reference, surrounded by a block to ensure an even heat distribution. The analysis of the fireside deposit was performed under controlled conditions where the following were specified:

- Alumina crucibles of 6x2.5 mm size

- Maximum temperature of 1400°C
- Heating rate of 10°C/min
- Testing atmosphere (Nitrogen in the furnace)

The results are presented in DTA curves of differential temperature against temperature. Peaks on the curve correspond to the evolution or absorption of heat following physical or chemical changes in the test sample.

3.5 IN-SITU GAS ANALYSIS

In a separate project looking at the environment of the furnace, the actual conditions of the flue gas were determined by performing in-situ combustion tests which involved analysis of the composition of the flue gas, measurements of the tube temperature, and analysis of the distribution of air (or excess oxygen) in the furnace. The in-situ gas analysis was conducted at Unit 1 of Station A over a period of three days at different excess air levels with Oxygen (O_2) at 2.48%, 2.82% and 3.1% dry basis. The in-furnace probing positions were located at gun blower 12 (one of the areas where fireside corrosion has occurred repetitively) and furnace exit. Temperature traverses were conducted on both the left hand side and right hand side of the economiser inlet and outlet areas. Oxygen and carbon monoxide measurements were taken at furnace exit and both sides of the economiser outlet ducts. The results obtained from the gas analysis of station A were checked against the fireside deposit analysis of station A to determine the link between the furnace environment and the type of fireside corrosion taking place in station A.

4. RESULTS

4.1 CONDITION OF THE TUBES INVESTIGATED

4.1.1 Visual Inspection

Hard and thick sintered deposits were observed on the fireside of the tubes and loosely bonded ash on the outer layer on tubing from all three power stations, as shown in Figure 4.1. Wall thicknesses of the tubes varied from slightly thinned to very thin on the fireside, whereas the wall thinning on the non-fireside was uniform and minimal. Localised wall thinning was found on the fireside of the tubes from station A and C at a 120°C angle from the 10 o'clock to the 2 o'clock positions as illustrated by Figure 4.2 and 4.3. One of the tubes from station A had actually ruptured in this area (Figure 4.1a) due to significant wall thinning and excessively resulting in high stresses.

The wall thickness measured on the fireside of tubing from Station A varied from 0.66 mm to 4.93 mm in thickness and 0.1 mm at the rupture tip with an installed as original wall thickness of 5.6 mm, the wall thinning was in the range of 11.9 - 98.2%. Wall thickness measurements on the fireside of the tube from Station C ranged between 2.9 mm to 3.4 mm. Based on a 7.5 mm installed wall thickness, the wall thinning was in the range of 45.2 - 65.3% for the tubing from Station C. The deposit thickness was up to 0.97 mm and 0.57 mm for station A and C respectively. Such thick deposits have been seen to result in tube overheating, which can aggravate the damage on the tubes. However, no sign of overheating was observed.

(a) (b) (c)

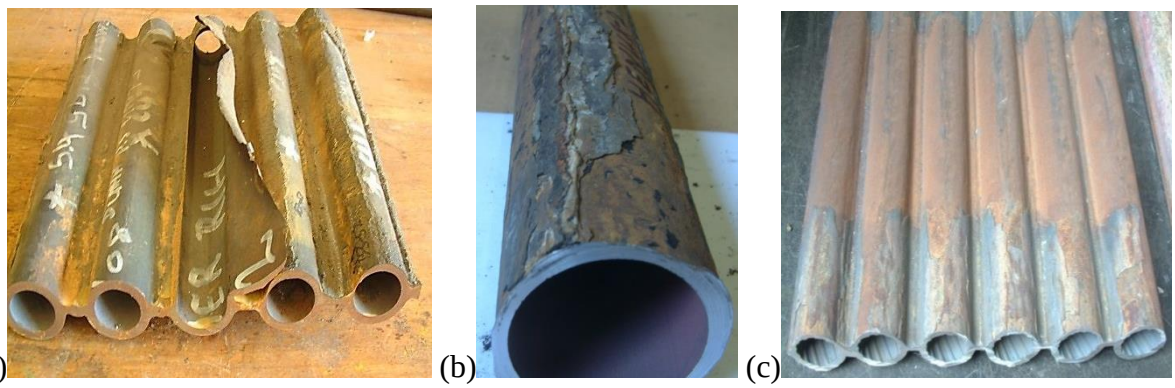

Figure 4.1: Furnace wall tube from (a) Station A with a ruptured tube, (b) Station B and (c) Station C, showing the fireside deposit.

(a)

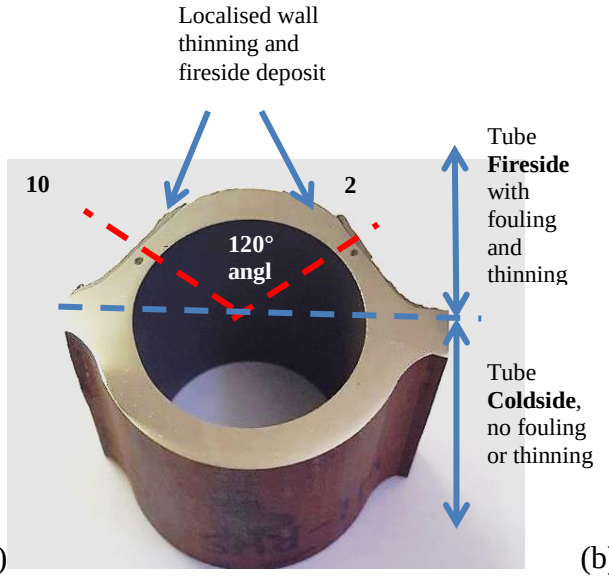

(b)

Figure 4.2: Samples prepared for SEM analysis with fireside deposit located (a) at 10 o'clock and 2 o'clock positions and (b) at 12 o'clock position of the fireside of the tube.

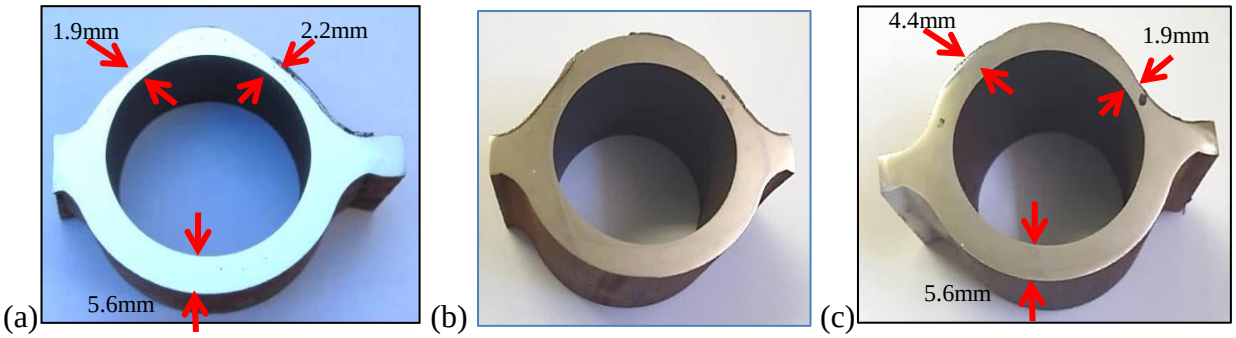

Figure 4.3: Specimens of tubing from Station A (a) Unit 2, (b) Unit 3, (c) Unit 1.

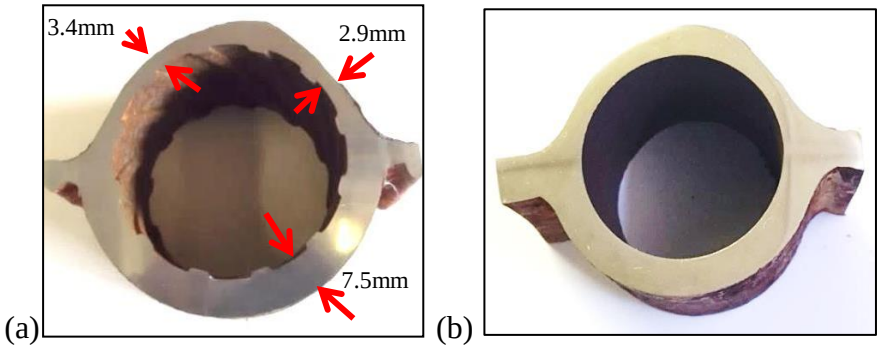

Figure 4.4: Cross section specimens of tubing from Station A (a) Unit 6 and (b) Unit 4.

Tubes from station B showed different features to those from Stations A and C. Unit 1 tubes revealed general wall thinning around the tube circumference. However, tubes from Unit 8 and 10 showed uniform thinning only on the fireside. Tubes from Unit 3 on the other hand showed a completely different picture, inconsistent wall thinning on both fireside and non-fireside, as shown in Figure 4.5c. Observations made on tubing from Station B suggest that the boiler units either experienced different forms of attack, or were subjected to the same corrosion mechanism, but to different degrees of attack. The fireside deposits on tubing from Station B were also different. Tubes from units 1 and 3 had hard and thin, sintered brown deposits, whereas those from Unit 8 and 10 were loosely bonded grey ash deposits. The wall thickness of the tubing from Station B ranged between 1.76 to 5.54 mm. Based on 6 mm installed wall thickness, the highest wall thinning was 70.6%. Maximum deposit thickness 0.6 mm.

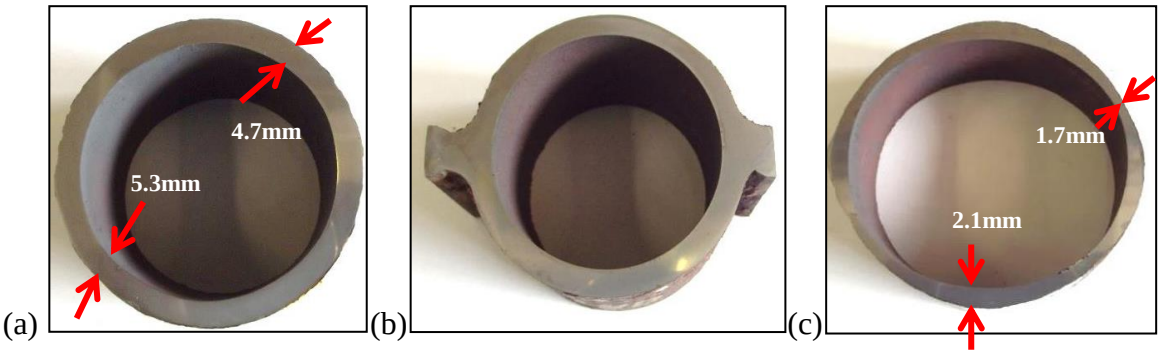

Figure 4.5: Cross section specimens of Station B tubing showing (a) uniform wall thinning on fireside and coldside of Unit 1, (b) uniform wall thinning on fireside of Unit 8 and (c) uneven wall thinning on fireside and coldside of Unit 3.

4.1.2 Chemical Properties of the Tubes

The chemical composition of Station A, B and C tubing correlates with the standard specifications of 16Mo3, SA106 and SA105 respectively, as outlined in tables 4.1, 4.2 and 4.3.

Table 4.1: Chemical analysis of tubing samples from Station A

Element	**Weight %**	**Specification for 16Mo3/15Mo3 as per BS EN 10216-2 (2013)**
Carbon	0.16 ±0.02	0.12-0.20
Manganese	0.56 ±0.05	0.40-0.90
Sulphur	0.013 +0.005	0.025 max
Phosphorus	0.018 +0.005	0.030 max
Silicon	0.31 ±0.05	0.35 max
Chromium	0.05 ±0.05	0.30 max
Molybdenum	0.29 ±0.03	0.25-0.35
Nickel	0.006 ±0.005	0.30 max
Copper	0.008 ±0.05	0.30 max

Table 4.2: Chemical analysis of tubing samples from Station B

Element	Weight %	Specification for A106M Grade B as per ASTM A106/106M (2018)
Carbon	0.17 ±0.02	0.30 max
Manganese	0.72 ±0.05	0.29-1.06
Sulphur	0.005 +0.003	0.035 max
Phosphorus	0.009 +0.005	0.035 max
Silicon	0.24 ±0.05	0.10 min
Chromium	0.05 ±0.05	0.40 max
Molybdenum	0.06 ±0.03	0.15 max
Nickel	0.15 ±0.005	0.40 max
Copper	0.18 ±0.05	0.40 max

Table 4.3: Chemical analysis of tubing samples from Stations C

Element	Weight %	Specification for A105M as per ASTM A105/105M (2018)
Carbon	0.15 ±0.02	0.35 max
Manganese	1.09 ±0.10	0.60-1.05
Sulphur	0.047 +0.005	0.040 max
Phosphorus	0.024 +0.005	0.035 max
Silicon	0.22 ±0.05	0.10-0.35
Chromium	0.12 ±0.05	0.30 max
Molybdenum	0.03 ±0.03	0.12 max
Nickel	0.12 ±0.005	0.40 max
Copper	0.250 +0.05	0.40 max

4.1.3 Hardness Values

The average hardness of the tubing, calculated by considering four indentations, was estimated at 135-158 HV, 131-143 HV, and 142-147 HV on the fireside of stations A, B and C respectively. The hardness on the coldside was estimated at 139-146 HV, 126-150 HV, and 140-147 HV for stations A, B and C respectively. Calibration was done using a 109 HV Yamamoto hardness test block. The average hardness reading obtained on the calibration block, after six indentations, was 108 HV_{10kg} which confirms an error margin of +1 HV. Tables 4.4, 4.5 and 4.6 show that the hardness values measured w well within the standard specifications of 16Mo3, SA106 and SA105 respectively.

Table 4.4: Hardness values of station A measured at HV_{10}.

Reading Number	**Unit 1**		**Unit 2**		**Unit 3**		**Unit 4**	
	Coldside	Fireside	Coldside	Fireside	Coldside	Fireside	Coldside	Fireside
1	143	152	146	141	143	152	139	146
2	138	142	139	150	152	157	142	135
3	151	155	145	140	143	168	133	131
4	135	147	144	144	-	155	145	130
Harness Average	**141+1**	**149+1**	**143+1**	**143+1**	**146+1**	**158+1**	**139+1**	**135+1**
Hardness standard specifications converted from UTS as per BS EN 10216-2 (2013) is 131- 186 HV.								

The hardness of 164 HV, which is higher than the average, but still within the standard specification, was measured in the vicinity of the ruptured area on the tube from station A. This confirms that transformation and strain hardening occurred at this location.

Table 4.5: Hardness values of station B measured at HV_{10}.

Reading Number	**Unit 1**		**Unit 3**		**Unit 8**		**Unit 10**	
	Coldside	Fireside	Coldside	Fireside	Coldside	Fireside	Coldside	Fireside
1	130	128	147	144	159	138	124	145
2	133	129	146	136	150	141	126	141
3	131	131	143	136	147	146	126	135
4	135	131	141	140	146	148	131	139
Hardness Average	**132+1**	**131+1**	**144+1**	**139+1**	**150+1**	**143+1**	**126+1**	**140+1**
Hardness standard specifications converted from UTS as per ASTM A106 / 106M (2018) is 147HV maximum.								

Table 4.6: Hardness values of station C measured at HV_{10}.

Reading Number	**Unit 4**		**Unit6**	
	Coldside	Fireside	Coldside	Fireside
1	140	134	148	145
2	145	138	145	143
3	136	156	151	151
4	-	-	146	152
Hardness Average	**140+1**	**142+1**	**147+1**	**147+1**
Hardness standard specifications converted from UTS as per ASTM A105/105M (2018) is 197 HV maximum.				

4.1.4 Microstructural Examination

The microstructure observed on tubing from the three power stations was the same on both fireside and coldside; it consisted of well-spheroidised and degenerated carbides, still grouped in the original pearlitic pattern, in a ferrite matrix. A spheroidised microstructure is typical of service exposed 16Mo3 tubing operating at moderately elevated temperatures. A similar appearance between the fireside and coldside indicates that the flame-exposed (fire-) side of the tubing was not significantly hotter than the casing (cold-) side. The exception was seen on the ruptured areas which consisted of deformed grains.

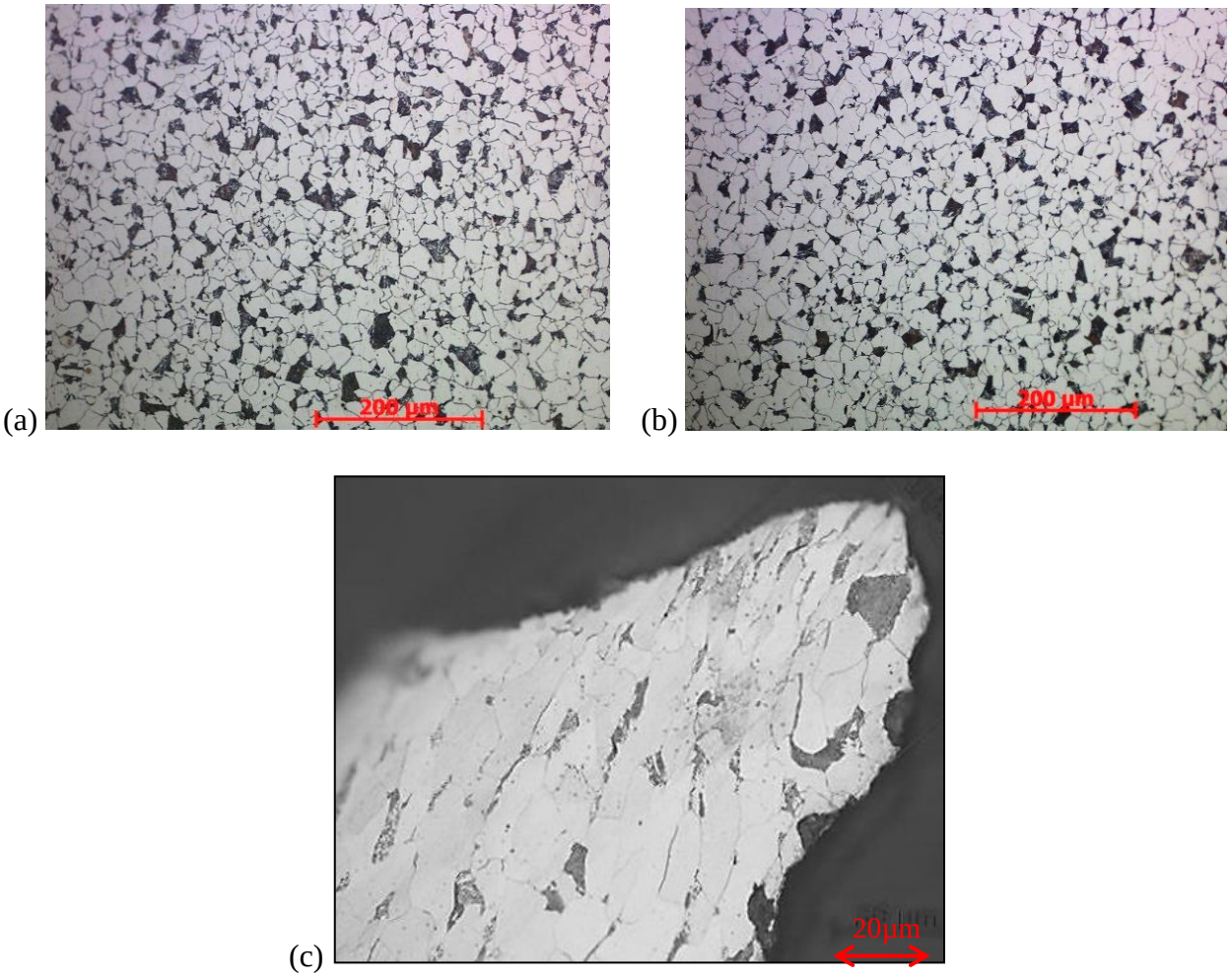

Figure 4.6: Station A side wall tubing (a) on the fireside, (b) on the coldside and (c) at failure showing deformation.

(a) 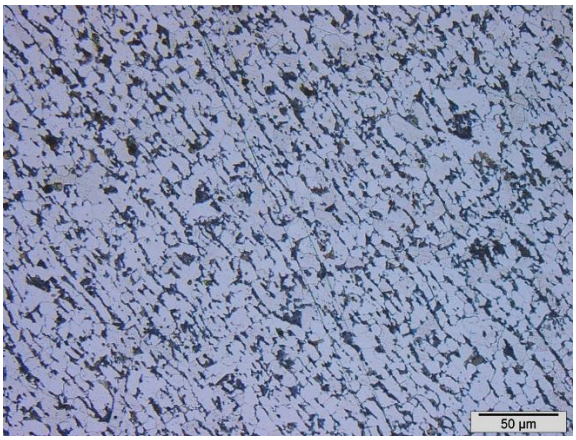

(b) 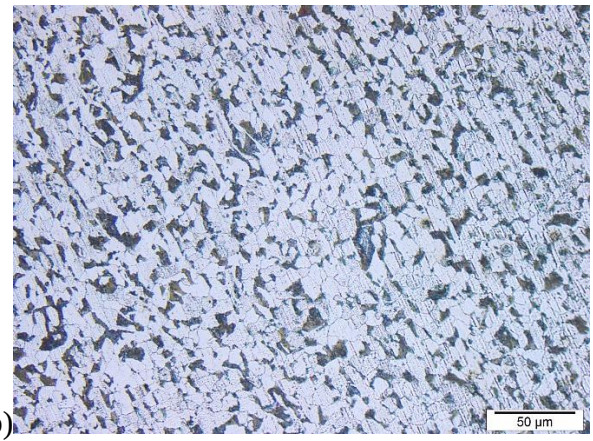

Figure 4.7: Station B front wall tubing (a) on the fireside and (b) on the coldside.

(a) 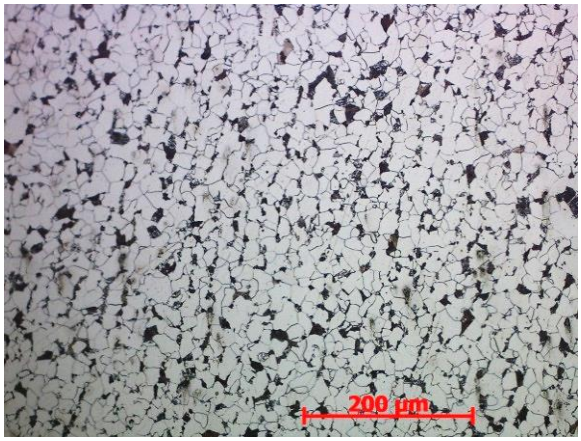

(b) 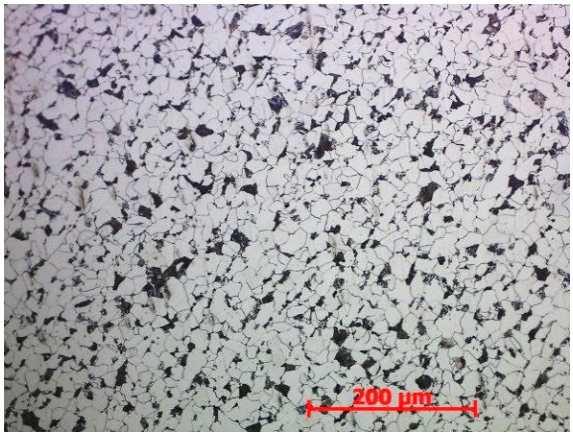

Figure 4.8: Station C side wall tubing (a) on the fireside and (b) on the coldside.

4.2 DEPOSIT ANALYSIS

Fireside deposits on the tubing surfaces from Station A, B and C were examined under light microscopy and a three layered deposit was observed on all the tubes with thicknesses as high as 0.97 mm, 0.60 mm and 0.57 mm respectively. Subsequently, the fireside deposit was analysed with SEM-EDS, QEMSCAN, XRD and DTA and the results are presented in sections 4.2.1 to 4.2.4.

4.2.1 SEM – EDS Analysis of the Fireside Deposit

A three layered fireside deposit was consistently seen in all the tubing samples from the three power stations. Similar elemental profile was revealed by EDS mapping of the fireside deposit from stations A, B and C. High concentration of oxygen was measured in the thin inner layer at the interface of the steel, as well as in the outer layer. Sulphur was concentrated in the middle layer of the fireside deposit.

4.2.1.1 Station A

The SEM analyses for units 3, 1 and 4 in station A respectively are presented in Figures 4.9, 4.10 and 4.11 and show the following distribution of elements in the fireside deposits:

Inner layer: High concentration of iron and oxygen.

Middle layer: High iron and moderate sulphur and oxygen.

Outer layer: High levels of iron, moderate sulphur and oxygen with low concentration of Al, Si, and Ca (fly ash particles).

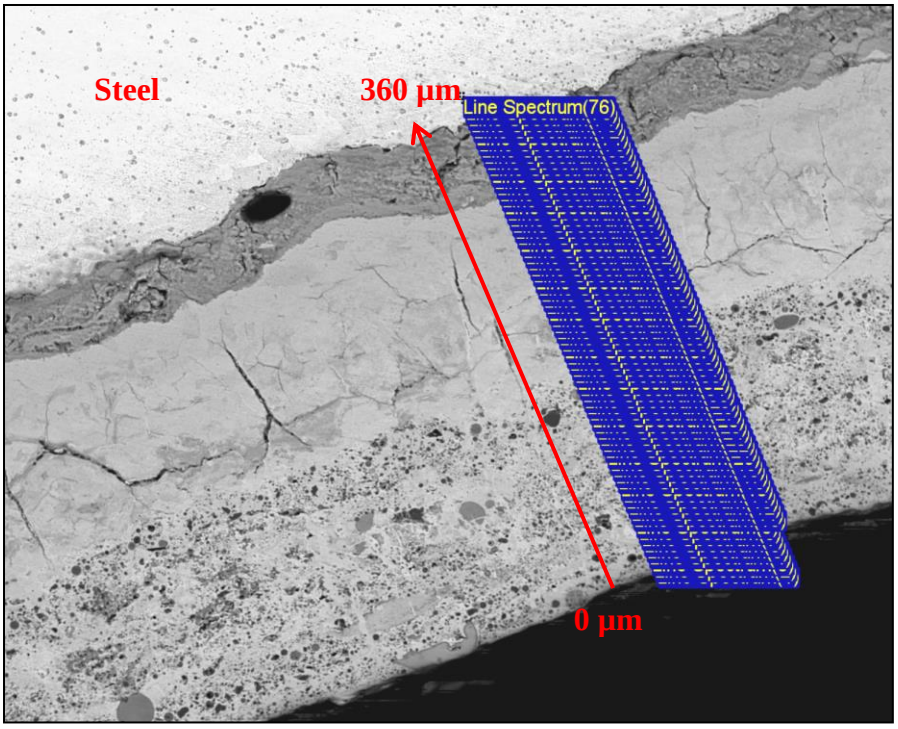

(a)

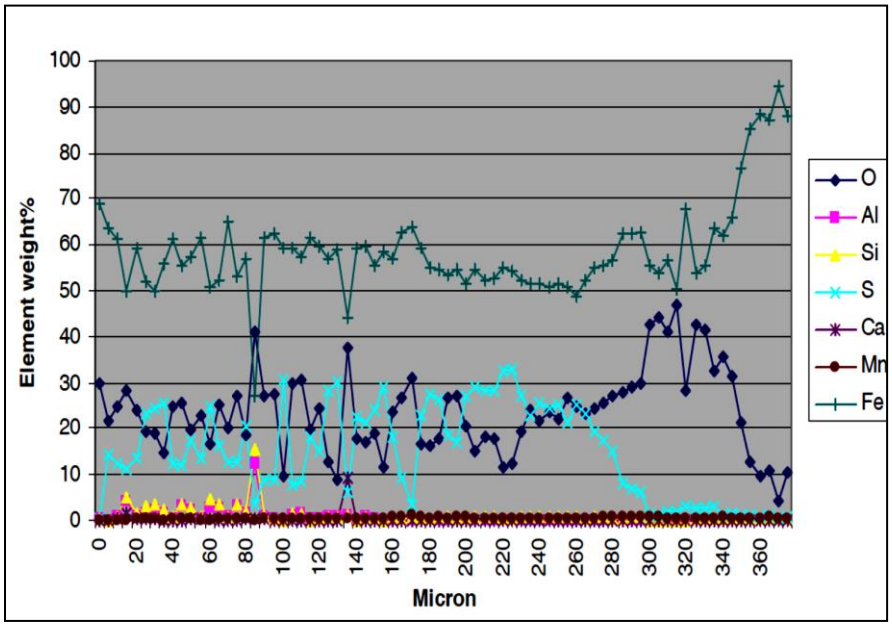

(b)

Figure 4.9: Station A Unit 3 sidewall tube showing (a) line map of the fireside deposit and (b) Elemental distribution in the fireside deposit as per EDS line map.

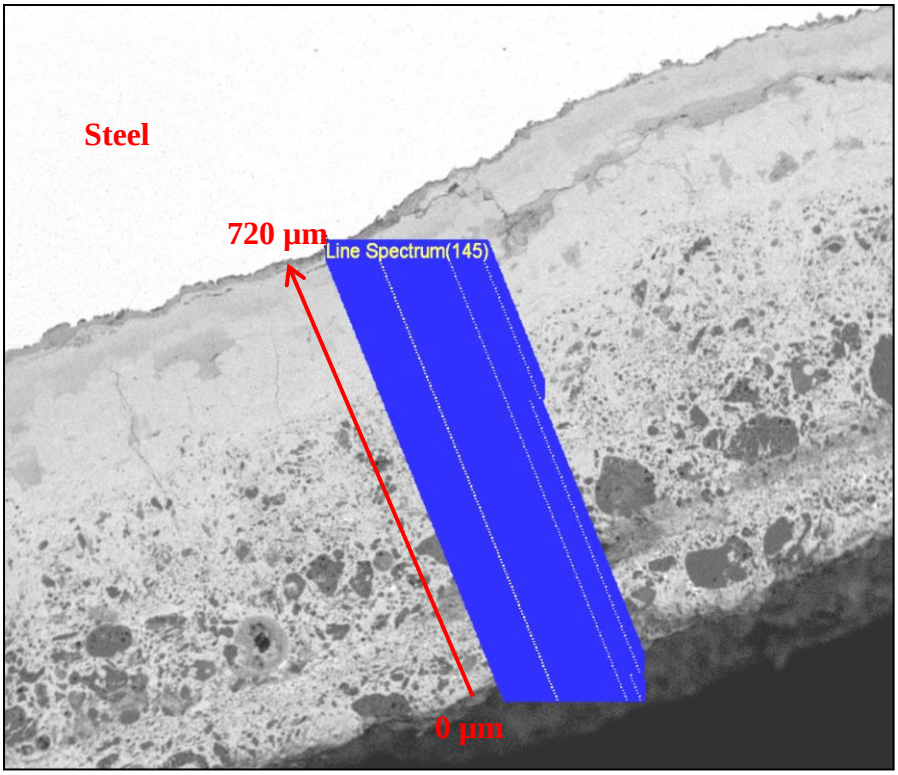

(a)

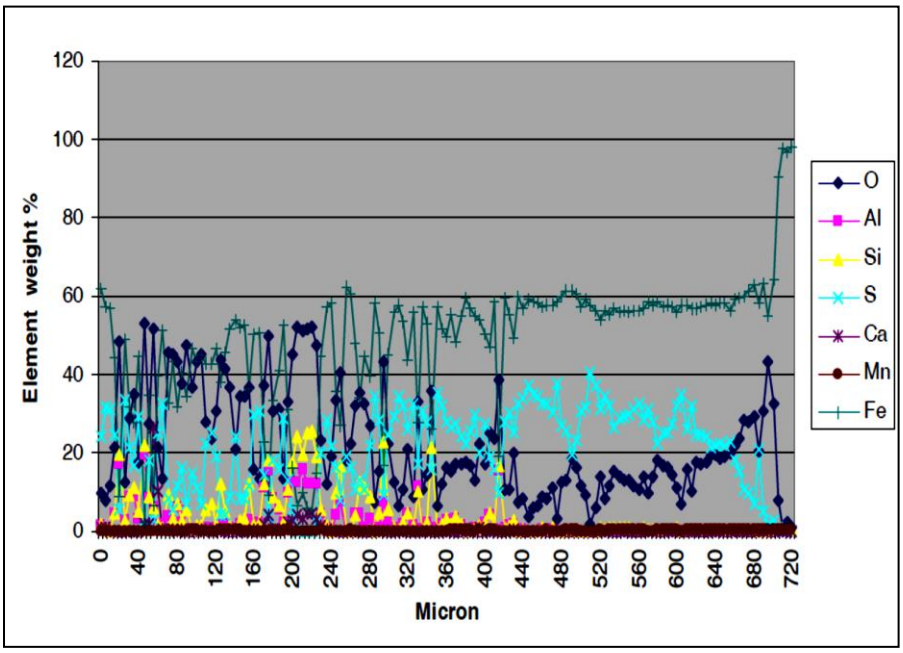

(b)

Figure 4.10: Station A Unit 1 sidewall tube showing (a) EDS line map of the fireside deposit and (b) Elemental distribution in the fireside deposit as per EDS line map.

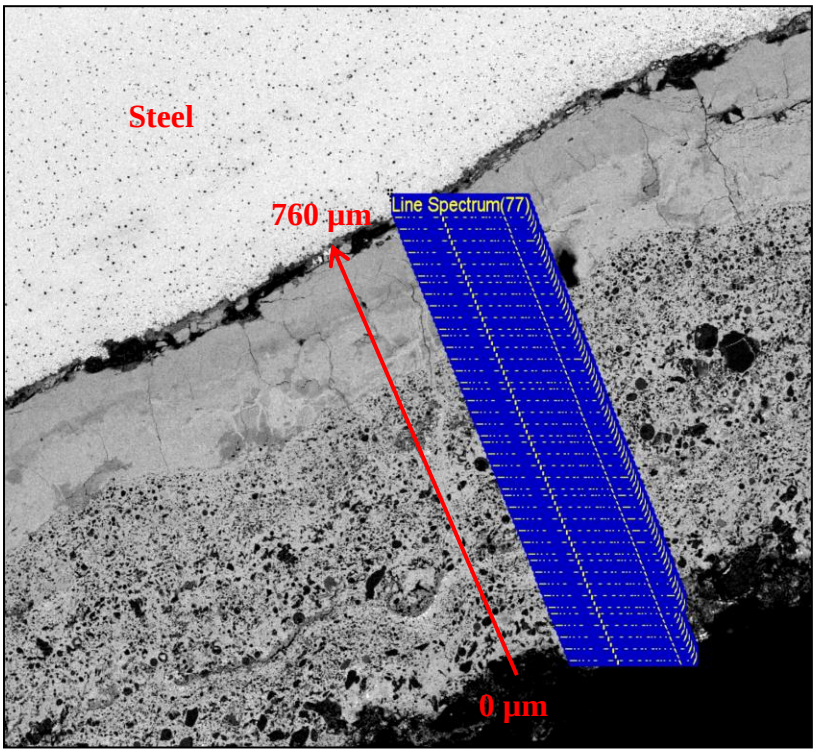

(a)

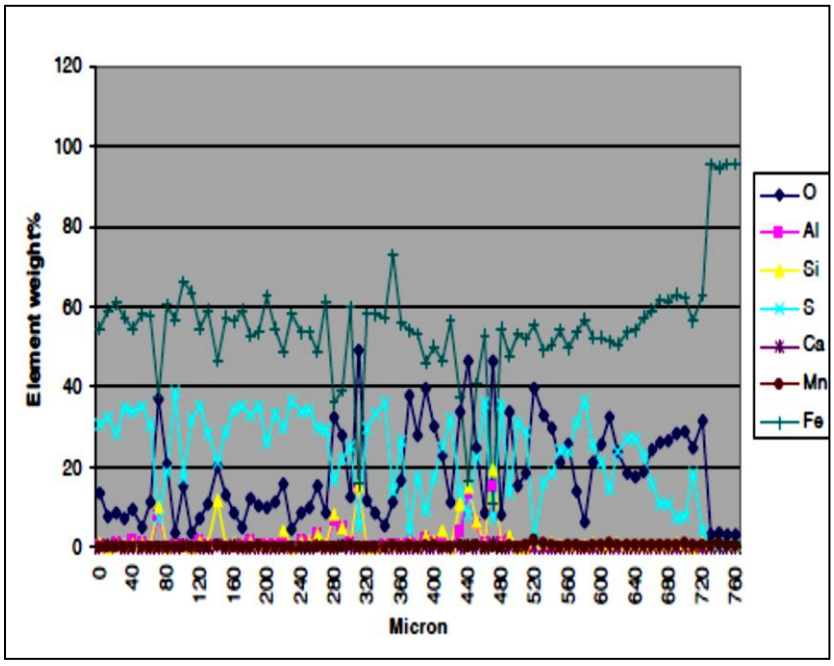

(b)

Figure 4.11: Station A Unit 4 sidewall tube showing (a) EDS line map of the fireside deposit and (b) Elemental distribution in the fireside deposit as per EDS line map.

4.2.1.2 Station B

Figures 4.12, 4.13 and 4.14 show SEM analyses of tubing from units 8, 3, and 1 in Station B respectively, and this showed the following with the following elemental distribution in the fireside deposits:

Inner layer: High concentration of iron and oxygen, and low levels of sulphur.

Middle layer: High iron and oxygen, with moderate to high concentration of sulphur.

Outer layer: High levels of iron, and low to moderate levels of oxygen sulphur.

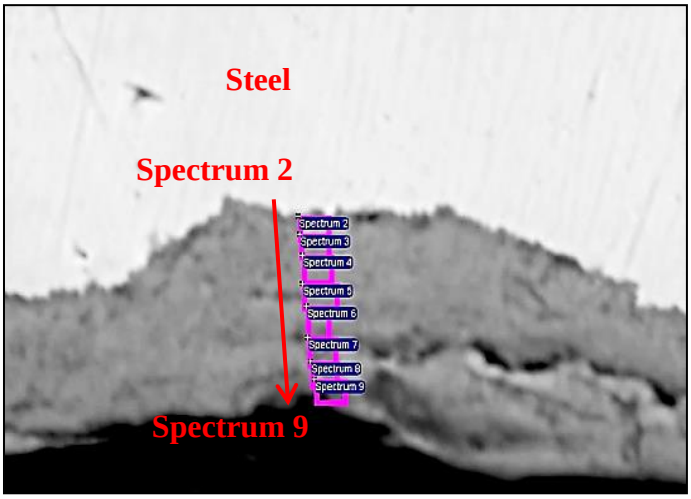

(a)

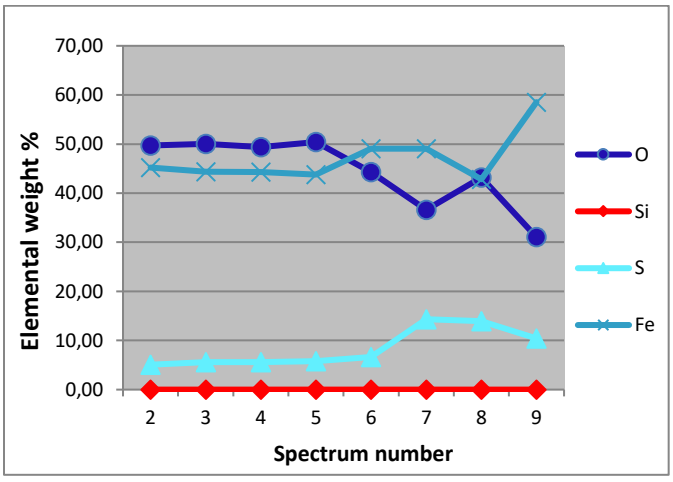

(b)

Figure 4.12: Station B Unit 8 sidewall tube showing (a) EDS line map of the fireside deposit and (b) Elemental distribution in the fireside deposit as per EDS line map.

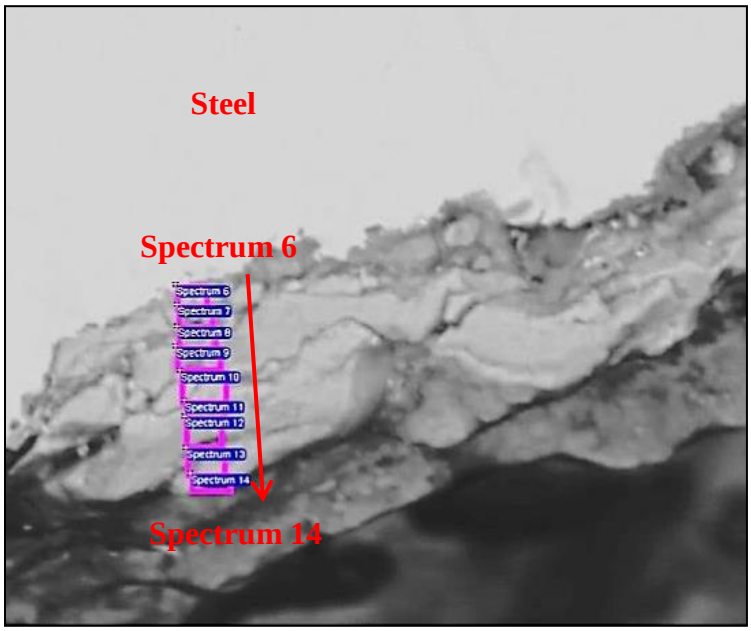

(a)

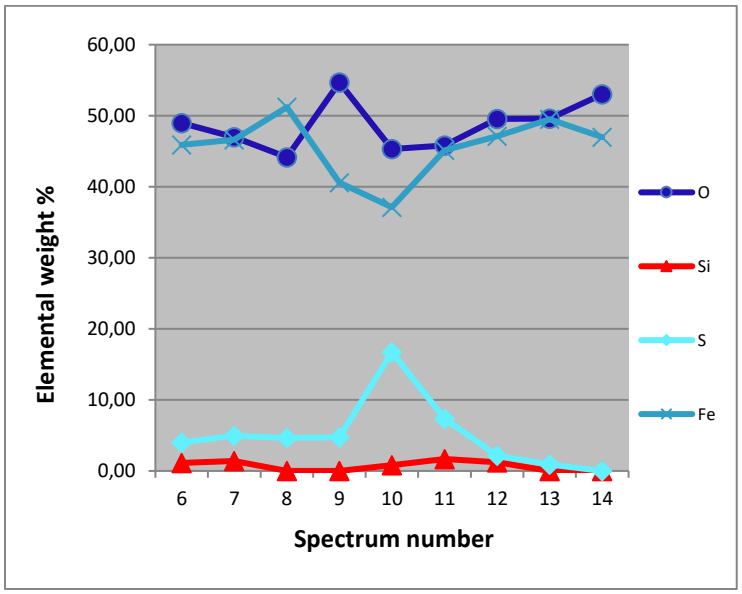

(b)

Figure 4.13: Station B Unit 3 sidewall tube showing (a) EDS line map of the fireside deposit and (b) Elemental distribution in the fireside deposit as per EDS line map.

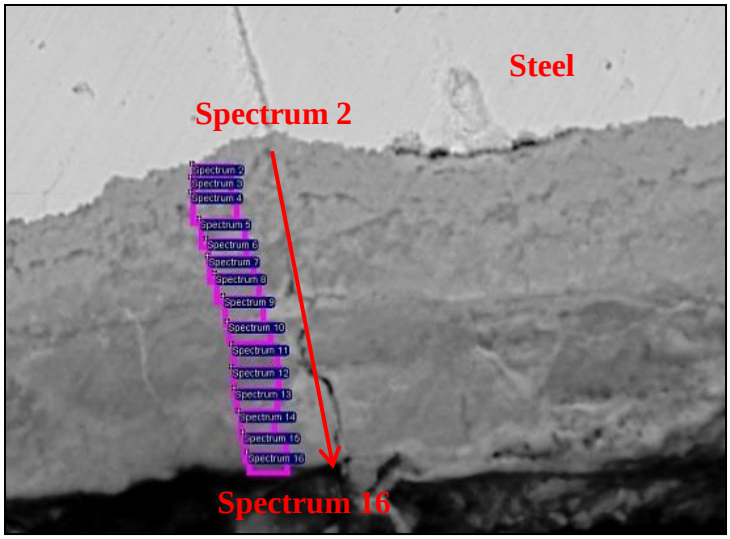

(a)

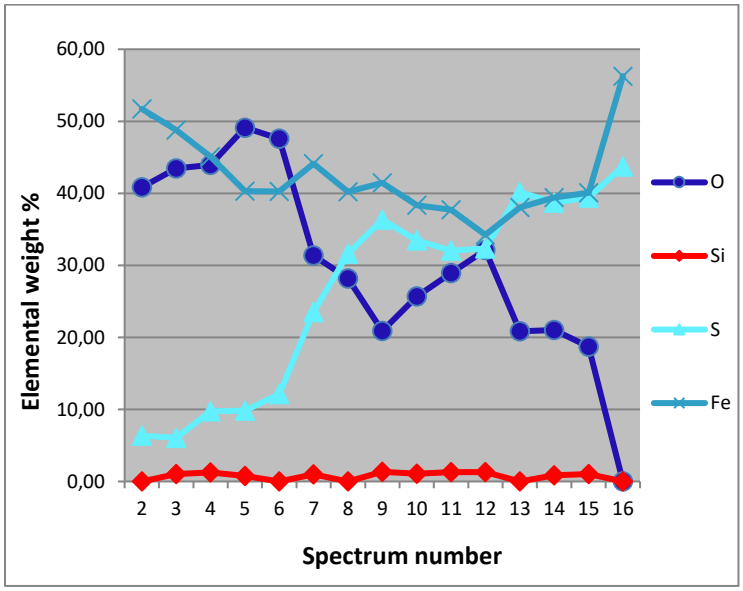

(b)

Figure 4.14: Station B Unit 1 sidewall tube showing (a) EDS line map of the fireside deposit and (b) Elemental distribution in the fireside deposit as per EDS line map.

4.2.1.3 Station C

Figures 4.15 and 4.16 show SEM analyses of tubing from units 4 and 6 in Station C respectively, and this showed the following with the following elemental distribution in the fireside deposits:

Inner layer: High concentration of iron and low oxygen and sulphur.

Middle layer: High iron and moderate sulphur and oxygen.

Outer layer: High levels of iron, moderate oxygen and low sulphur, traces of Si and Al.

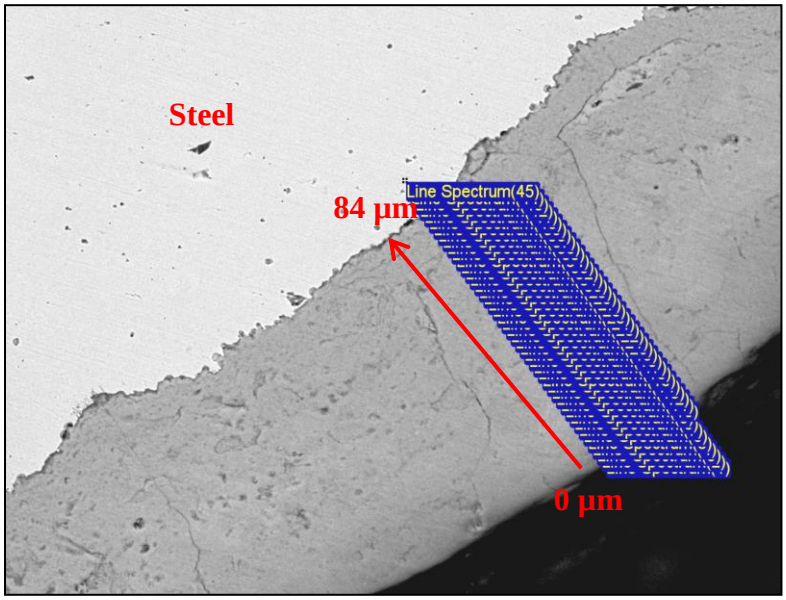

(a)

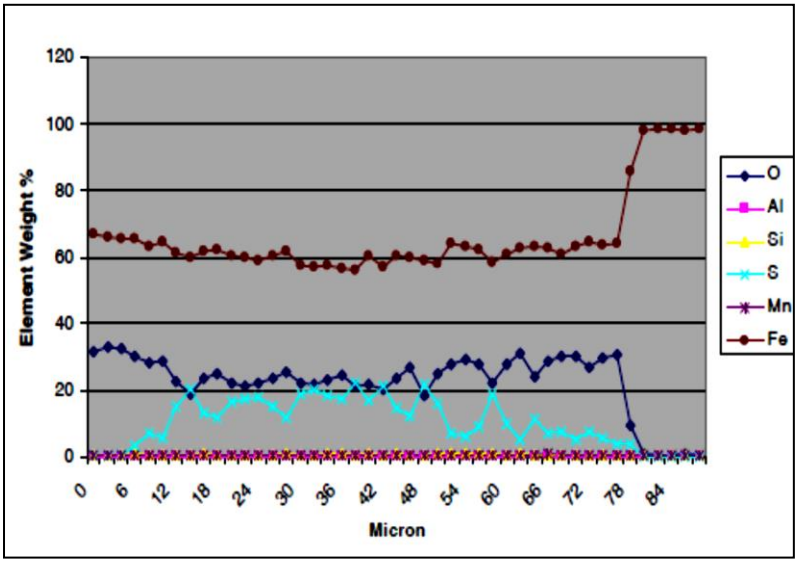

(b)

Figure 4.15: Station C Unit 4 sidewall tube showing (a) EDS line map of the fireside deposit and (b) Elemental distribution in the fireside deposit as per EDS line map.

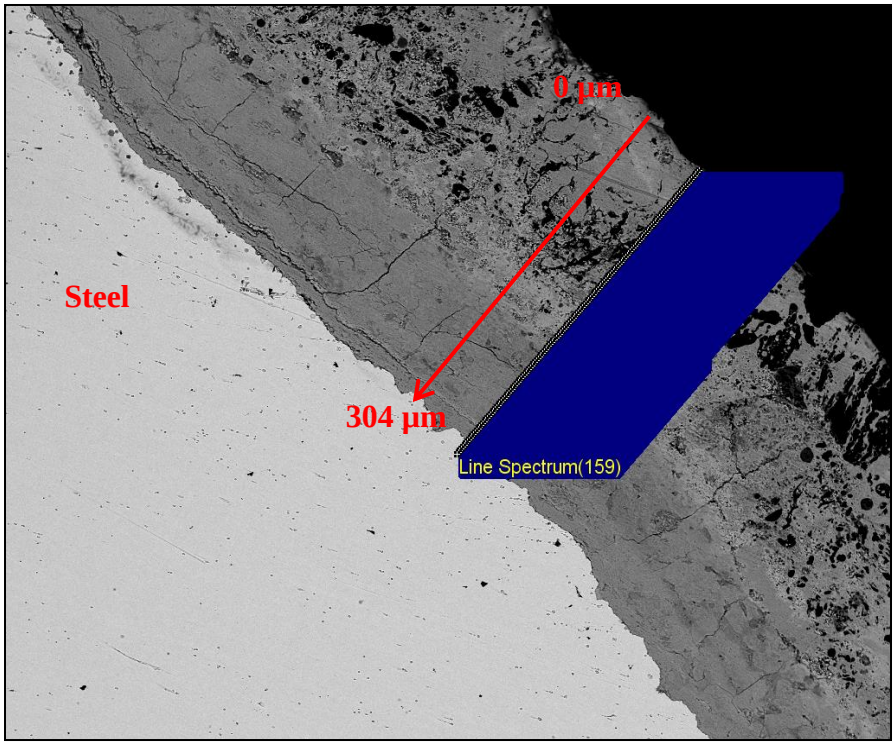

(a)

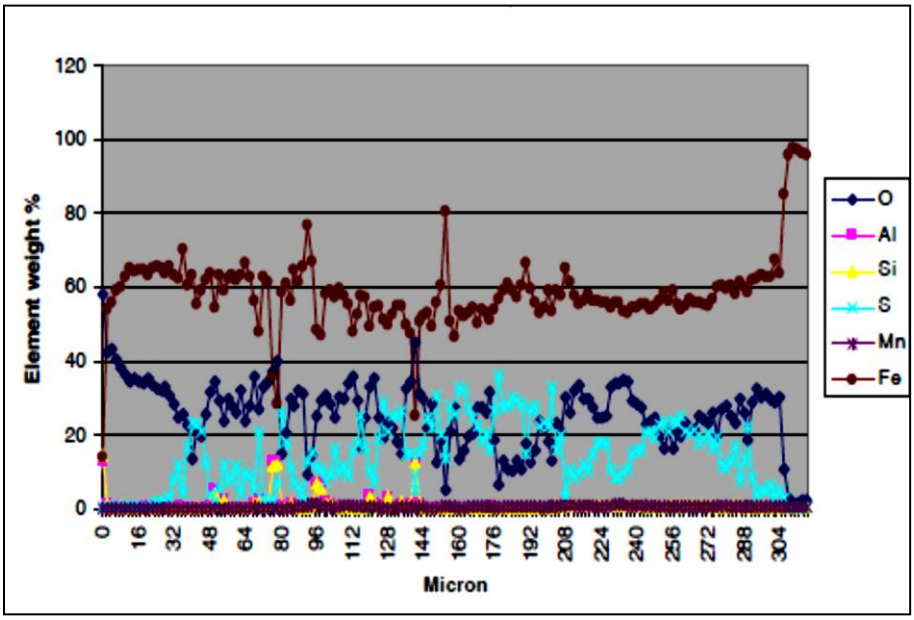

(b)

Figure 4.16: Station C Unit 6 sidewall tube showing (a) EDS line map of the fireside deposit and (b) Elemental distribution in the fireside deposit as per EDS line map.

4.2.2 QEMSCAN

QEMSCAN analyses were performed on tubes from Stations A and C due to limited number of samples, the mineralogy of Station B was analysed with XRD only. The analyses were performed on both fire- and cold- sides of the tubes.

4.2.2.1 Station A

A consistent thick Fe-sulphide rich layer was detected in the inner and middle layers of station A's fireside deposit. These results correlate with the findings of high iron and sulphur concentrations in the middle and innermost layers detected by SEM-EDS analysis. The Fe-sulphide was measured in volume percentages ranging from 47 to 80 volume % for Station A and iron oxide (hematite and magnetite) was in levels of 4 to 49 volume%. The concentration of fly ash particles ranged from 3 to 14 volume % and the fireside deposit thickness was measured up to the maximum of 1.2 mm. The three Units of station A had three layered fireside deposits with the following morphology sequence:

Inner layer ⟶ Outer layer

Unit 1: Fe-sulphide — Fe-sulphide + Fe-oxide — Fe-sulphide + Fe-oxide + FA, as shown by Figure 4.17 and 4.18.

Unit 3: Fe-sulphide — Fe-sulphide + Fe-oxide + FA — Fe-oxide + FA, as illustrated by Figure 4.19 and 4.20.

Unit 4: Fe-oxide + Fe-sulphide — Fe-sulphide — Fe-oxide + FA, as indicated in Figure 4.21 and 4.22.

FA = varying proportions of embedded fly ash particles such as aluminosilicate, kaolinite, quartz, calcite.

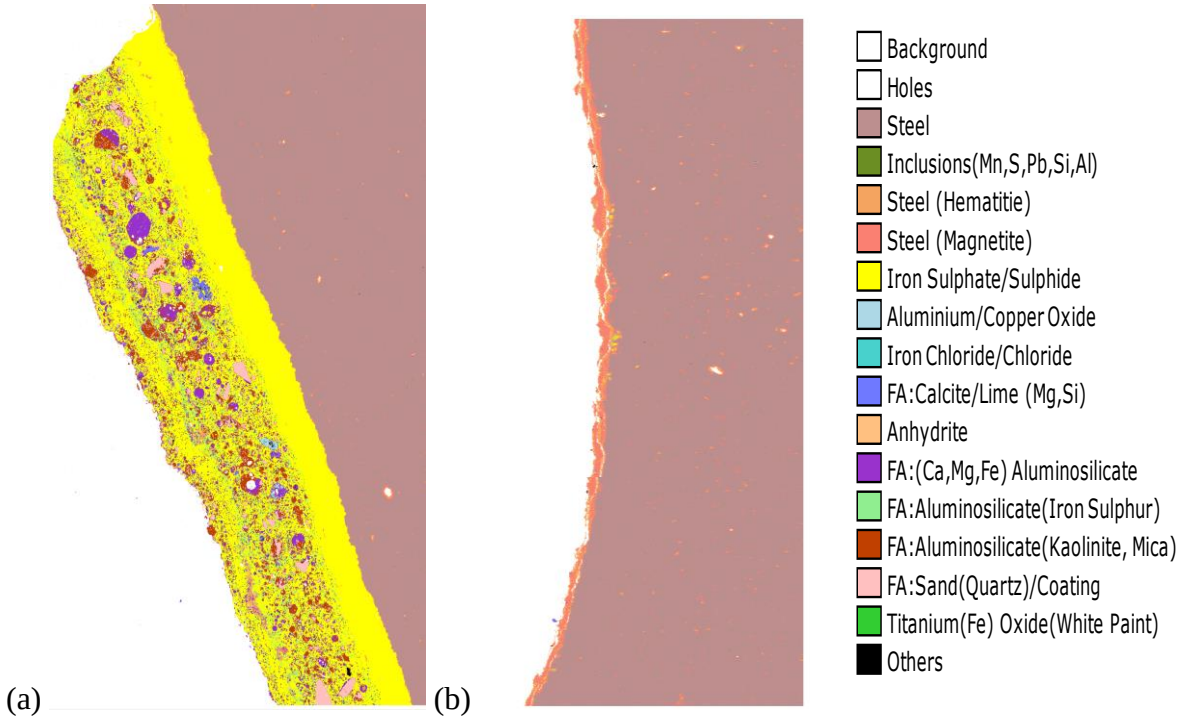

Figure 4.17: Qualitative image presentation of mineralogy composition in the deposit on (a) fireside and (b) non-fireside surfaces of Station A Unit 1 tubing.

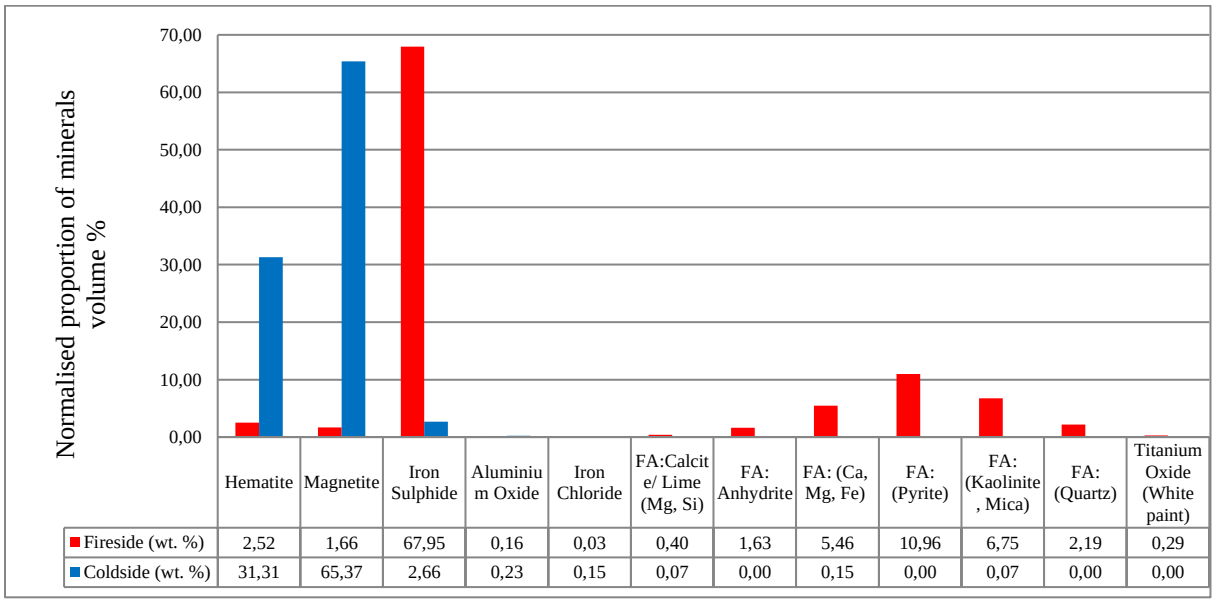

	Hematite	Magnetite	Iron Sulphide	Aluminium Oxide	Iron Chloride	FA:Calcite/ Lime (Mg, Si)	FA: Anhydrite	FA: (Ca, Mg, Fe)	FA: (Pyrite)	FA: (Kaolinite, Mica)	FA: (Quartz)	Titanium Oxide (White paint)
Fireside (wt. %)	2,52	1,66	67,95	0,16	0,03	0,40	1,63	5,46	10,96	6,75	2,19	0,29
Coldside (wt. %)	31,31	65,37	2,66	0,23	0,15	0,07	0,00	0,15	0,00	0,07	0,00	0,00

Figure 4.18: Quantitative mineralogy estimates of fireside and non-fireside deposits of Station A Unit 1 sidewall tubing.

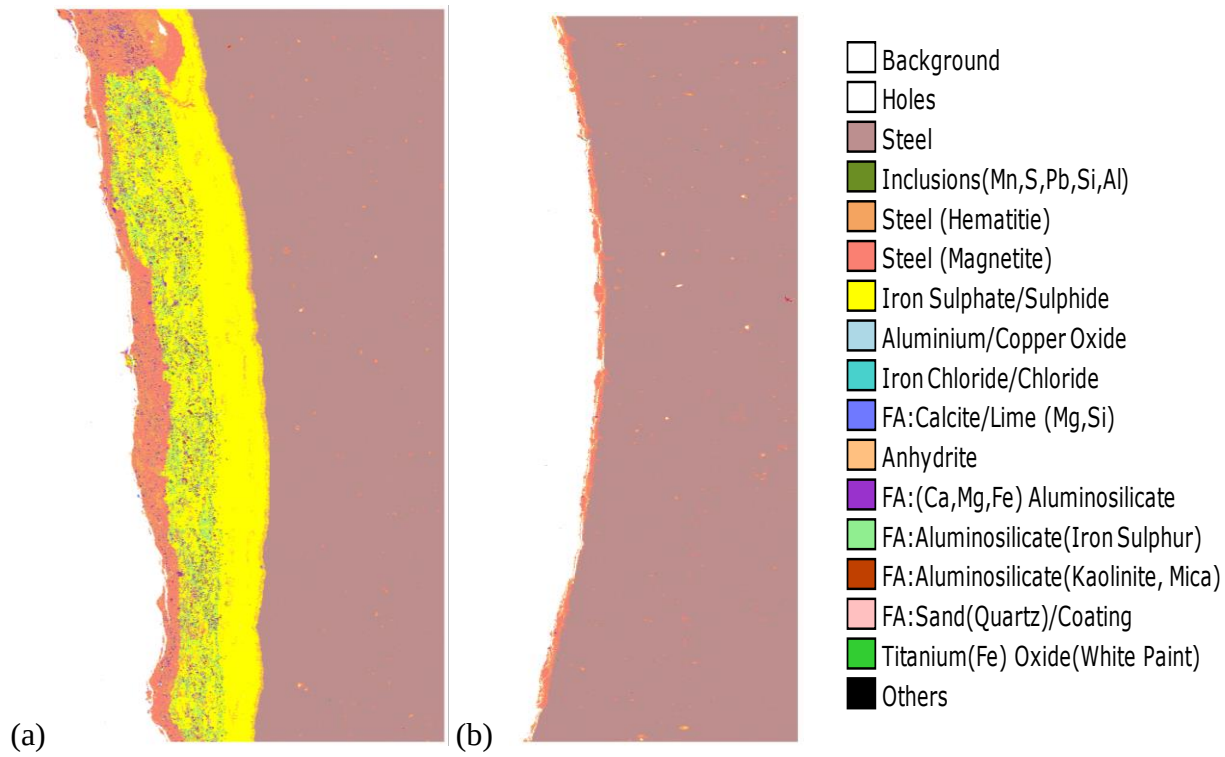

Figure 4.19: Qualitative image presentation of mineralogy composition in the deposit on (a) fireside, (b) coldside surfaces of Station A Unit 3 tubing.

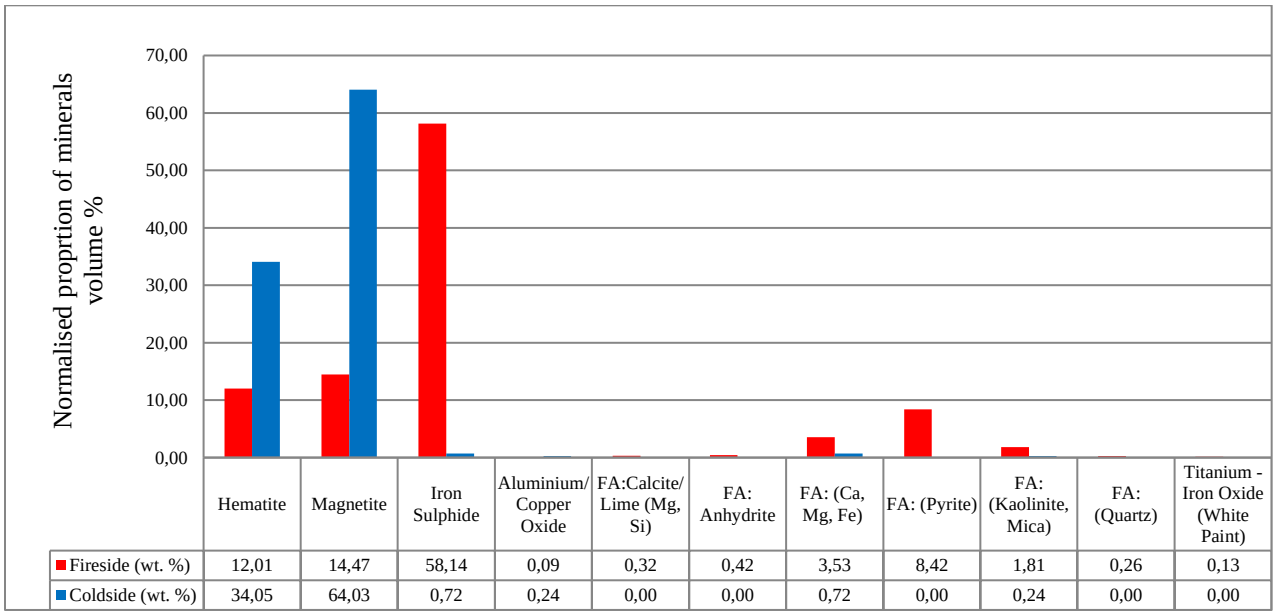

	Hematite	Magnetite	Iron Sulphide	Aluminium/ Copper Oxide	FA:Calcite/ Lime (Mg, Si)	FA: Anhydrite	FA: (Ca, Mg, Fe)	FA: (Pyrite)	FA: (Kaolinite, Mica)	FA: (Quartz)	Titanium - Iron Oxide (White Paint)
Fireside (wt. %)	12,01	14,47	58,14	0,09	0,32	0,42	3,53	8,42	1,81	0,26	0,13
Coldside (wt. %)	34,05	64,03	0,72	0,24	0,00	0,00	0,72	0,00	0,24	0,00	0,00

Figure 4.20: Quantitative mineralogy estimates of fireside and coldside deposits of Station A Unit 3 sidewall tubing.

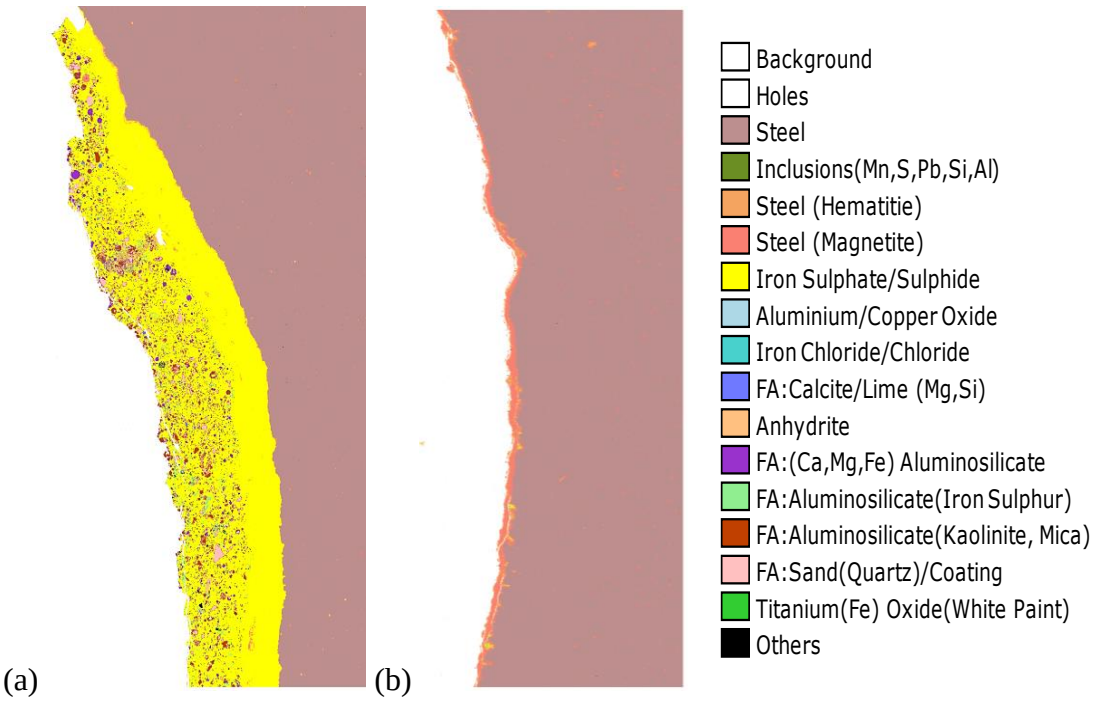

Figure 4.21: Qualitative image presentation of mineralogy composition in the deposit on (a) fireside, (b) coldside surfaces of Station A Unit 4 tubing.

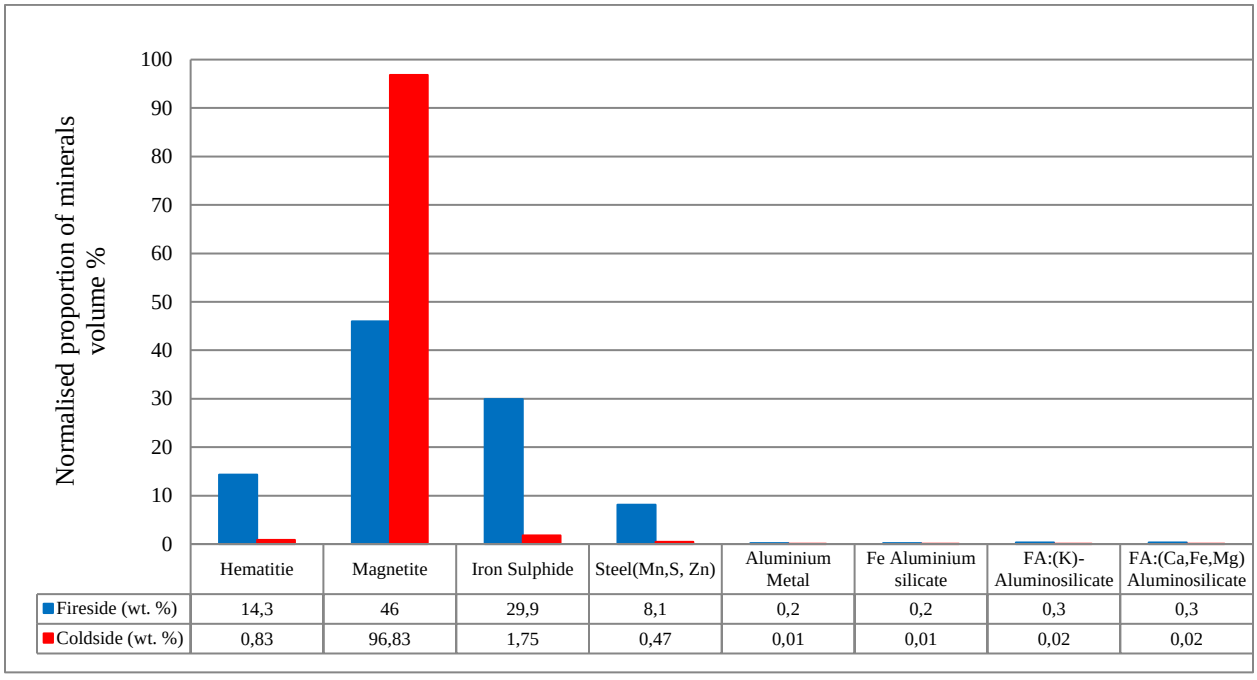

	Hematitie	Magnetite	Iron Sulphide	Steel(Mn,S, Zn)	Aluminium Metal	Fe Aluminium silicate	FA:(K)-Aluminosilicate	FA:(Ca,Fe,Mg) Aluminosilicate
Fireside (wt. %)	14,3	46	29,9	8,1	0,2	0,2	0,3	0,3
Coldside (wt. %)	0,83	96,83	1,75	0,47	0,01	0,01	0,02	0,02

Figure 4.22: Quantitative mineralogy estimates of fireside and coldside deposits of Station A Unit 4 sidewall tubing.

4.2.2.2 Station C

Similarly to station A, a three layered fireside deposit was also observed on Station C tubing samples with relatively thick Fe-sulphide rich layer detected in the inner and middle layers. These results are aligned with the findings of high iron and sulphur concentrations in the middle layers detected by SEM-EDS. The volume percentages of Fe-sulphide were measured as high as 67 to 69 volume %, while the iron oxide (hematite and magnetite) levels were in the range of 21 to 30 volume %. The concentration of fly ash particles ranged from 0.3 to 9 volume % and the fireside deposit thickness was measured to the maximum of 0.53 mm. Tubing of Unit 4 of Station C had three layered fireside deposits with the following sequence:

Inner layer ⟶ Outer layer

Unit 4: Fe-sulphide —— Fe-sulphide + Fe-oxide —— Fe-oxide + FA; as shown by Figure 4.23 and 4.24.

The morphology and composition of the fireside deposit from the two power stations, A and C, was found to be similar. The fireside deposit is three layered with iron sulphide rich inner layer formed on the surface of the steel, followed by the middle layer made up of a combination of iron sulphide and iron oxide, and covered by iron-oxide rich outer layer with fragments of fly ash particles (quartz (SiO_2), mullite ($Al_2(Al_3Si_2)O_{10}$) and ferrian ($Ca_3AlFeSi_2O_{12}$)). In all samples there was no evidence of sodium or potassium associated with the sulphur. The presence of sulphide phases, namely pyrrhotite and pyrite, coexisting with iron oxide is indicative of substoichiometric conditions in the furnace or on the tube surface.

Substoichiometric conditions are formed when there is limited oxygen (< 2%) in the furnace. Bakker, 2001, states that low excess O_2 favours the gasification process over combustion process. Gasification results in the formation of H_2S and limits oxidation of CO and combustion of pyrite (FeS_2). The high amounts of CO and H_2S favour a shift in the chemical equilibria for the sulphur species in the flue gas towards higher sulphur potentials and thus allow sulphidation of the metal to take place as well as oxidation (Bakker, 2001). A thicker but less protective deposit is then

formed on the metal surface which is largely composed of magnetite containing islands of iron sulphide, as is seen in the fireside deposit of Station A and C tubing. Sulphide deposits allow higher rates of transport (diffusion) of iron cations than oxides, the strength and adherence of the deposit decrease with increasing FeS content, while its growth rate and permeability increase significantly. These deposits are also brittle and poorly adherent, so they readily crack and spall. The result is increased metal wastage (i.e. wall thinning), which becomes the dominant factor in tube life.

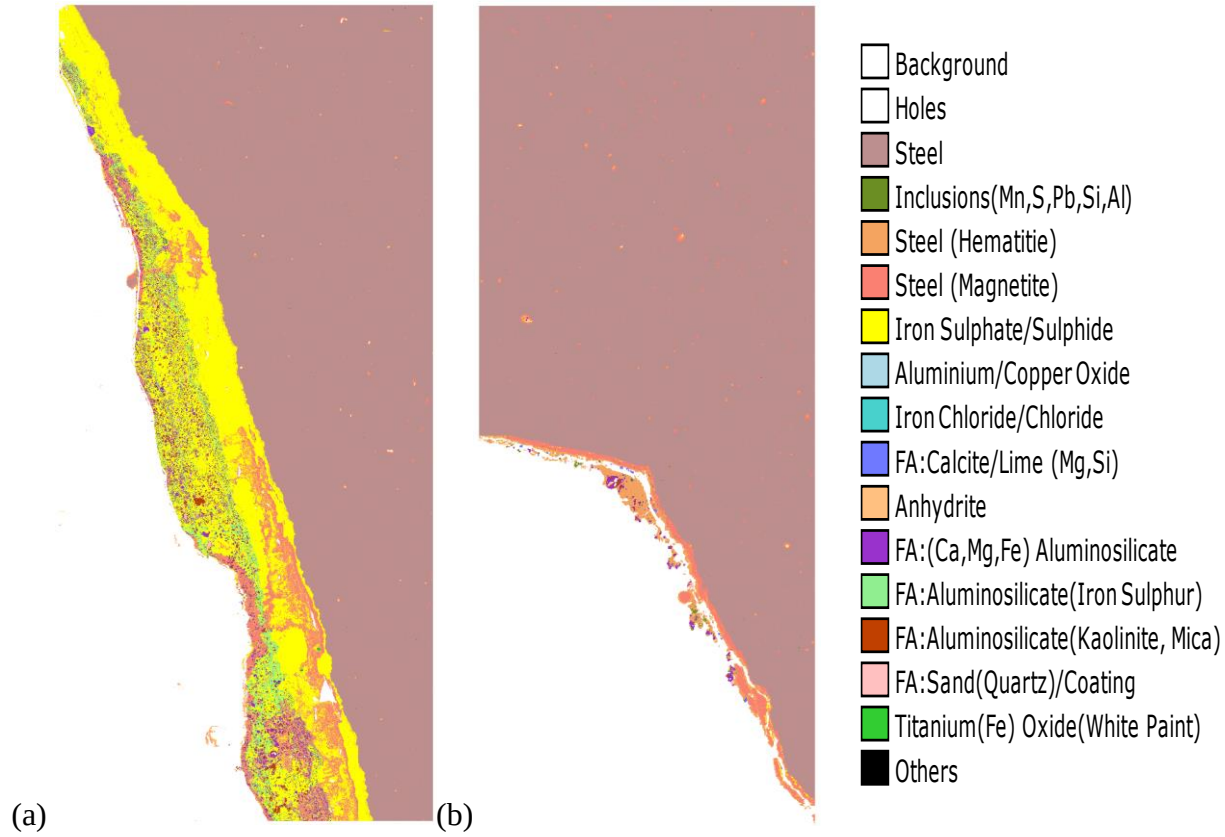

Figure 4.23: Qualitative image presentation of mineralogy composition in the deposit on (a) fireside, coldside surfaces of Station C Unit 4 tubing.

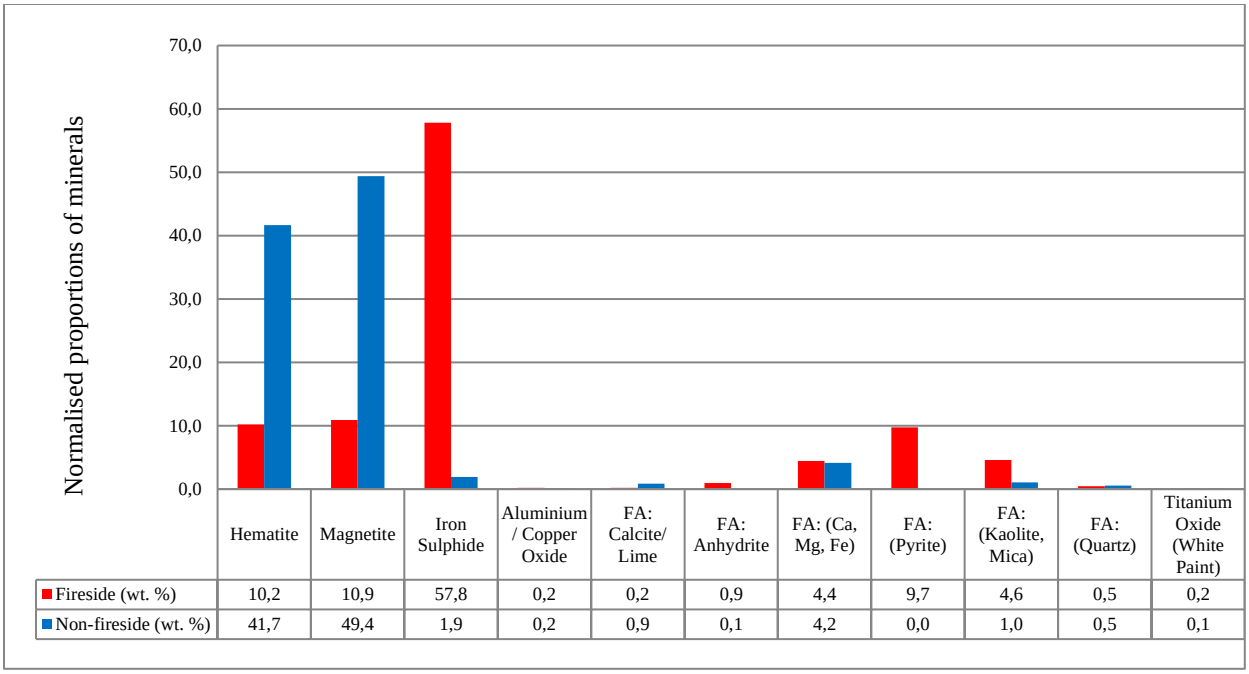

	Hematite	Magnetite	Iron Sulphide	Aluminium / Copper Oxide	FA: Calcite/ Lime	FA: Anhydrite	FA: (Ca, Mg, Fe)	FA: (Pyrite)	FA: (Kaolite, Mica)	FA: (Quartz)	Titanium Oxide (White Paint)
Fireside (wt. %)	10,2	10,9	57,8	0,2	0,2	0,9	4,4	9,7	4,6	0,5	0,2
Non-fireside (wt. %)	41,7	49,4	1,9	0,2	0,9	0,1	4,2	0,0	1,0	0,5	0,1

Figure 4.24: Quantitative mineralogy estimates of fireside and coldside deposits of Station C Unit 4 sidewall tubing.

4.2.3 X-Ray Diffraction (XRD)

The XRD analysis of Station A fireside corrosion deposit revealed the presence of iron-oxide and iron sulphide. Figure 4.25 and 4.26 show the XRD analysis results for station A; iron-oxide was in a form of Fe_2O_3 and Fe_3O_4, while iron-sulphide was detected as pyrrhotite in small quantities within a range of 1.4 - 3.7 weight %. Small to moderate quantities of quartz and mullite were also detected which is indicative of the presence of fly ash particles.

The fireside deposit on Station B's tubing consisted of iron-oxide predominantly as magnetite and low levels of hematite. Iron-sulphur rich phases detected include pyrrhotite, pyrite and traces of galena (PbS); fly ash particles were detected through mullite, quartz and jarosite ($K_2O.3Fe_2O_3.4SO_3.6H_2O$). For Unit 1, pyrrhotite was measured in small quantities ranging from 3.7 - 5.6 weight % as shown in Figure 4.27, whereas for Unit 3 high levels of pyrrhotite were measured in the range of 40 - 50 weight % as shown by Figure 4.28. The difference in the morphology of Unit 1 and Unit 3 fireside deposits may be an indication of the furnaces operating

under different combustion conditions. The high concentration of pyrrhotite in Unit 3 may be indicative of prolonged reducing conditions in the furnace and/or on the tube.

Both units of Station C showed fireside deposits consisting of predominantly pyrrhotite. Figure 4.29 shows low concentration of magnetite in Unit 4 and trace concentrations of ferrian. Analysis of Unit 6 revealed high magnetite concentration and low goethite (FeO(OH)) as shown by Figure 4.30. Only qualitative analysis was done on units 4 and 6. The difference in the morphology of units 4 and 6 fireside deposits is indicative of the furnaces operating under different combustion conditions. Unit 6 fireside deposits consisted of both high concentrations of pyrrhotite and iron oxide phases; this shows existence of both oxidising and reducing conditions. In Unit 4, it appears that substoichiometric conditions (i.e. mostly reducing) were in existence for a longer time, which resulted in high formation pyrrhotite and minimal iron oxide phases. The effect of fly ash is also shown through the detection of ferrian.

XRD analysis of the fireside deposit from the three power stations produced correlating results. High content of hematite and magnetite was detected with consistent detection of pyrrhotite. Fly ash particles were also identified (predominantly quartz and mullite) as well as coal constituents such as pyrite, galena and anglesite ($PbSO_4$).

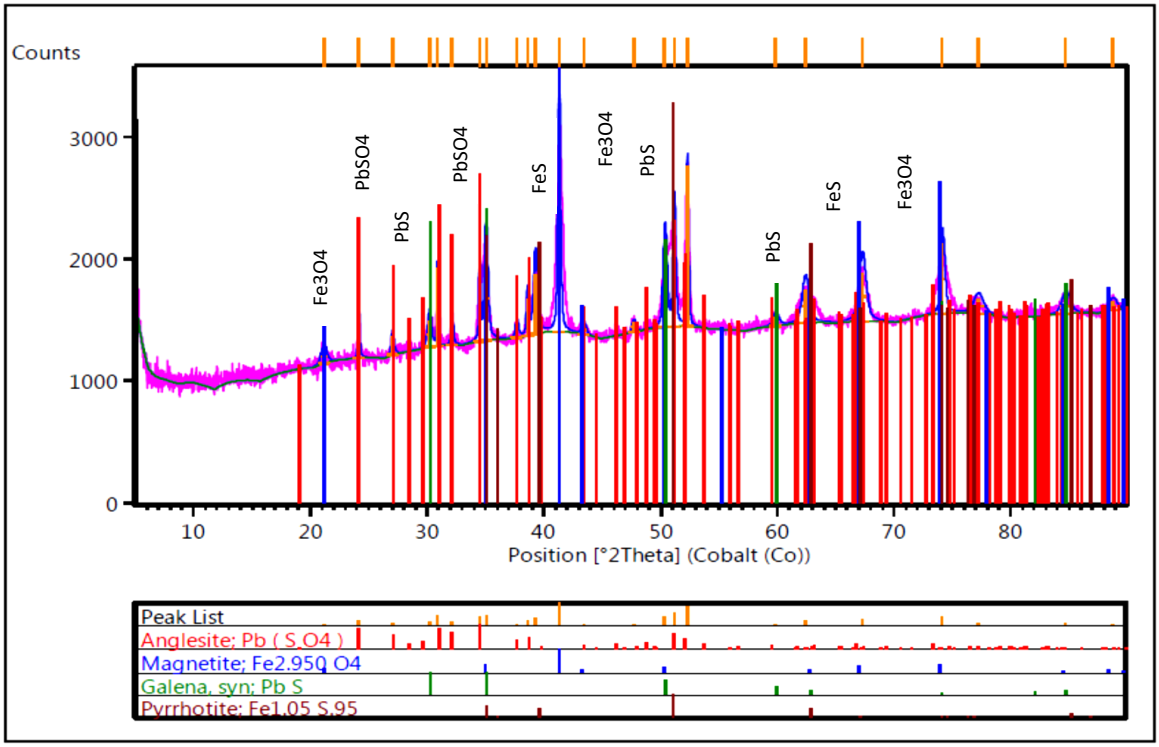

Figure 4.25: Analysis of front wall tube fireside deposit from Unit 2 of Station A.

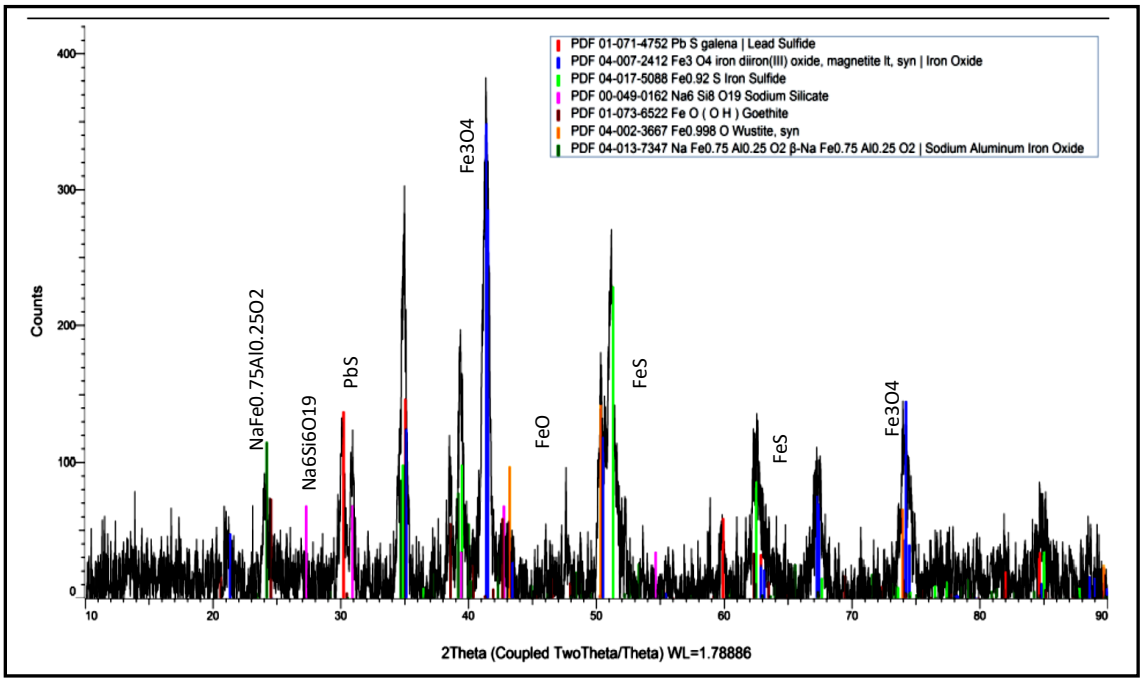

Figure 4.26: Analysis of sidewall tube fireside deposit from Unit 1 of Station A.

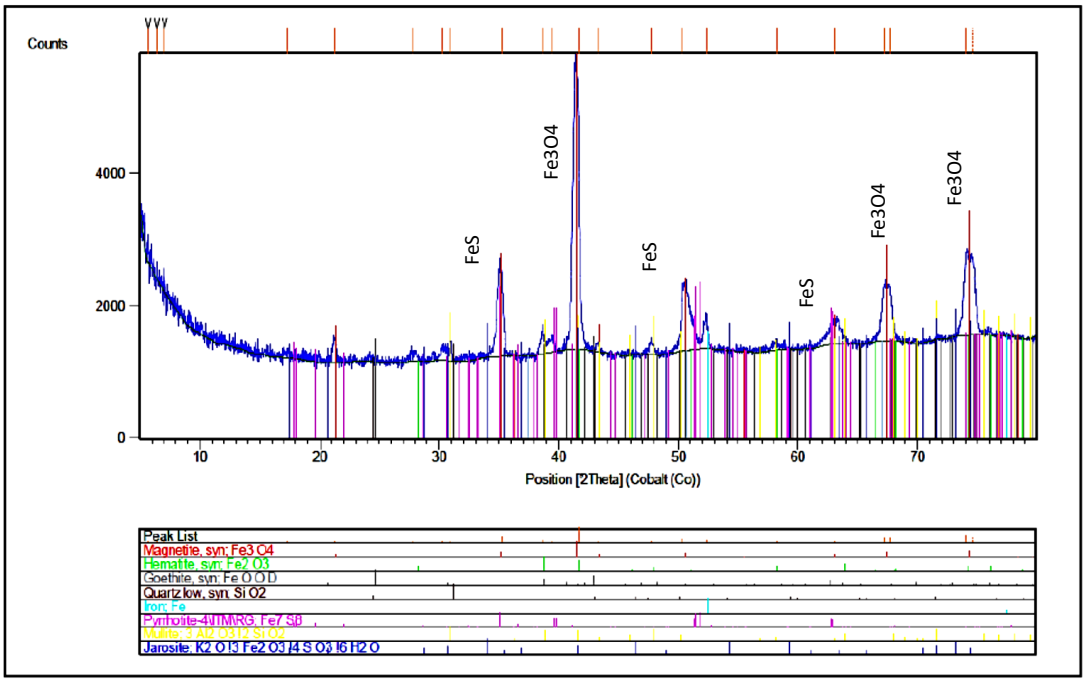

Figure 4.27: Analysis of the division wall tube fireside deposit from Unit 1 of Station B.

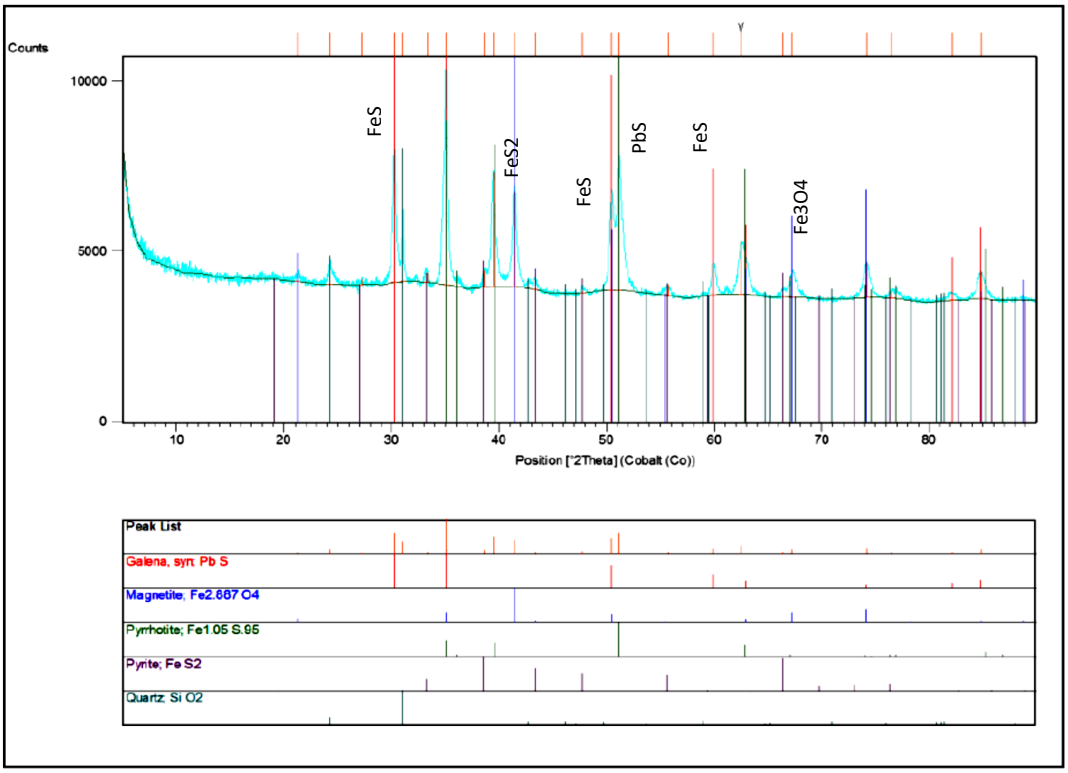

Figure 4.28: Analysis of the division wall tube fireside deposit from Unit 3 of Station B.

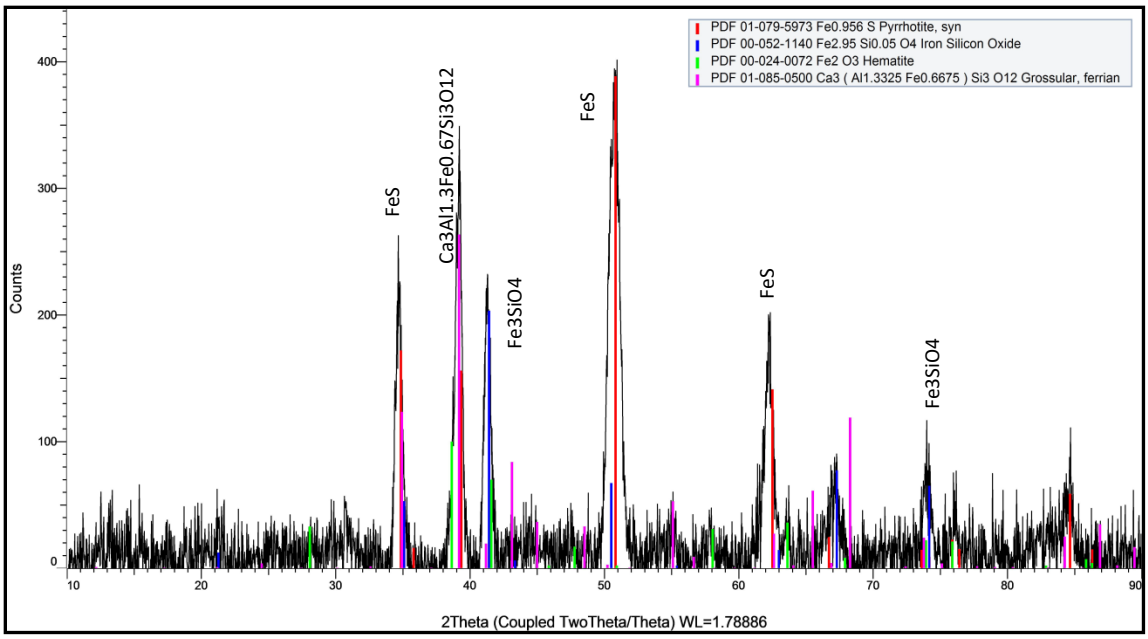

Figure 4.29: XRD analysis of sidewall tube fireside deposit from Unit 4 of Power Station C.

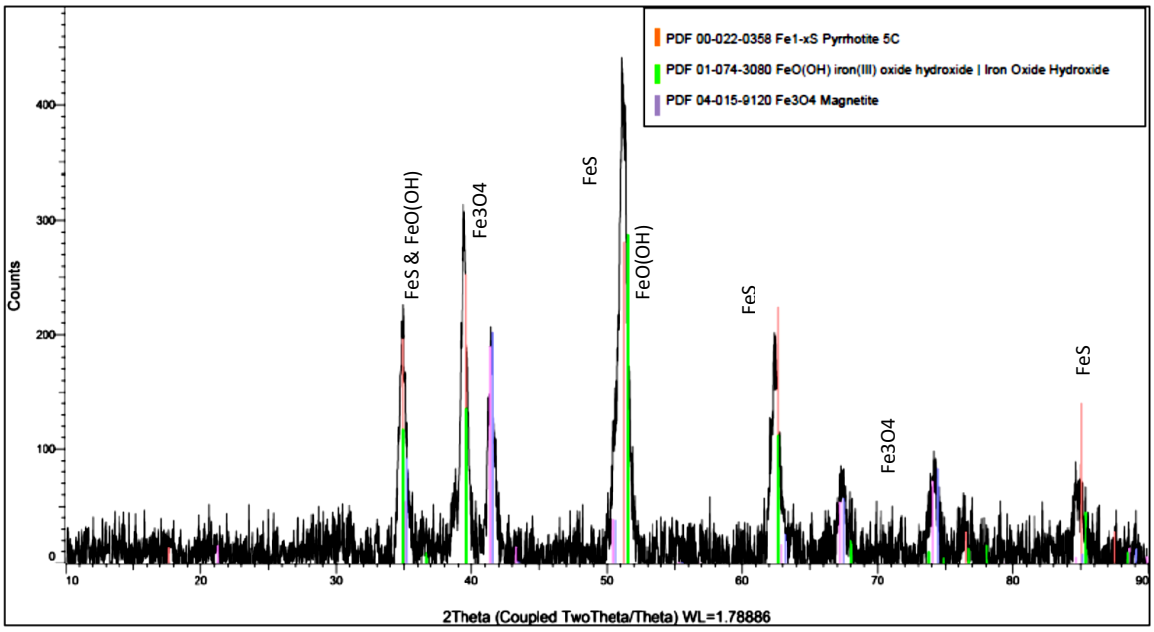

Figure 4.30: XRD analysis of sidewall tube fireside deposit from Unit 6 of Power Station C.

4.2.4 Differential Thermal Analysis (DTA)

Only samples from stations A and B were analysed with DTA. The thermal analysis of station A tubing showed peaks generally at temperatures ranging from 950 to 1250°C. The exception was seen on one tube where lower temperature activity was indicated at 565°C. A similar trend was observed on samples from station B; higher temperature peaks were detected at 977°C and 1240°C, while one lower temperature activity was indicated at 541°C, as shown by Figures 4.30 to 4.31.

The low temperature peaks, at 541 and 565°C, measured on the samples of station A and B are likely an indication of kaolinite transformation into metakaolinite which occurs at temperatures around 500°C and/or pyrite's oxidation into FeS and Fe_2O_3 which between 475°C and 525°C. The thermal peaks measured at higher than 900°C may be representation of metakaolinite transformation into other forms of aluminosilicate such as mullite at 925°C and 1100°C forms such as mullite (Bryers, 1995).

(a)

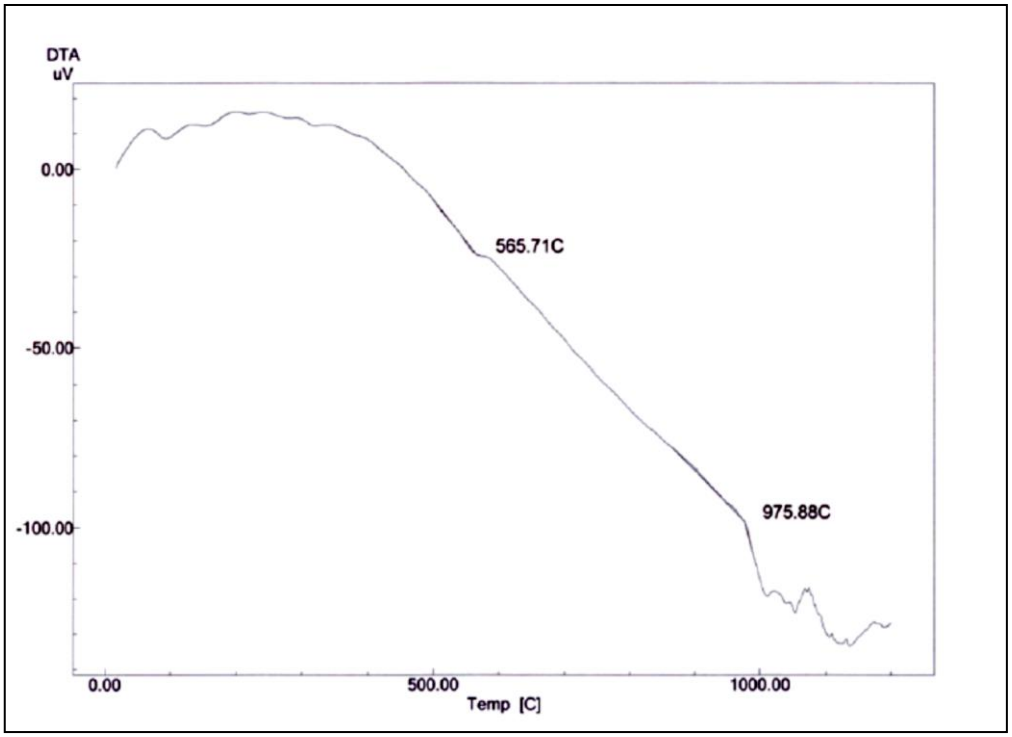

(b)

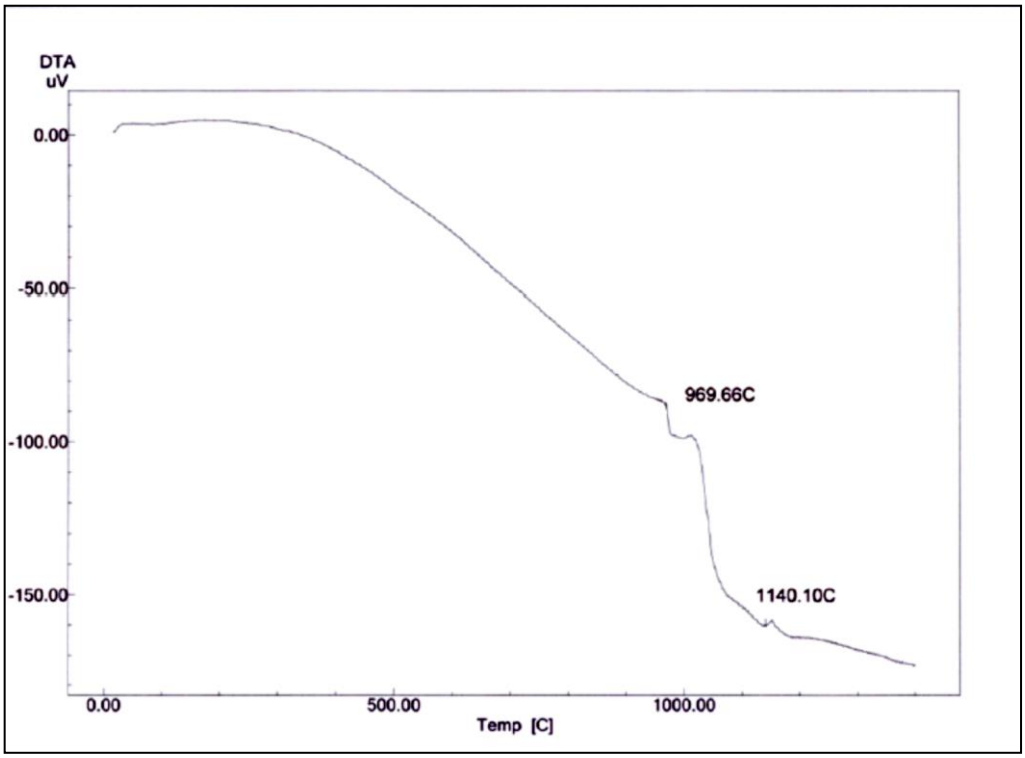

Figure 4.31: Thermal behaviour of the fireside deposit on Station A tubing samples.

(a)

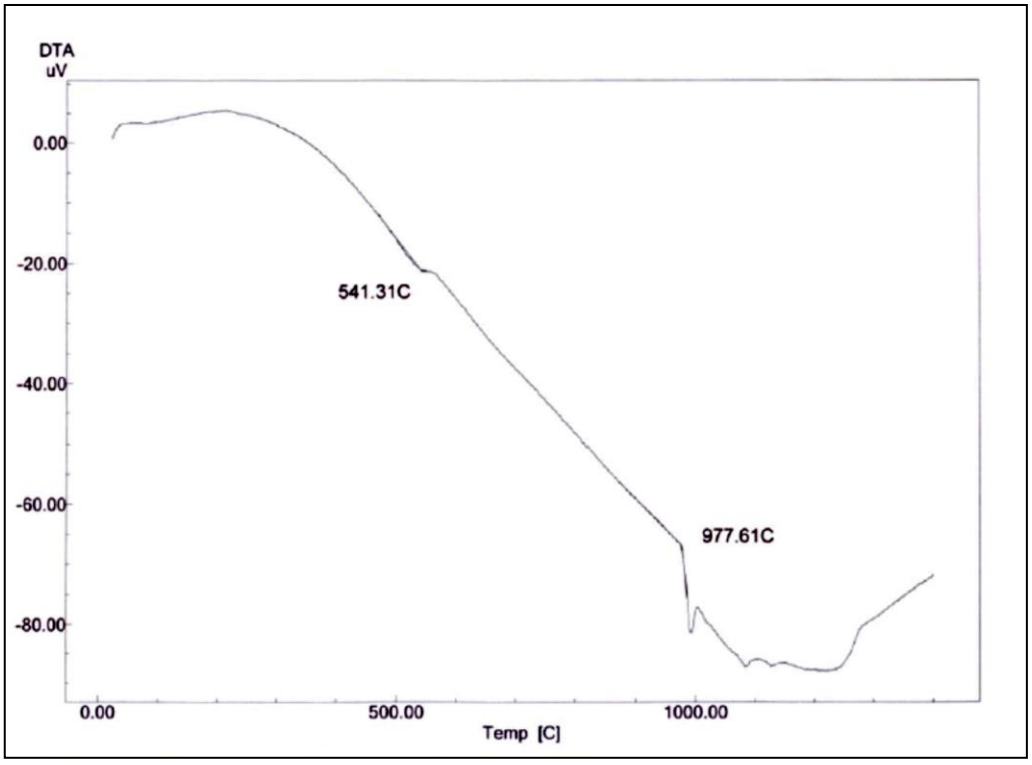

(b)

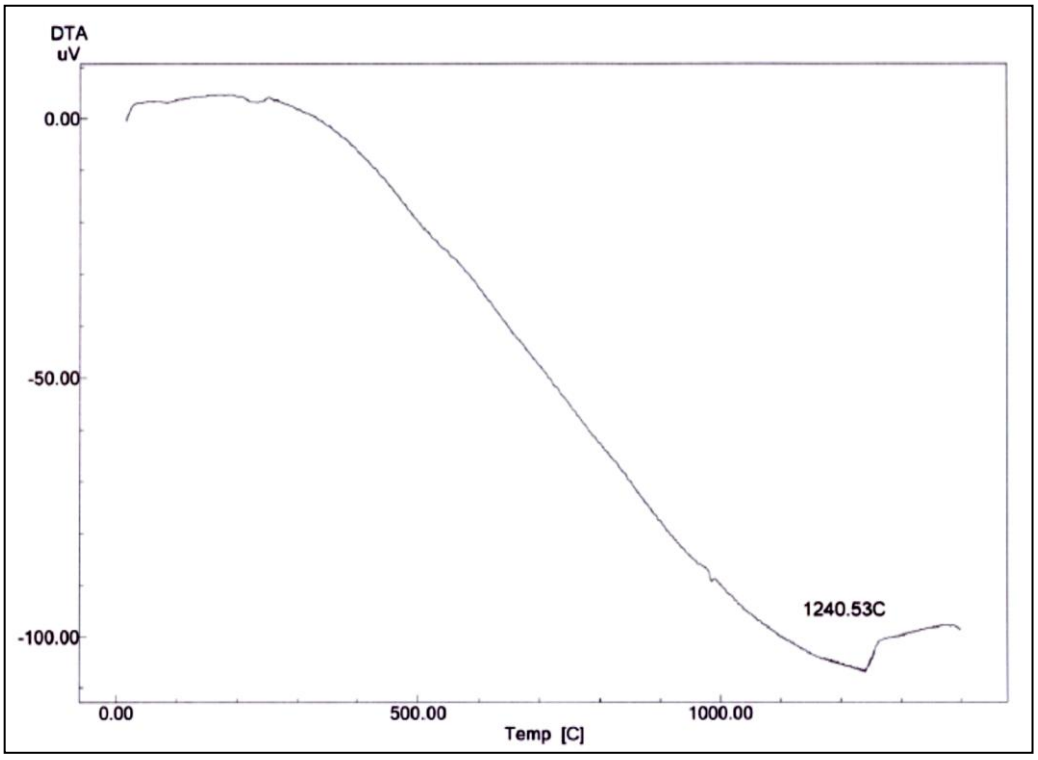

Figure 4.32: Thermal behaviour of the fireside deposit on Station B tubing samples.

4.3 IN-SITU GAS ANALYSIS

In-situ gas analysis performed at Unit 1 of Eskom Station A verified that the furnace is operating under reducing conditions. The oxygen content in the flue gas was found to be lower than the Pulverised Fuel Firing Regulations limits of ≥ 2%. High levels of CO were measured at the furnace wall (up to 38000 ppm) and furnace exit (≥ 3500 ppm). In all the three tests performed O_2 and CO measurements were taken at economiser outlet and furnace exit.

Test 1 was performed at a load of 576.0 MW and the results obtained showed that the CO measurements at gun blower 12 and furnace exit levels were significantly higher than the recommended, which is maximum 2000 ppm, as shown in Figure 4.33. This is according to Benedetto Riso from RECOM Services GmbH, who provides Computational Fluid Dynamic combustion modelling of industrial furnaces and boilers (Van Wyk, 2010).

Test 2 was carried out at 584 MW at gun blower 12 and furnace exit levels. Figure 4.34 shows high CO levels, greater than 2000 ppm, measured at gun blower 2. Distribution of O_2 at gun blower 2, Figure 4.34, and economizer outlet, Figure 4.35, varies significantly from 3.5% to 0.8%, which is a clear indication of substoichiometric conditions in the furnace.

Test 3 was conducted at 567 MW at the same location as Test 2. Again varying O_2 levels were seen at gun blower 2, Figure 4.36, and economizer outlet (left hand side), Figure 4.37. The CO measurements at gun blower 12 were still higher than 2000 ppm. The substoichimetric conditions and high CO levels are some of the parameters that drive sulphidation corrosion.

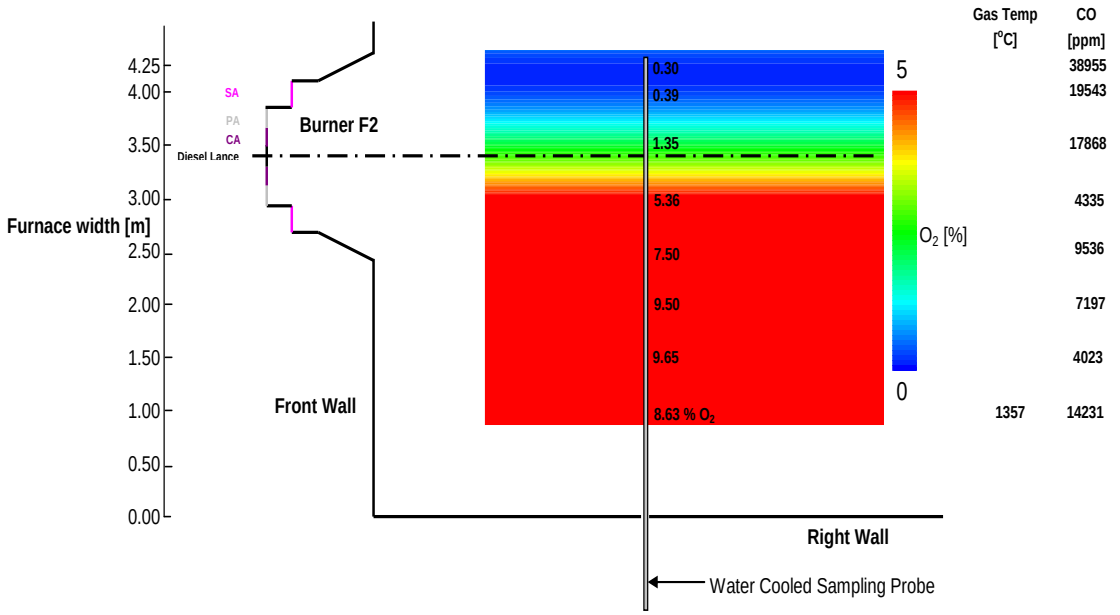

Figure 4.33: CO and O_2 distribution at Gun Blower 12, Test 1 conducted at 576 MW/hr.

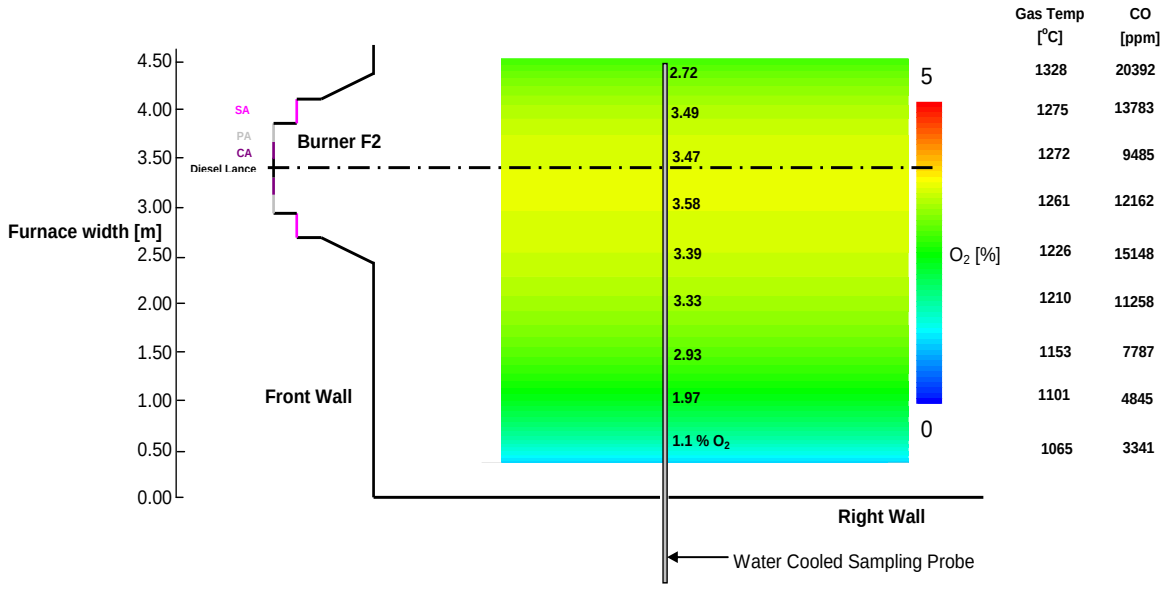

Figure 4.34: CO and O_2 distribution at Gun Blower 12, Test 2 performed at 584 MW/hr.

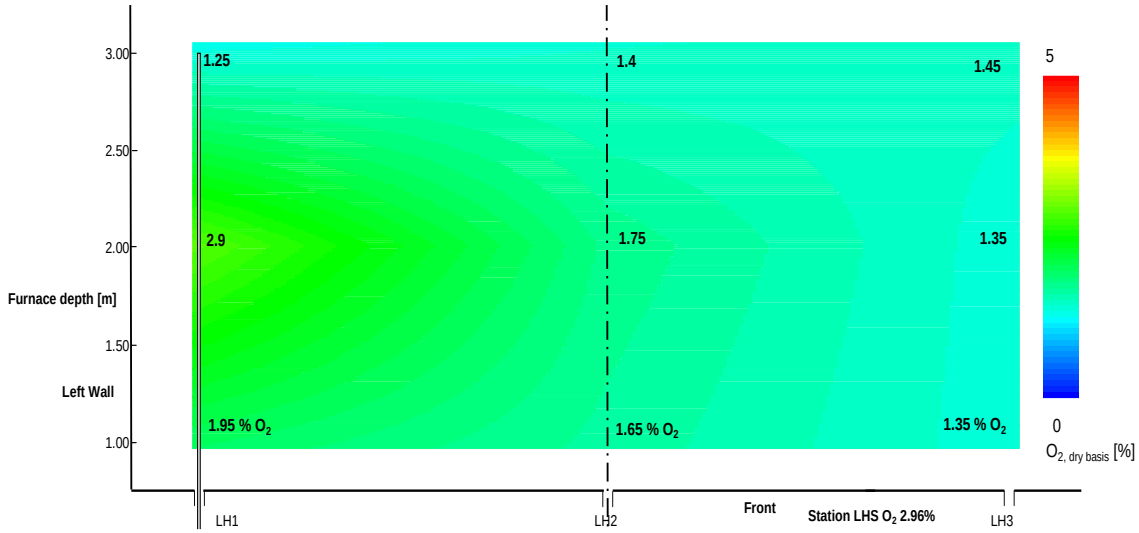

(a)

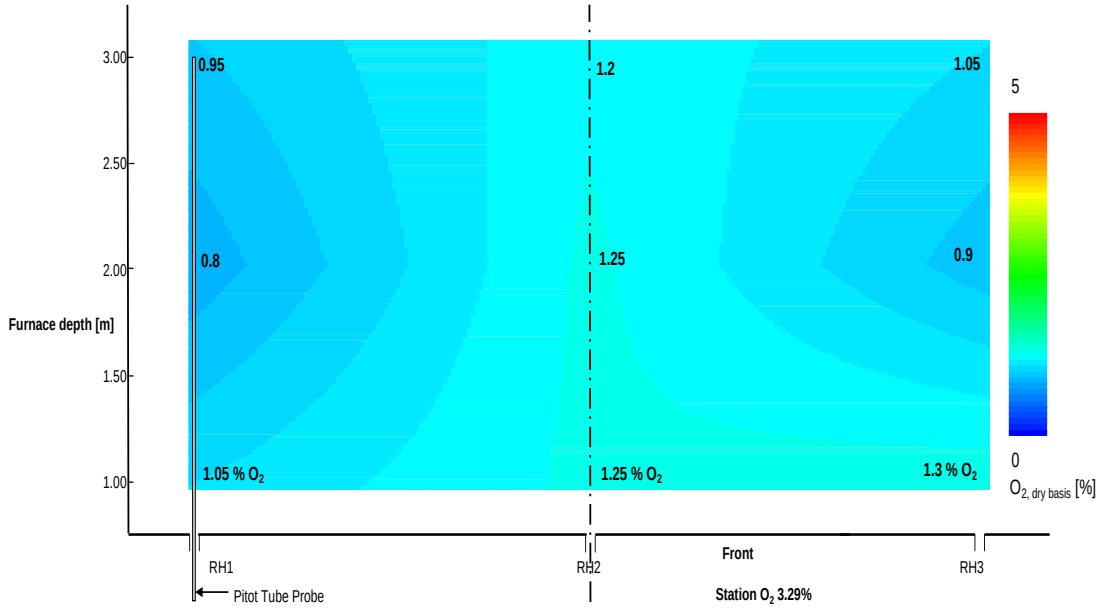

(b)

Figure 4.35: O_2 distribution at Economiser Outlet (a) left hand side duct and (b) right hand side duct, Test 2.

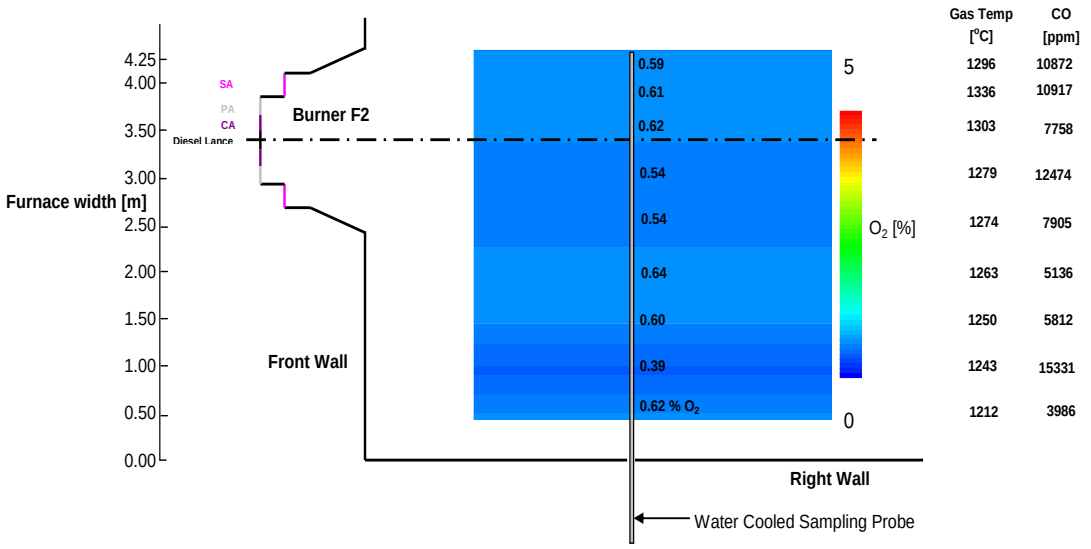

Figure 4.36: CO and O_2 distribution at Gun Blower 12, Test 3 performed at 567 MW/hr.

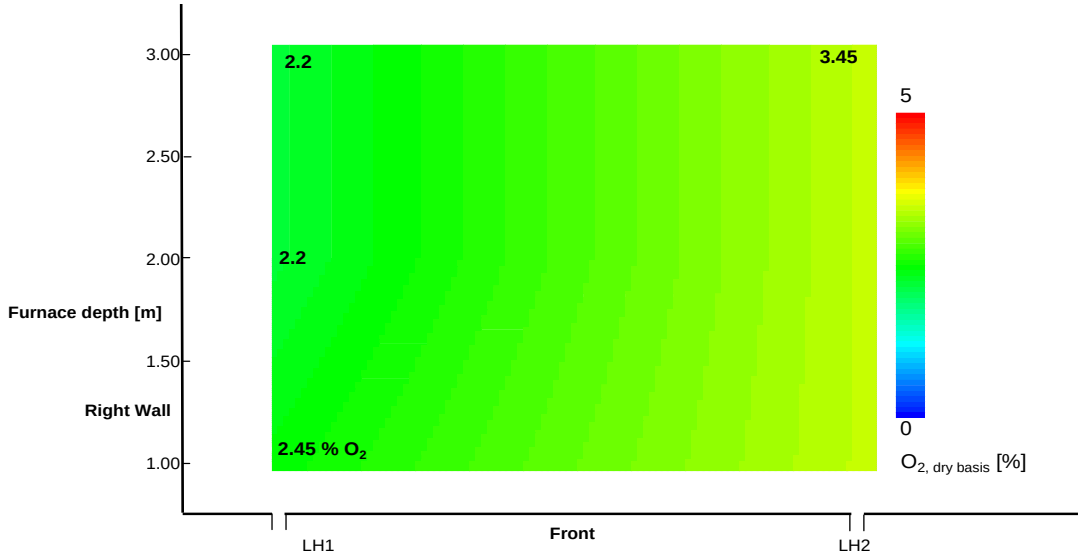

(a)

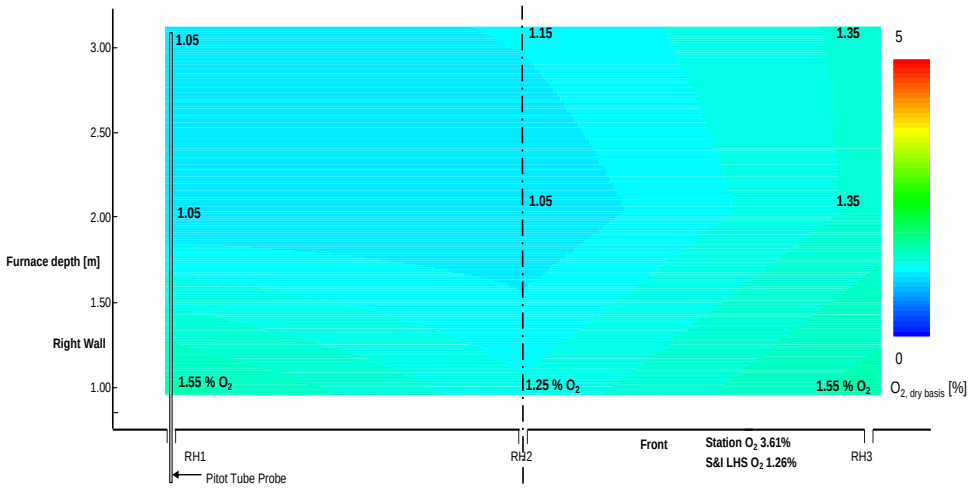

(b)

Figure 4.37: O_2 Distribution at Economiser outlet (a) left hand side duct and (b) right hand side duct, Test 3.

5. DISCUSSION

5.1 INTRODUCTION

In this chapter, the properties of the boiler tubes alloys used for the investigation into the mechanism of fireside corrosion are presented, the results of the analyses and characterisation of the fireside deposit will be discussed, as well as the combustion gas test results of Unit 1 of Station A.

5.2 STATION A - TUBING CONDITION

Station A tubing samples consisted of both ruptured and non-ruptured tubes. The fireside was completely covered with reddish brown and black coloured, hard and thick deposits with loosely bonded ash on top. The installed wall thickness was 5.6 mm and the minimum measured wall thickness was 0.7 mm and 0.1 mm on the non-ruptured and ruptured tubes respectively. The wall thinning was essentially all from the fireside, but focussed at the 10 o'clock and 2 o'clock positions.

The alloy was verified as 15Mo3. The fire and cold side for the non-ruptured tubes consisted of well-spheroidized carbides, still grouped in the original pearlitic pattern, in a ferrite matrix. The spheroidized microstructure is typical of service exposed tubing operating at moderately elevated temperatures. The hardness of 135-158 HV and 139-146 HV was measured on fire and cold sides of the non-ruptured tube respectively, which is well within the specification of BS EN 10216-2 (2013), given as 131-186 HV for 16Mo3 alloy, an equivalence of 15Mo3. The similar appearance in the fire and cold sides of the tubing indicates that the flame-exposed side of the tubing was not significantly hotter than the casing side. This indicates that the non-ruptured tube had not been overheated during service.

The exception was seen on the ruptured tube from Unit 2 which had a deformed microstructure at the rupture and away from rupture the microstructure consisted primarily of large well defined pearlite colonies in ferrite. A measured hardness of 164 HV confirmed the strain hardening at this

location. It was obvious from both of these observations that this tube had been overheated, but below its transformation temperature, perhaps as a result of an earlier failure in the same tube circuit that resulted in loss of flow.

5.3 STATION A - CHARACTERISATION OF FIRESIDE DEPOSIT

EDS mapping results presented in section 4.2.1 for Station A samples showed fireside deposit with three distinct layers. The inner layer (attached to the metal surface) was composed of high concentration of iron and oxygen and low sulphur, whereas the intermediate and outer layers were rich in iron and sulphur, but low in oxygen. The outer layer was also observed of low levels of Al, Si, and Ca, elements associated with fly ash.

The mineralogical characteristics of the fireside deposit in different layers were determined by QEMSCAN and micrographs are shown in section 4.2.2. A three layered fireside deposit was observed, with the inner and intermediate layers made up of a uniform iron sulphide bands. In addition to the iron-containing sulphide the intermediate layer comprised of magnetite and some Na/Mg-alumina-silicates. In the samples of the outer layer, some iron-containing sulphide and magnetite can also be found, but the sodium-containing aluminosilicates, calcite and quartz are identified. The exception is seen on Unit 3 samples where the inner layer consisted of only magnetite, the intermediate and outer layers had the same mineralogical distribution as the other Units. The iron sulphide was measured in average volume percentages of 47% to 80%, iron oxide (hematite and magnetite) was in levels of 4% to 49%, whereas fly ash compounds ranged from 3% to 14% through the thickness of the fireside deposit. The most heavily corroded tube exhibited the thickest inner iron sulphide scale layer.

The possible series of mechanisms presented above is also reported by Yu et al. (2017), who through several failure investigations found that the furnace wall fireside corrosion products comprising ostly of iron-containing sulphide and magnetite and as a result classified the corrosion in this power plant as the sulphide type corrosion. Yu et al. (2017) further states that the main reason for high temperature corrosion from the sulphide type is due to the large amount of H_2S, detached sulphur, and the unstable FeS that would be formed in the oxygen-deficient ambience

(i.e. reducing conditions) when a high sulphur coal is burned. French (1982) also suggested that the corrosion attack on the furnace wall tubes is associated with sulphides and requires strongly reducing conditions at the tube surface.

The thermal analysis of Station A tubing showed peaks generally at temperatures ranging from 950 to 1250°C. The exception was seen on one tube where lower temperature activity was indicated at 565°C. The thermal behaviour of minerals commonly found in coal is well explained in Figure 5.1 by the survey conducted by Watt, Jackson and Walchuk as cited by Bryers (1995). They determined that kaolinite transforms into metakaolinite at temperatures around 500°C, which further transforms into other forms of aluminosilicate at around 925°C and 1100°C. Mitchell and Gluskoter, cited by Bryers (1995), had similar observations from examining minerals released from coal by means of low-temperature ashing (LTA) (i.e., oxidizing carbon at temperatures of 150°C under an oxygen plasma without disturbing the mineral structure) by slow heating the released minerals on a hot stage quenching and analysing. The analyses were performed at temperature, and after quenching the results were summarized as shown in Figure 5.2. The lower temperature transformations involve pyrite's (FeS_2) oxidation into FeO and FeS which occurs at 475°C. FeO transforms further into Fe_2O_3 at 525°C. All these minerals were detected in the fireside deposit of Station A by QEMSCAN and the thermal indications observed from DTA concur with thermal behaviour described by Bryers, 1995. Therefore, the low temperature peak, at 565°C, is likely an indication of pyrite's oxidation into FeS and Fe_2O_3. Whereas, the thermal peaks measured at higher than 900°C may be representation of metakaolinite transformation into other aluminosilicate forms such as mullite.

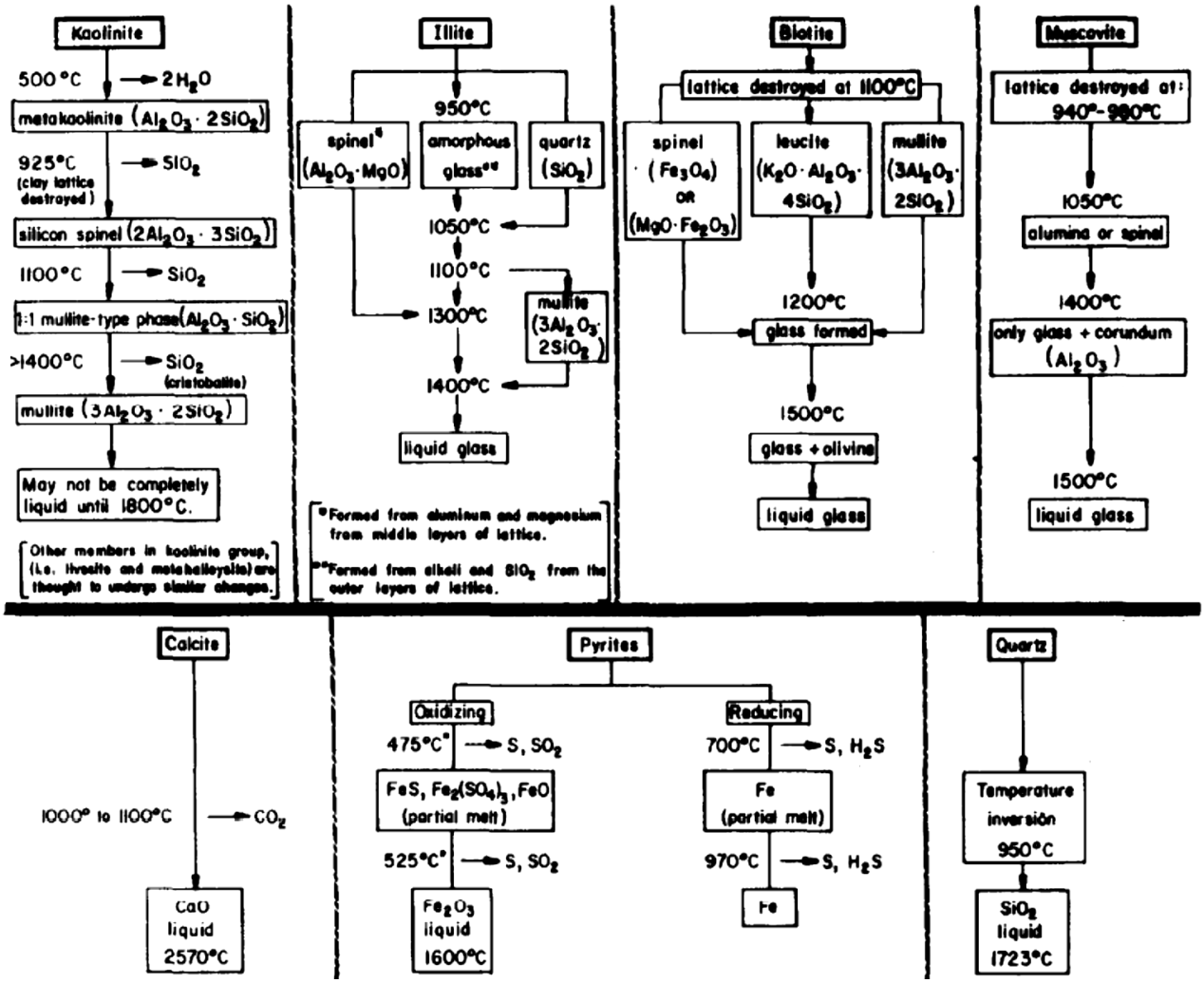

Figure 5.1: Phase transformation of minerals commonly found in coal (Bryers, 1995).

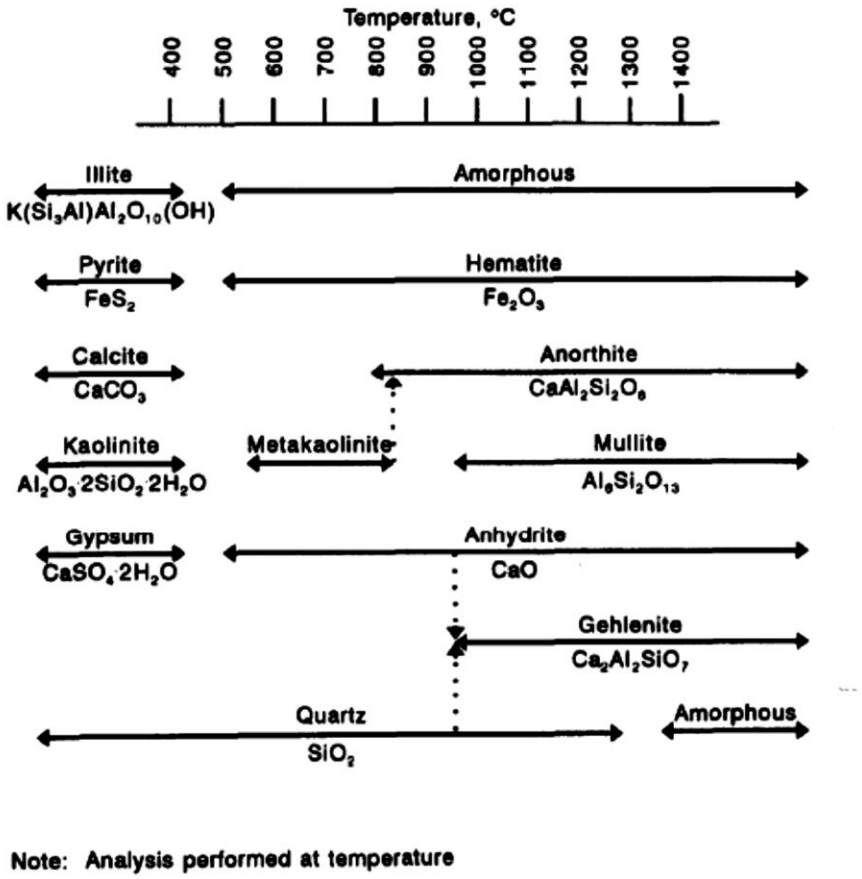

Figure 5.2: Summary of mineral transformations due to heating low-temperature ashed coal by Gluskoter and Mitchell as cited by Bryers (1995).

The presence of sulphide phases, FeS and FeS_2, coexisting with iron oxide is indicative of reducing conditions in the furnace or on the tube surface. Reducing conditions are formed when there is limited oxygen (<2%) in the furnace (Dooley and McNaughton, 2007). Under uniformly, constant oxidizing conditions, protective oxides form and fireside corrosion is not a problem. However, the development of reducing conditions from a variety of causes, can lead to deposition, primarily of iron sulphide and alkali sulphates. There was no detection of sodium and potassium which are the primary elements of alkali sulphates. Therefore, all the features of the fireside deposit indicate sulphidation as the mechanism for the fireside corrosion on the furnace walls of Station A.

In-situ gas analysis performed at Unit 1 of Station A verified that the furnace was operating under reducing conditions. The O_2 content in the flue gas was found to be outside the Pulverised Fuel Firing Regulations limits (< 2%). Very high levels of CO were measured at the furnace wall (up to 38000 ppm) and furnace exit (≥ 3500 ppm). In all the three tests performed O_2 and CO measurements were taken at economiser outlet and furnace exit. Dooley and McNaughton (2007) report that CO levels close to water wall tubes needs to be kept below 2% to minimize CO corrosion on the tubes. Reid (1984), found CO concentrations of 0.9 - 4.9% in areas of corrosion. No corrosion was observed in areas where carbon monoxide was absent or present in quantities of less than 0.2%.

5.4 STATION B - TUBING CONDITION

Station B showed different features to Stations A. Although most of the tubes revealed general wall thinning on the fireside, it was mostly uniform and not localized on typical locations encompassing 120°C angle. Unit 3 on the other hand showed uneven wall thinning on both fireside and non-fireside, which suggests that the tubes maybe experiencing other forms of attack. Different fireside deposits were also observed on Station B tubing. Units 1 and 3 had hard and thin sintered brown deposits, whereas Unit 8 and 10 were observed of loosely bonded grey ash deposit. The minimum wall thickness was measured as 1.76 mm and 5.54 mm on the fire and cold sides respectively. Based on 6 mm installed wall thickness, the highest wall thinning was measured at 70.6%. Deposit was measured at a maximum of 0.6 mm.

The material of the tubes was confirmed as SA106. Similarly to station A, the fire and cold sides consisted of well-spheroidized carbides, still grouped in the original pearlitic pattern, in a ferrite matrix. The average hardness of 131-143 HV and 126-150 HV was measured on fire and cold sides of the tubes respectively, which correlates with specification of ASTM A106, 2018, given as 147 HV maximum for SA106 alloy. One point on the coldside was measured at 150 HV which slightly higher than the standard specification by 3 HV; this is likely due to an error in the measurement.

5.5 STATION B - CHARACTERISATION OF FIRESIDE DEPOSIT

Similarly to Station A, three layered fireside deposits were observed under light microscope and SEM. The EDS mapping, presented in section 4.2.1, revealed high levels of iron and oxygen with low sulphur in the inner layer. The sulphur content was seen to increase in the intermediate layer while oxygen decreased. The outer layer showed a similar elemental distribution as the inner layer, rich in iron and oxygen but low in sulphur. In addition, the outer layer consisted of Al, Si, and Ca. X-ray diffraction identified iron-oxide in predominant form of magnetite and in low levels of hematite. Iron-sulphur rich phases detected include FeS, FeS_2 and PbS. Fly ash particles were detected in a form of mullite, quartz and jarosite. In Unit 1 tubing, FeS was measured in small quantities ranging from 3.7-5.6 weight %, whereas for Unit 3 high levels of FeS were measured in the range of 40-50 weight %. Similarly to Station A, the presence of sulphide phases, FeS and FeS_2 and no detection of sodium and potassium which are the primary elements of alkali sulphates, suggests that the corrosion on the fireside of boiler tubes is of sulphide type, which is highly associated with reducing conditions in the furnace and/or on the tube surface. The high concentration of FeS in Unit 3 may be indicative of prolonged reducing conditions in the furnace and/or on the tube.

DTA showed thermal activity at 541°C, 977°C and 1240°C. Bryers (1995) and Reid et al. (1945) identified the presence of alkali-iron tri-suphates and pyrosulphates on superheaters and furnace walls respectively, as responsible for tube wall thinning. Srivastava et al. (1997) explained that molten pyrosulphates exist at lower temperatures and perform corrosion reaction in the range between 400-482°C. Both the pyrosulphates ($Na_2S_2O_7$ and $K_2S_2O_7$) are likely to exist as deposits on heat-exchangers in the presence of sufficient SO_3. DTA measured the lowest thermal activity measured at 541°C, which is higher than corrosion reaction range of molten pyrosulphate. This, in addition to the absence of sodium and potassium in the fireside deposit, suggest that the thermal activities observed from DTA are not associated with alkali sulphates. Instead, similarly to Station A, it appears that the low temperature peak, at 541°C, is indicative of pyrite's oxidation into FeS and Fe_2O_3. Whereas, the thermal peaks measured at temperatures higher than 900°C may be representation of metakaolinite transformation into other aluminosilicate forms such as mullite.

The presence of sulphide phases, FeS and FeS_2, coexisting with iron oxide is indicative of substoichiometric conditions in the furnace or on the tube surface, and the absence of alkali sulphates (Na and K sulphate salts) suggests that sulphidation is also the mechanism for the fireside corrosion on the furnace walls of station B.

5.6 STATION C - TUBING CONDITION

The fireside was completely covered with grey layer of sintered deposits. Wall thinning was observed at 10 o'clock and 2 o'clock positions. Wall thickness measured on the fireside ranged from 2.92 mm to 3.4 mm. Based on 7.5 mm installed wall thickness, the wall thinning measured was in the ranges of 45.2-65.3%. Deposit was measured of thicknesses up to 0.57 mm.

The alloy of the tubes was verified as SA105. The fire and cold sides consisted of well-spheroidized carbides, still grouped in the original pearlitic pattern, in a ferrite matrix. The spheroidized microstructure is typical of service exposed tubing operating at moderately elevated temperatures. The hardness of 142-147 HV and 140-147 HV was measured on fire and cold sides respectively, which conforms to the standard specification of ASTM A105 (2018), given as 197 HV maximum for SA105 alloy. The similar appearance in the fire and cold sides of the tubing indicates that the flame-exposed side of the tubing was not significantly hotter than the casing side.

5.7 STATION C - CHARACTERISATION OF FIRESIDE DEPOSIT

Fireside deposit on samples from Station C, with three distinct layers, presented a similar morphology to that seen on Station A and B samples. The EDS profiles revealed high proportions of iron and oxygen in the inner layer, but with very low levels of sulphur. The intermediate and outer layers was detected of high levels of iron and sulphur and low oxygen. Fly ash elements, Al, Si, and Ca, were also detected in the outer layer but at significantly lower proportions.

QEMSCAN analysis also showed a three layered fireside deposit consisting of high concentration of iron sulphide in the inner and intermediate layers. Iron oxide was located on the intermediate and outer layers, with the presence of silicates and aluminosilicates on the outer layer. The average volume percentage of iron sulphide was between 67% to 69%, while iron oxide (combination of

magnetite and hematite) levels were in the range of 21% to 30%. Fly ash particles were found to range from 0.3% to 9%. Station C exhibits similar mechanism of corrosion as that suggested for Station A and B, which is sulphide type corrosion, driven by substoichiometric conditions in the furnace or on the tube surface.

5.8 PROPOSED MECHANISM AND CAUSES OF FIRESIDE CORROSION

The systematic investigation and characterisation of the fireside deposit of the furnace wall boiler tubes from the three fossil fired power stations A, B and C of Eskom generated unambiguous results that exhibit the same mechanism of fireside corrosion. The results of SEM-EDS and QEMSCAN analyses revealed that the fireside scale was composed of three distinct layers: (i) Fe-oxide and Fe-sulphide inner layer, (ii) Fe-sulphide rich intermediate layer and (iii) the outer layer consisting of low Fe-sulphide, high Fe-oxide and low to high levels of Ca/Mg-aluminosilicates. The iron oxide was mainly in the form of Fe_3O_4 and Fe_2O_3 and the iron sulphide was predominantly identified as pyrrhotite (FeS) with low levels of galena (PbS) and pyrite (FeS_2). Fly ash particles consisted mostly of silica (SiO_2) and alumina-silicate associated with iron sulphide, calcium and magnesium. The thermal phase transformation of alumina-silicate, i.e. metakaolinite into mullite, were detected consistently at temperatures higher than 900°C, specifically in the ranges of 950 - 1000°C and 1000 - 1250°C for stations A and B respectively, which concurs with thermal behaviour described by Bryers (1995). On isolated samples, lower temperature peaks were measured between 500 and 600°C, indicating pyrite (FeS_2) transformation into FeS, $Fe_2(SO_4)_2$ and FeO (Borio and Levasseur, 1986). The coexistence of pyrrhotite in high levels with iron oxide and the presence of pyrite in the fireside deposit is indicative of the reducing conditions occurring in the furnace as well as on the surface of the boiler tubes.

As previously mentioned, the analysis of the ash deposits formed on tubes from stations A, B, and C is on contrary to the theory presented by Reid et al. (1945) and Srivastava et al. (1997), where they identified the pyrosulphates, molten at temperatures exceeding 398°C for sodium pyrosulphate ($Na_2S_2O_7$) and 454°C for potassium pyrosulfate ($K_2S_2O_7$), being responsible for fireside corrosion boiler tubes. The characterization and analytical analyses of fireside deposits from Stations A, B and C, did not identify or detect sodium and potassium, which are primary

elements for alkali sulphate phases. Instead, iron sulphide rich phase was identified consistently in all the analysed furnace wall tubing samples. This type of fireside corrosion mechanism was also identified by French (1982), whom through several failure investigations of furnace wall tubes over a period of a decade, consistently detected sulphur, oxygen, iron, silicon and chromium in the ash deposits. No sodium, potassium or chlorine was observed in the study conducted by French (1982). French suggests that the corrosion attack on the furnace wall tubes is associated with sulphides and requires strongly reducing conditions at the tube surface. He further states that carbon is required so the sulphites that form are stable. Carbon can enter the ash deposit either as unburned coal or the deposition from carbon monoxide. French proposed that the corrosion on furnace wall tubes occurs in several stages as outlined in section 2.4.1 from equation 1 to 9.

Hong and Yong (2002) state that high temperature corrosion of the water-cooled wall caused by sulphur in a coal-fired power plant can be divided into two types, namely sulphide type and sulphate type. Through his investigation of fireside corrosion at water-cooled wall from a coal-fired power plant in China, Yu et al. (2017), found that the corrosion products were composed mostly of iron-containing sulphide and magnetite and as a result classified the corrosion in this power plant as the sulphide corrosion. He further states that the main reason for high temperature corrosion from the sulphide type is due to the large amount of H_2S, detached sulphur, and the unstable FeS that would be formed in the oxygen-deficient ambience when a high sulphur coal is burned.

Literature (Yu et al., 2017, Dooley and McNaughton, 2007, Bryers, 1995) states that reducing conditions have been known to also result in reducing flue gas containing H_2S, which causes gas phase reactions. However, corrosion caused solely by the presence of reducing flue gas containing H_2S is expected to be low for subcritical boilers and the level of H_2S in the flue gas is correlated with sulphur content of the coal (Yu et al., 2017). The coal combusted at the three power stations had the average sulphur content of less than 1.5% in the coal, which is regarded low, refer to Appendix H. Also, the degree of wall thinning experienced by all three power stations is high, especially on stations A and C, resulting in failures at some Units. It is clear from the two observations, significant wall thinning and low sulphur percentage in the coal, that H_2S levels in the flue gas could not have been a dominant factor in the fireside corrosion. Therefore, gas phase

reactions are not the sole cause of fireside corrosion but may have contributed to formation of sulphide rich deposits, which leaves sulphidation as the probable mechanism of fireside corrosion.

Reducing conditions are formed when there is limited excess oxygen (<2%) in the furnace, (Yu et al., 2017). Bakker (1998) states that low excess O_2 favours the gasification process over combustion process. Gasification results in the formation of H_2S and limits oxidation of CO and combustion of pyrite (FeS_2). This occurs through the reaction of sulphur in the coal (i.e. FeS_2, S_{org}) and some H_2 present in the flue gas which can be partially converted into H_2S instead of SO_2 (Hatt, 1990, Reid et al., 1945), through the following reactions:

$$FeS_2 + H_2 \rightarrow FeS + H_2S \qquad \text{Equation 23}$$

$$S_{(org)} + H_2 \rightarrow H_2S \qquad \text{Equation 24}$$

Reid et al. (1945) observed that under highly reducing conditions the pyrite is not completely burnt and the unburned pyrite is transported to the tube surface through flame impingement and may react directly with the iron in the tube walls resulting in sulphidation as shown by equation (25).

$$Fe + FeS_2 \rightarrow 2FeS \qquad \text{Equation 25}$$

The high amounts of CO and H_2S favour a shift in the chemical equilibria for the sulphur species in the flue gas towards higher sulphur potentials and thus allow sulphidation of the metal to take place as well as oxidation (Bakker, 1998). When H_2S is present in the flue gas, it will preferentially react with iron in the furnace wall tubes, through molecular diffusion, to form pyrrhotite (FeS) as follows:

$$Fe + H_2S \rightarrow FeS + H_2 \qquad \text{Equation 26}$$

By solid-state diffusion, already formed Fe_3O_4 may also be transformed into FeS,

$$Fe_3O_4 + 3H_2S \rightarrow 3FeS + 3H_2O + \tfrac{1}{2}O_2 \qquad \text{Equation 27}$$

The substoichiometric conditions in the furnace were confirmed by the morphology and characteristics of the fireside deposit found on tubing from Station A, B and C, with the inner layer consisting of Fe_3O_4, Fe_2O_3, and FeS, the intermediate layer being rich in FeS and the outer layer rich of iron oxide, fly ash and unburnt coal.

Davis et al. (2001) found that, the typical conditions under which most of furnace wall tubing in pulverized fuel-fired plants should operate, with negligible corrosion rates and tube life exceeding the expected life span are achievable if the furnace environment is predominantly oxidizing environments. These conditions enable production of dense, adherent and protective mixed oxide/sulphide corrosion deposits and corrosion rates are parabolic as shown in equation 28 and are dependent only upon metal temperature, with no effect of coal composition or heat flux.

$$K_{Po} = A \times e^{-(Qo/RT)} \qquad \text{Equation 28}$$

Where K_{Po} = Parabolic Rate Constant ($cm^2.sec^{-1}$) under oxidation,

A = Constant,

Qo = Activation Energy for Oxidation ($J.mole^{-1}$),

R = Gas Constant (8.3143 $J/K^{-1}.mole^{-1}$),

T = Temperature °K.

When the furnace operated under reducing (O_2 < 0.5%, CO > 2%) in the absence of chlorine (Cl < 0.05%), the corrosion mechanism shifted progressively from oxidation towards sulphidation as the CO content of the flue gas increased and the O_2 content declined. The corrosion mechanism produced an adherent deposit and parabolic kinetics still pertained, albeit at higher metal loss rates than those obtained under oxidizing conditions. There was no measurable effect of heat flux on the corrosion rates, but increasing the CO content of the flue gas did increase the corrosion rates via the formation of progressively more sulphide within the deposit (equation 29).

$$K_{Pr} = B \times (\%CO)^n \times e^{-(Qr/RT)} \qquad \text{Equation 29}$$

Where K_{Pr} = Parabolic Rate Constant ($cm^2.sec^{-1}$) under reducing conditions,

B = Constant,

Qr = Activation Energy for Mixed Oxidation Sulphidation ($J.mole^{-1}$),

%CO = percentage of CO in the local combustion environment.

Gas analysis of Unit 1 of station A correlate with the findings by Davis et al. (2001). High levels of CO were measured at the furnace wall (up to 38000 ppm) and furnace exit (≥ 3500 ppm) (Van Wyk, 2010), boiler areas with high wall thinning due to fireside corrosion. High CO concentrations are indicative of limited combustion caused by limited excess O_2. These conditions promote formation of FeS rich deposit as seen on Unit 1 of Station A. Sulphide deposits allow higher rates of transport (diffusion) of iron cations than oxides, the strength and adherence of the deposit decrease with increasing FeS content, while its growth rate and permeability increase significantly. These deposits are also brittle and poorly adherent, so they readily crack and spall and are easily removed by soot blowing or thermal cycling. The result is increased metal wastage (i.e. wall thinning), which becomes the dominant factor in tube life. The morphology and characteristics of the fireside deposit on tubes from the three power stations are indicative of a sulphidation mechanism of fireside corrosion caused by reducing conditions in the furnace.

Mitigation of furnace wall fireside corrosion is achievable through effective control of combustion process in order to prevent formation of reducing conditions. Effective combustion process can be achieved through the following (Sherlock et al., 1997, Sherlock et al., 1999, Bakker, 1998):

- Controlling the amount of free oxygen in the flue gas within acceptable limits (> 2%). The corrosion rate decreases with increasing oxygen content.
- Minimising the amount of CO in the flue gas (< 2000 ppm). The corrosion rate increases strongly with increasing CO content, indicating that FeS becomes stable in highly reducing environments.
- Avoiding flame impingement and high tube temperature. Like most chemical reactions, the corrosion rate is an exponential function of temperature.

Combustion modelling is a tool mostly used to introduce changes in the combustion process. Combustion Fluid Dynamic (CFD) modelling simulates all known reactions occurring during the combustion process in a boiler and is also able to track trajectories of ash and coal particles. Thus,

it can predict flue gas temperatures and compositions anywhere in the boiler as well as deposit formation and the composition thereof. These predictions can be compared with known areas of high corrosion rates to determine if there are any correlations. Bakker (2001), made a model for a supercritical, tangentially fired boiler, suffering from corrosion primarily on the front and rear wall. The combustion model showed that the area of high corrosion did not correlate very well with areas where the flue-gas near the wall was reducing and contained high levels of H_2S. However, the corrosive areas correlated quite well with the areas where deposits of FeS and unburned carbon are likely to occur.

In addition to combustion modelling, there are other various options available for the control and mitigation of fireside corrosion of furnace wall tubes, these include (Bakker, 2001):

- Mills – Improving the operation of PF mills could reduce the likelihood of unburned carbon being found in the ash deposits.
- Inspection and adjustment of burners – This could improve combustion conditions and prevent direct flame impingement.
- Air blanketing – This mitigation measure is used mostly in low NOx burners. Air blanketing is used to provide an oxygen rich atmosphere along the furnace walls and has been found to be effective.
- Coatings and weld overlays – Thermal spray coatings and weld overlays can be used to provide a layer of corrosion resistant material on the tube surface. Good surface preparation prior to coating is crucial if this approach is to be effective. These solutions use alloys with high chrome (25-30% or higher) or chrome/nickel (45Cr-50Ni) content. The life expectancy of metal spraying is 3 to 5 years depending on the corrosivity of the environment, thermal cycles (which lead to spalling) and the quality of the application. Weld overlays, using Cr-Ni alloys can add between 7-15 years of life depending on the alloy used.

6. CONCLUSIONS

While the mechanism of high temperature corrosion in superheater and reheater by liquid phases within the coal ash is reasonably well understood, no comparable understanding of furnace wall corrosion is available. Most of the literature looking at fireside corrosion on furnace wall corrosion is centred around alkali sulphate reactions with very limited focus on the iron sulphide deposit and its role in fireside corrosion. This study was aimed at gaining a better understanding of the mechanism(s) of fireside corrosion is on furnace wall tubes from fossil fuel fired boilers of Eskom. A series of fireside corrosion product analyses were conducted on boiler tube samples from conventional subcritical coal fired boilers. The knowledge and understanding acquired from this study will not only be beneficial to the conventional subcritical coal fired boilers but to subcritical boilers operated with low NOx combustion as well as supercritical boilers.

To comply with air pollution control laws, coal fired power generation industries have to apply certain technologies to reduce the emissions of the NOx and SOx. Low excess air combustion and two-stage combustion processes are commonly applied as means of realizing low-NOx emissions. These combustion methods can reduce NOx emission from a boiler, however, a strong reducing atmosphere is formed in the region between burners and airports in the case of two-stage combustion. This atmosphere promotes the formation of hydrogen sulphide (H_2S), which causes sulphidation corrosion at the boiler wall (Hard and Smith, 2010, Dooley and McNaughton, 2007).

To meet the high demand of electricity, superctitical boilers are more frequently introduced. At higher operating temperatures of these boilers the tubes are at a higher risk of suffering high temperature corrosion, of which fireside corrosion forms part.

This study aimed to determine the (i) actual mechanism of fireside corrosion taking place on furnace wall tubes from power stations A, B and C, (ii) the role of the combustion process in promoting the existence of this fireside corrosion mechanism and (iii) the control measures commercially available and applicable for power generation utility.

The conclusions drawn from all the tests and analyses performed are as follows:

1. The mechanism of fireside corrosion taking place on the furnace walls of fossil fired boilers from stations A, B and C is sulphidation due to FeS deposition. The main contributors to FeS deposition are the reducing conditions in the furnace caused by high CO levels (> 2000 ppm) and low excess O_2 (< 2%) in the flue gas and on the tube surface caused by unburned coal.
2. Sulphide scales that form allow higher rates of transport of iron cations than oxides, they are brittle and poorly adherent so they readily crack and spall, the result is increased tube wall thinning which becomes the dominant factor in tube life. Corrosion rates increase rapidly with increasing FeS scale content up to 20%. At higher FeS levels corrosion rates will continue to increase, but at a lower rate.
3. Mitigation of sulphidation corrosion can be applied through more effective combustion processes which can be achieved by controlling the amount of free oxygen in the flue gas within acceptable limits, $\geq 2\%$, minimising the amount of CO in the flue gas to below 2000 ppm, avoiding flame impingement on the tubes and ensuring the use of the correct coal particle size to reduce the amount of unburned carbon in the ash deposits. In addition, coatings and weld overlays can be considered as material solutions for reducing the corrosion rate on the tubes fireside surface.
4. The degree and extent of fireside corrosion is likely to increase in boilers operating with low NOx combustion techniques and those operating at supercritical conditions. It is in these type of boilers where an effective combustion process is crucial.

7. RECOMMENDATIONS FOR FURTHER RESEARCH

The selection of samples to be tested and analysed was informed by the historical data on the areas with the highest tube failures and replacements. These were predominantly on the furnace walls and as a result this study was focused on this location of the boiler. Although not to the highest rate, there have been reported cases of tube failures in superheater and reheater areas which are believed to be due fireside corrosion. In order to determine the effective measures toward mitigation or effective management of fireside corrosion the type of corrosion existing on superheater and reheater should also be investigated.

Literature has shown that there is a tendency for an increase in fireside corrosion rate when the conventional subcritical boilers are operated with low NOx combustion techniques and when the boiler is operated at supercritical conditions. Future work is required in these areas to determine how the rate of fireside corrosion compares to conventional subcritical boilers.

REFERENCES

Asnavandi M., Kahram M., Rezaei M. and Rezakhani D. (2017), Fire-Side Corrosion: A Case Study of Failed Tubes of a Fossil Fuel Boiler, School of Chemistry, The University of New South Wales, Sydney, Australia, Chemistry and Materials Research Centre, Niroo Research Institute (NRI), Tehran, Iran, Department of Mining and Metallurgical Engineering, Amirkabir University of Technology, Tehran, Iran.

ASTM A105/A105M:18 (2018), Standard Specification for Carbon Steel Forgings for Piping Applications, ASTM International.

ASTM A106/A106M:18 (2018), Standard Specification for Seamless Carbon Steel Pipe for High-Temperature Service, ASTM International.

ASTM A370-06 (2006), Standard Test Methods and Definitions for Mechanical Testing of Steel Products, ASTM International.

ASTM E3-95 (1995), Standard Practice for Preparation of Metallurgical Specimens, ASTM International.

ASTM E92-17 (2017), Standard Test Methods for Vickers Hardness and Knoop Hardness of Metallic Materials, ASTM International.

Bakker W. (1998), Waterwall Wastage in Low NOx Boilers: Root Causes and Remedies, Electric Power Research Institute, Report TR11155.

Bakker W. (2001), Waterwall Wastage Mechanisms in Coal Fired Boilers: The Effect of Coal Chemistry on Waterwall Wastage. EPRI Report 1004021.

Borio R.W. and Levasseur A.A. (1986), Overview of Coal Ash Deposition in Boilers, Combustion Engineering Inc.

Broodryk G.J. (1995), A Systematic Approach to Fireside Boiler Tube Investigations, *MSc Chemistry Thesis*, University of the Witwatersrand.

Bryers R.W. (1995), Fireside Slagging, Fouling, and High-Temperature Corrosion of Heat-Transfer Surface due to Impurities in Steam-Raising Fuels, *Progress in Energy & Combustion Science*, Volume 22, page. 29-120.

BS EN 10216-2 (2013), Seamless Steel Tubes for Pressure Purposes – Technical Delivery Conditions, Part 2: Non-alloy and alloy steel tubes with specified elevated temperature properties, BSI Standard Publication.

Chou C.L. (1984-1986), Distribution of sodium, chlorine, and Sulphur in Illinois coals removal by cleaning and their behaviour during combustion, Final Technical Report.

Chou S.F., Daniels P.L., Rodgers L.W., Theus G.J. and Eskinazi D. (1985), Fireside Corrosion in Low-NOx Combustion Systems, *Proceeding Symposium Stationary Combustion NOx Control Volume I: Utility Boiler Applications*, pp. 19-1 - 19-22.

Clark, F. and Morris, C.W. (1980), Corrosion Resistance for Coal Systems, *D.B. Meadow Craft, M.I. Manning*, Applied Science, London.

Corey R.C., Grabowski H.A., and Cross B.J. (1949), Transactional ASME, pp. 951-963.

Corey, R.W. (1964), Measurements and Significance of the Flow Properties of Coal Ash Slag, Bureau of Mines Bulletin.

Cutler A.J.B. and Grant C.J. (1975), Corrosion of Iron and Nickel Base Alloys in Alkali Sulphate Melts, *Conf. Metal-Slag-Gas Reactions*, p. 951, Electrochemical Society, Inc.

Cutler, A.J.B. and Raask, E. (1981), External Corrosion in Coal-fired Coilers: Assessment from laboratory data, *Corrosion Science,* Volume 21, number 11, pp. 789-800.

Davis, C.J, James, P.J, Pinder, L.W. (2001), Mehta, A.K., Effects of Fuel Composition and Combustion Parameters on Furnace Wall Fireside Corrosion in Pulverised Coal-Fired Boilers, *Materials Science Forum*, Volumes. 369-372, pp. 857-864.

Dooley R.B. and McNaughton W.P. (2007), Boiler and Heat Recovery Steam Generator Tube Failures: Theory and Practice, Volume 2, EPRI Manual. 1012757.

Flatley T., Latham E.P. and Morris C.W. (1981), Co-extruded Tubes Improve Resistance to Fuel Ash Corrosion in U.K. Boilers, *Materials Performance*, Volume 20.

French D.N. (1982), Furnace Wall Corrosion problems in Coal Fired Boilers, Corporate Quality Assurance, Riley Power Inc., a Babcock Power Inc. company (formerly Riley Stoker Corporation), Presented at: National Association of Corrosion Engineers, Houston, Texas, March 22-26.

Haines P.J. (2001), Thermal Methods of Analysis – Principles, Applications and Problem, Chapter 1: Introduction to Thermal Methods, Springer Science and Business Media, 1995.
Harb J.N. and Smith E.E. (2010), Fireside Corrosion in PC-Fired Boilers, *Progress in Energy & Combustion Science*.

Harding N.S. and O'Connor D.C. (2007), Ash Deposition Impacts in the Power Industry, Fuel Processing Technology, Volume 88, number.1112, pp.1082–1093.

Hatt, R. M. (1990), Fireside Deposits in Coal-Fired Utility Boilers, *Progress in Energy and Combustion Science*, Volume 16, pp. 235-241.

Hendry, A. and Lees, D. J. (1980), Corrosion of Austenitic Steels in Molten Sulphate Deposits, *Corrosion Science,* Volume 20, number 3, pp. 383-404.

Hong Z. and Yong W. (2002), Discussion on the mechanisms and factors of the gas side high temperature corrosion in water wall tubes for coal fired boilers, *Power Engineering 2*.

Khanna, A. S. (2002), *Introduction to high temperature oxidation and corrosion,* ASM International, Materials Park, OH.

Kihara S., Nakagawa K. and Kajigaya I. (1998), Waterwall Corrosion in Low-NOx Combustion Boiler. Corrosion Control, pp. 99–106.

Lees D.J. and Whitehead M.E. (1983), Microanalysis of Scales and Deposits Formed on Corroding Furnaces Tubes in Coal-fired Boilers, *Corrosion Resistant Materials in Coal Conversion Systems*, D.B. Meadowcroft and M.I. Manning (Eds.), pp. 63-86, Applied Science Publishers.

Moore, H. (1995), Boiler: Fireside Fouling and Corrosion. *Material Selection and Corrosion, Volume II.*

Morinaga M., Najima S., Aramaki H., Wakabayashi N. and Shirai H. (2010), Evaluation of Sulphide Corrosion Conditions in a Pulverized Coal Fired Thermal Power Plant, Thermal Nuclear Power Generation Conv, pp. 78–85.

Natesan, K. and Park, J. H. (2007), Fireside and Steam-side Corrosion of Alloys for USC plants, *International Journal of Hydrogen Energy*, Volume 32, number 16, pp. 3689-3697.

Norton J.F. (1984), High Temperature Materials Corrosion in Coal Gasification Atmospheres, Elsevier Applied Science Publishers.

Otsuka N. (2010), Fireside Corrosion, Materials Science and Materials Engineering - Shreir's Corrosion, Volume 1: Basic Concepts, *High Temperature Corrosion*, pp. 457-481.

Reid, W.T. (1971), External Corrosion and Deposits: Boilers and Gas Turbines, Elsevier, New York.

Reid, W.T. (1984), The relation of mineral composition to slagging, fouling and erosion during and after combustion, *Progress Energy & Combustion Science*, Volume 10.

Reid W.T., Corey R.C. and Cross B.J. (1945), External Corrosion of Furnace-wall Tubes – I History and Occurrence, *Transactional ASME Volume 67*, pp 279-285.

Shirai H., Ikeda M. and Aramaki H. (2012), Characteristics of Hydrogen Sulphide Formation in Pulverized Coal Combustion, Central Research Institute of Electric Power Industry, Japan.

Samms, J. A, C. and Smith, W. D. (1961), High temperature gas side corrosion in water-tube boilers, British Coal Utilisation, Research Association Monthly Bulletin 25, p. 454.

Shamanna, S. and Schobert, H. H. (1997), Fireside corrosion of selected alloys by ash recovered from coal-water slurry combustion, *Fuel Processing Technology,* Volume 53, number 1-2, pp. 133-156.

Sherlock T. P., Wells C. H. and Dooley R. B. (1997), State of Knowledge Assessment for Accelerated Waterwall Corrosion with Low NOx Burners, Electric Power Research Institute, TR-107775.

Sherlock T. P., Wells C. H. and Dooley R. B. (1999), *Mitigation of Fireside Corrosion in Low NOx Boilers: A State of the Art Assessment of Materials Solutions,* Electric Power Research Institute, TR-112823.

Shreir L.L., Jarman R.A. and Burstein G.T. (1994), Chapter 1: Principles of Corrosion and Oxidation, Corrosion – Metal Environment Reactions, 3rd Edition, Volume 1, pp. 55-67.

Sidhu, T. S., Prakash, S. and Agrawal, R. D. (2006), Hot corrosion studies of HVOF NiCrBSi and Stellite-6 Coatings on a Ni-based Superalloy in an Actual Industrial Environment of a Coal Fired Boiler, *Surface and Coatings Technology,* Volume 201, number 3-4, pp. 1602-1612.

Srivastava, S. C., Godiwalla, K. M. and Banerjee, M. K. (1997), Fuel Ash Corrosion of Boiler and Superheater tubes, *Journal of Materials Science (UK)*, Volume 32, number 4, pp. 835-849.

Stringer J. (1983), High Temperature Corrosion Problems in Steam Boilers, *Proceeding Symposium Corrosion in Fossil Fuel Systems*, I.G. Wright (ed.), pp 1-28, Electrochemical Society, Inc.

Stringer, J. and Wright, I. G. (1995), Current limitations of high-temperature alloys in practical applications, *Oxidation of Metals*, Volume 44, number 1-2, pp. 265-308.

Syed A., Dr Simms N. and Prof. Oakey J. (2011), Fireside Corrosion Study of Superheater Materials in Advanced Power Plants, School of Applied Science, PhD.

Valero A. and Cortes C. (1996), Ash Fouling in Coal-Fired Utility Boilers, Monitoring and Optimization of On-load Cleaning, *Progress in Energy and Combustion Science*, Volume 22, pp. 189-200.

Van Alphen C. (2016), Coal Quality Management, Power Station Process Training, Module 3, Eskom.

Van Wyk, D.C. (2010), Station A Preliminary Report: Results of Data Gathered during Test on Unit 1 in January 2010, Generation Business Unit, Eskom, 2010.

Viswanathan, R. and Bakker, W. (2000), Materials for Boilers in Ultra Supercritical Power Plants, *2000 International Joint Power Generation Conference*, 23-26 July, Miami Beach, Florida.

Wells C.H., Sherlock T.P., Dooley R.B. (1997), State of Knowledge Assessment for Accelerated Waterwall Corrosion with Low NOx Burners, Electrical Power Research Institute, TR 107775.

Wu C. (2003), Experimental Studies on High Temperature Corrosion on Water Cooled Wall in Coal-fired power plant, PhD Thesis, Zhejiang University, Hangzhou, China.

Yu X., Gong B., Gao Q., Zhao Y., Tian C. and Zhang J. (2017), Investigation of Fireside Corrosion at Water-cooled Wall from a Coal-fired Power Plant in China, State Key Laboratory of Coal Combustion, School of Energy and Power Engineering, Huazhong University of Science & Technology, Hubei Key Laboratory of Water Jet Theory and New Technology, School of Power and Mechanical Engineering; Wuhan University, and Shenhua Guohua (Beijing) Electric Power Research Institute Co. Ltd., China.

Zhao, S., Xie, X., Smith, G. D. and Patel, S. J. (2005), The Corrosion of INCONEL Alloy 740 in Simulated Environments for Pulverized Coal-fired Boiler, Materials Chemistry and Physics, Volume 90, number 2-3, pp. 275-281.

APPENDICES

APPENDIX A – VISUAL INSPECTION OF THE TUBING SAMPLES

A.1 STATION A

Unit 2 tubes that ruptured as primary failure as a result of fireside corrosion and secondary failure caused by water washing from the primary failed tube, as shown in Figure A.1. Flash rust (corrosion product) on ruptured tubes and on adjacent tubing. Wall thinning is found at the fireside of non-ruptured tubes at the 10 o'clock and 2 o'clock positions. No indication of wall thinning or deposit on the coldside of the tube.

Figure A.1: Failed tubes on division wall of Unit 2 boiler from station A.

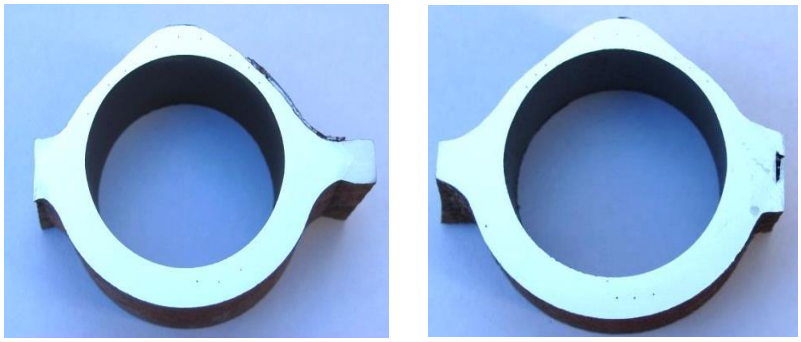

(a) (b)

Figure A.2: Tubing cross sectional samples from Unit 2 non-ruptured tubes of Station A, showing fireside deposit and wall thinning on the fireside.

A ruptured tube is amongst a bank of tubes removed from the side wall of the boiler, Figure A.3 (a). Wall thinning is also found at the fireside of non-ruptured tubes at the 10 o'clock and 2 o'clock positions, Figure A.4 (b). No indication of wall thinning or deposit on the coldside of the tube.

(a) (b)

Figure A.3: Failed tubes on division wall of Unit 2 boiler from station A.

(a) (b)

Figure A.4: Tubing samples from Unit 3 of Station A, showing fireside deposit (a) and wall thinning on the fireside (b).

Brown layer of sintered deposits on the external surface of fireside of the tubes form Unit 4 of Station A. The deposit is stable, intact, lifts off easily but does not crumble. Maximum wall thinning is found at the fireside of the tube at the 10 o'clock and 2 o'clock positions. No indication of wall thinning or deposit on the coldside of the tube.

(a) (b)

Figure A.5: Side wall tubing samples from Unit 4 of Station A, showing (a) fireside deposit and (b) wall thinning on the fireside.

A.2 STATION B

Thin and weak brown and reddish deposits on the fireside of Unit 1 tube with loosely bonded fly ash. The deposits crumble when handled. No scale or deposit on the coldside of the tube. A uniform wall thinning is seen around the tube.

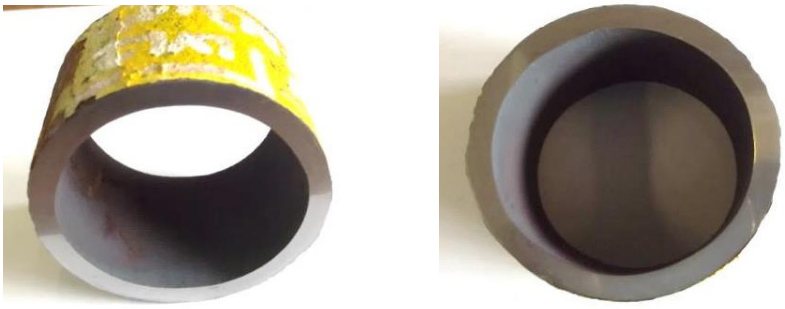

(a) (b)

Figure A.6: Tubing samples from division wall of Unit 1 of Station B, showing (a) fireside deposit and (b) wall thinning on the fireside.

Strong brown deposits sintered on the fireside of the tube. Figure A.7 (b) shows an inconsistent wall thinning around the tube. No scale or deposit on the non-fireside of the tube. No indication of wall thinning or deposit on the coldside of the tube.

(a) (b)

Figure A.7: Division wall tube sample from Unit 3 of Station B, showing (a) fireside deposit and (b) wall thinning on the fireside.

Weak fly ash deposits on the fireside of the tube. No signs of localized or preferred wall thinning around the tube circumference. No indication of wall thinning or deposit on the coldside of the tube.

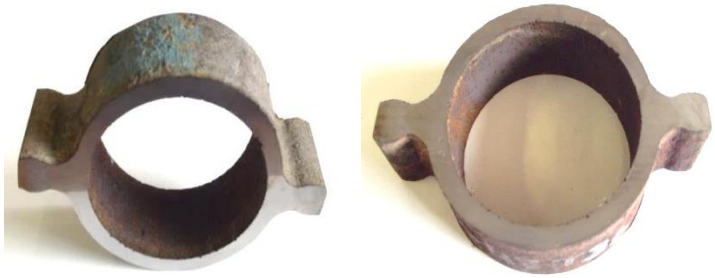

(a) (b)

Figure A.8: Side wall tube sample from Unit 8 of Station B, showing (a) fireside deposit and (b) wall thinning on the fireside.

Weak fly ash deposits on the fireside of the tube. Uniform wall thinning is visible on the fireside of the tube. No indication of wall thinning or deposit on the cold side of the tube.

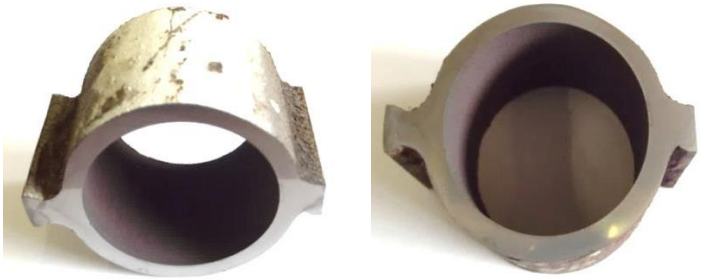

(a) (b)

Figure A.9: Division wall tube sample from Unit 10 of Station B, showing (a) fireside deposit and (b) wall thinning on the fireside.

A.3 STATION C

A very strong bonded metallic deposit was covering the fireside of the tube. Wall thinning can be seen on the fireside of the tube at 10 o'clock and 2 o'clock locations. There's no indication of wall thinning or deposit on the coldside of the tube.

(a) (b)

Figure A.10: Side wall tubing samples from Unit 4 of Station C, showing fireside deposit and wall thinning on the fireside.

A grey layer of sintered deposit is covering the fireside of the tube. The wall thinning on the fireside of the tube was located at the 10 o'clock and 2 o'clock positions. The coldside did show any sign of wall thinning or scaling.

(a) (b)

Figure A.12: Division wall tubing samples from Unit 6 of Station C, showing fireside deposit and wall thinning on the fireside.

APPENDIX B: MATERIAL CHEMICAL ANALYSIS

Table B.1: Chemical analysis of Station A

CHEMICAL ANALYSIS

Element		C	Mn	Si	P	S	Cr	Mo	Ni	Al	Cu	Nb	Ti	V	Sn	Sb	B
Specification	Max	0.20	0.90	0.35	0.030	0.025	0.30	0.35	0.30		0.30						
Requirement	Min	0.12	0.40					0.25									
Sample Tested		0.16	0.56	0.31	0.018	0.013	0.05	0.29	0.06	0.008	0.008	0.003	0.001	0.003	0.005	0.006	0.001

Results expressed in % **Note:** If specification is referenced, all specification values maximum unless otherwise stated.

Table B.2: Chemical analysis of Station B

CHEMICAL ANALYSIS

Element		C	Mn	Si	P	S	Cr	Mo	Ni	Al	Cu	Nb	Ti	V	Sn	Sb	B
Specification	Max	0.30	1.06		0.035	0.035	0.40	0.15	0.40		0.40			0.08			
Requirement	Min		0.29	0.10													
Sample Tested		0.17	0.72	0.24	0.009	0.005	0.05	0.06	0.15	0.03	0.18	0.002	0.003	0.001	0.021	0.009	0.001

Element		Cr+Cu+Mo+Ni+V
Specification	Max	1.00
Requirement	Min	
Sample Tested		0.44

Results expressed in % **Note:** If specification is referenced, all specification values maximum unless otherwise stated.

Table B.3: Chemical analysis of Station C

CHEMICAL ANALYSIS

Element		C	Mn	Si	P	S	Cr	Mo	Ni	Al	Cu	Nb	Ti	V	Sn	Sb	B
Specification	Max	0.30	1.06		0.035	0.035	0.40	0.15	0.40		0.40			0.08			
Requirement	Min		0.29	0.10													
Sample Tested		0.15	1.09	0.22	0.024	0.047	0.12	0.03	0.12	0.020	0.250	0.002	0.001	0.003	0.030	0.011	0.001

Element		Cr+Cu+Mo+Ni+V
Specification	Max	1.00
Requirement	Min	
Sample Tested		0.53

Results expressed in % **Note:** If specification is referenced, all specification values maximum unless otherwise stated.

APPENDIX C – HARDNESS TESTING

Table C1: Hardness Readings for Station A

Reading Number	**Unit 1**		**Unit 2**		**Unit 3**		**Unit 4**	
	Coldside	Fireside	Coldside	Fireside	Coldside	Fireside	Coldside	Fireside
1	143	152	146	141	143	152	139	146
2	138	142	139	150	152	157	142	135
3	151	155	145	140	143	168	133	131
4	135	147	144	144	-	155	145	130
Harness Average	**141**	**149**	**143**	**143**	**146**	**158**	**139**	**135**

Table C2: Hardness Readings for Station B

Reading Number	**Unit 1**				**Unit 3**				**Unit 8**		**Unit 10**	
	Coldside		Fireside		Coldside		Fireside		Coldside	Fireside	Coldside	Fireside
1	125	135	131	126	157	138	151	138	159	138	124	145
2	132	134	133	126	152	140	138	135	150	141	126	141
3	131	132	130	132	147	139	137	136	147	146	126	135
4	136	134	131	132	145	137	143	137	146	148	131	139
Hardness Average	**132**		**131**		**144**		**139**		**150**	**143**	**126**	**140**

Table C3: Hardness Readings for Station C

Reading Number	**Unit 4**		**Unit6**	
	Coldside	Fireside	Coldside	Fireside
1	140	134	148	145
2	145	138	145	143
3	136	156	151	151
4	-	-	146	152
Hardness Average	**140**	**142**	**147**	**147**

APPENDIX D – MICROSTRUCTURAL EXAMINATION

Metallographically prepared tubing samples were examined under an optical microscope and the results are presented in this Appendix, showing a pearlite and ferrite microstructure.

D.1 STATION A

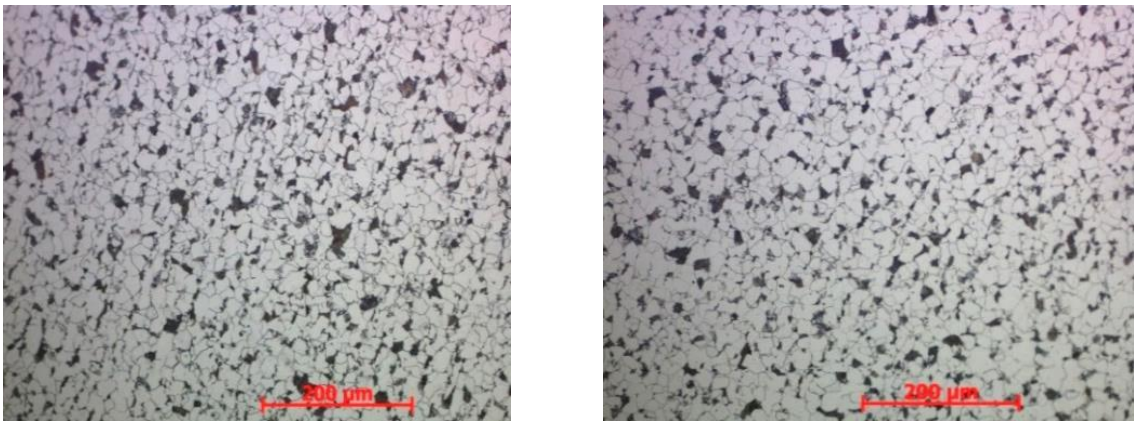

a **b**

Figure D.1: Microstructure of side wall tube 181 on the (a) fireside and (b) coldside.

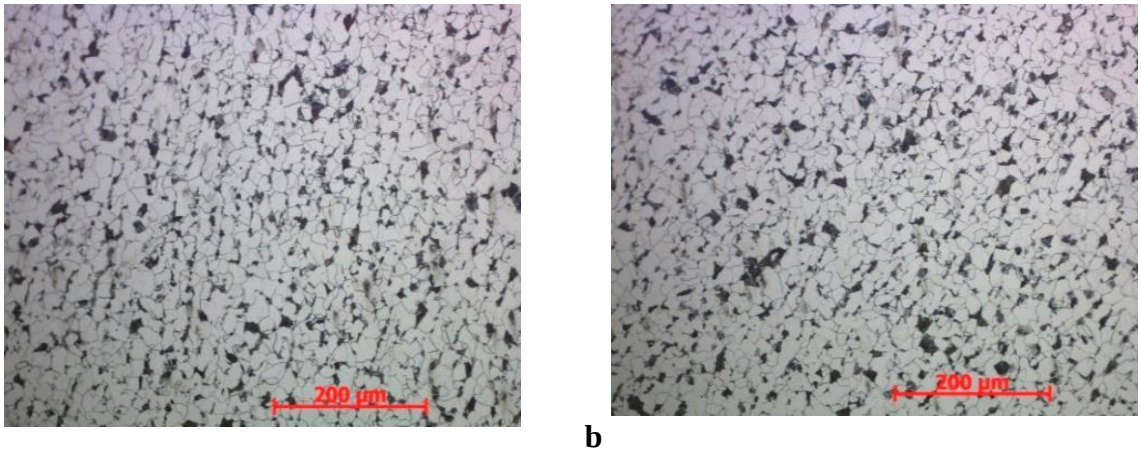

a **b**

Figure D.2: Microstructure of side wall Tube 49 on the (a) fireside and (b) coldside.

D.2 STATION B

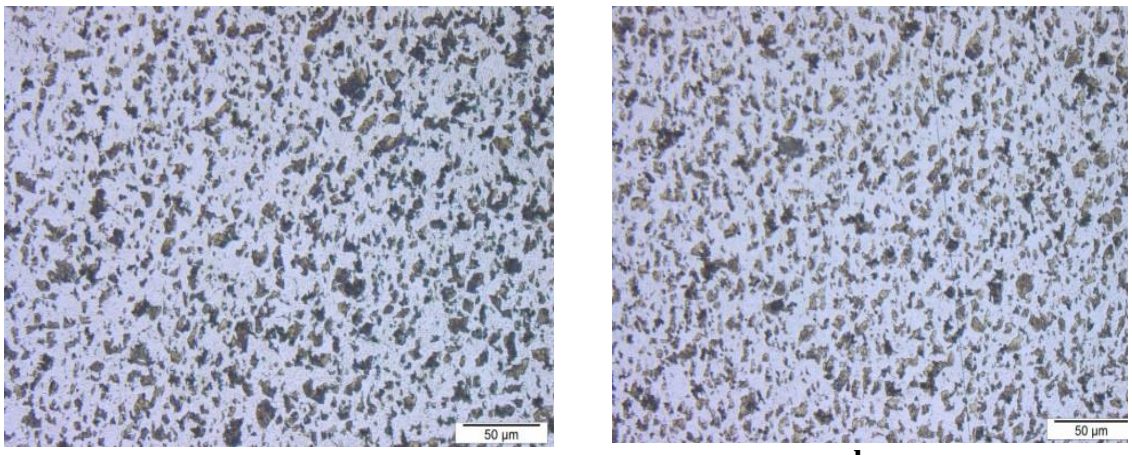

a **b**

Figure D.3: Microstructure of Unit 1 front wall tube on the (a) fireside and (b) coldside

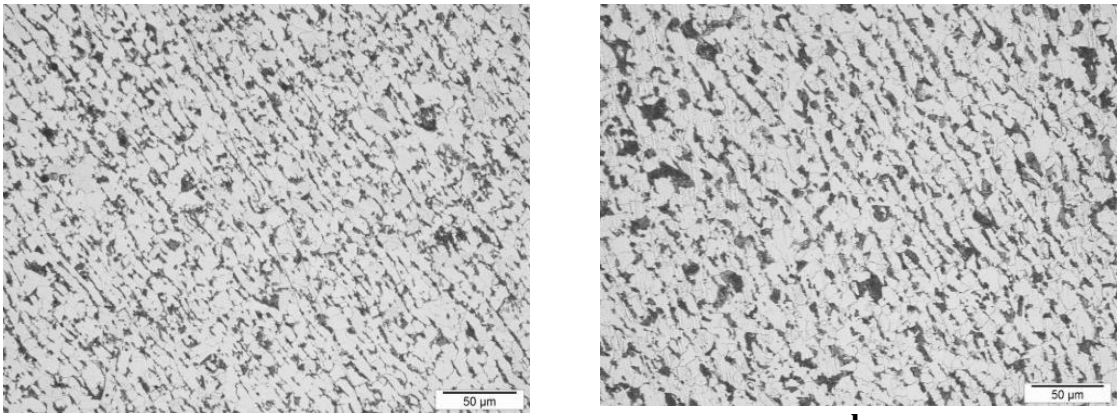

a **b**

Figure D.4: Microstructure of Unit 3 division wall tube on the (a) fireside and (b) coldside

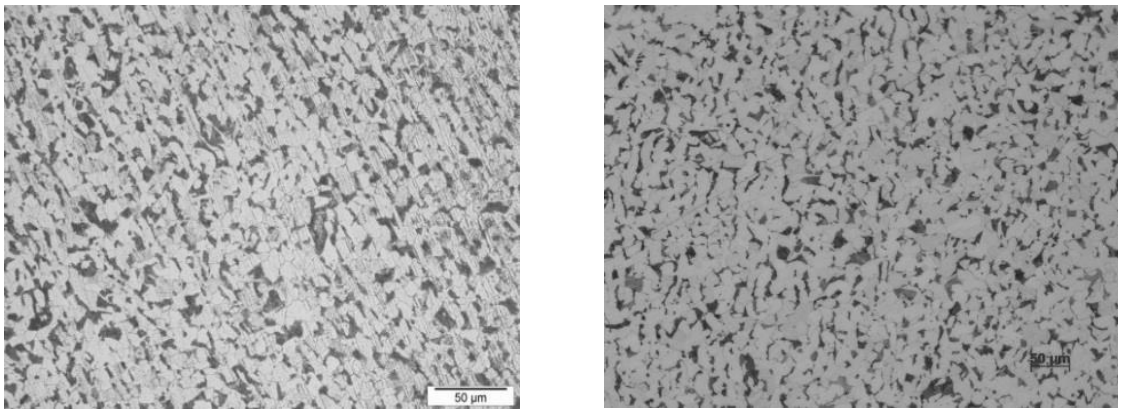

a **b**

Figure D.5: Microstructure of Unit 8 division wall tube on the (a) fireside and (b) coldside

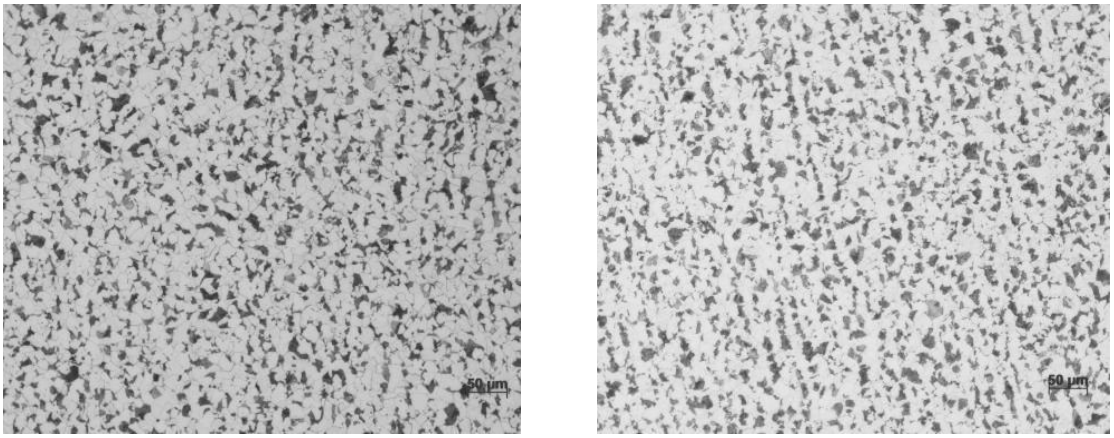

a **b**

Figure D.6: Microstructure of Unit 10 division wall tube on the (a) fireside and (b) coldside

D.3 STATION C

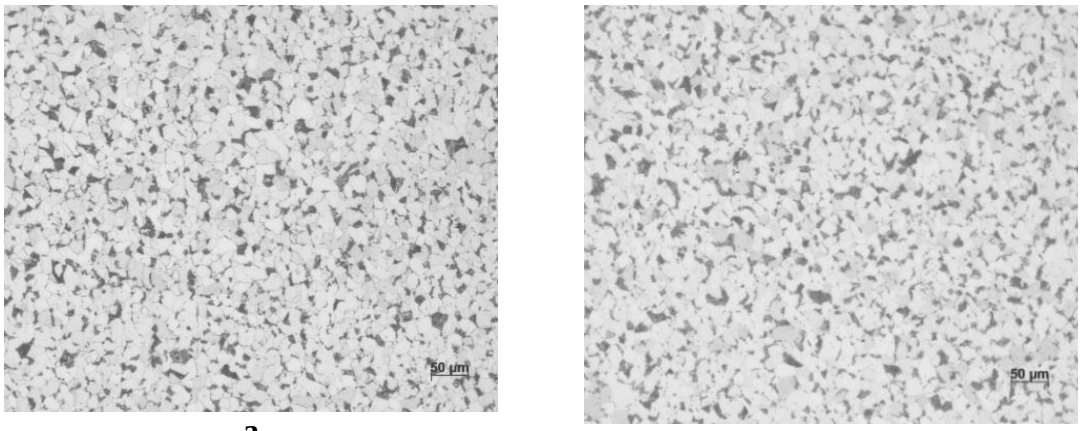

a **b**

Figure D.7: Microstructure of Unit 4 side wall tube on the (a) fireside and (b) coldside

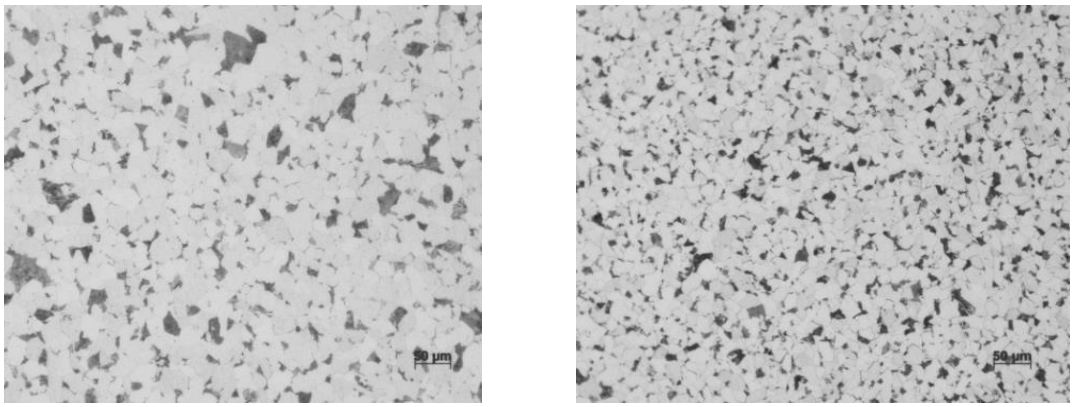

a **b**

Figure D.8: Microstructure of Unit 6 side wall tube on the (a) fireside and (b) coldside

APPENDIX E – SCANNING ELECTRON MICROSCOPY (SEM) ANALYSIS

E.1 STATION A

(a) 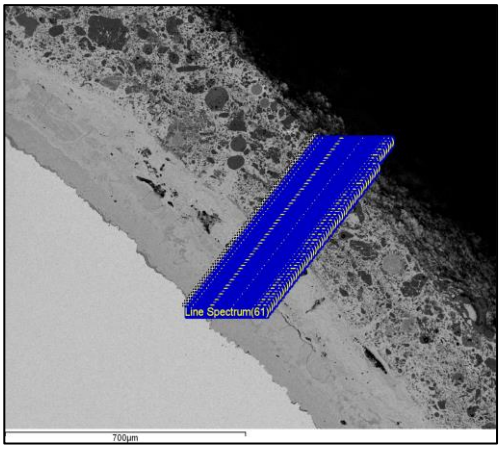

(b) 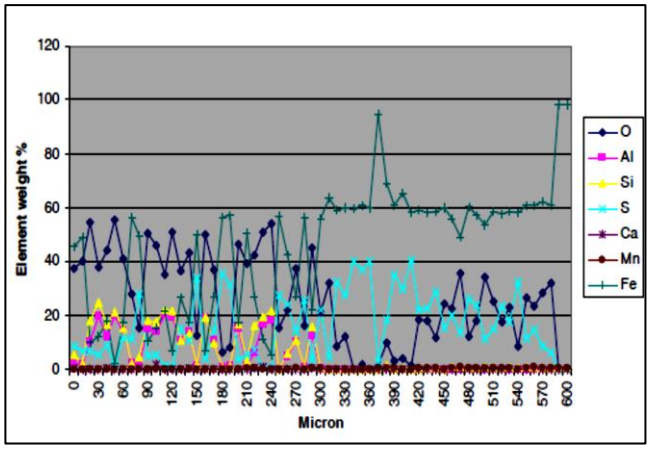

Figure E.1: SEM analysis of Station A Unit 1 – Sample 2 showing (a) EDS line map of the fireside deposit, (b) Elemental composition of the fireside deposit as per EDS line map.

(a) 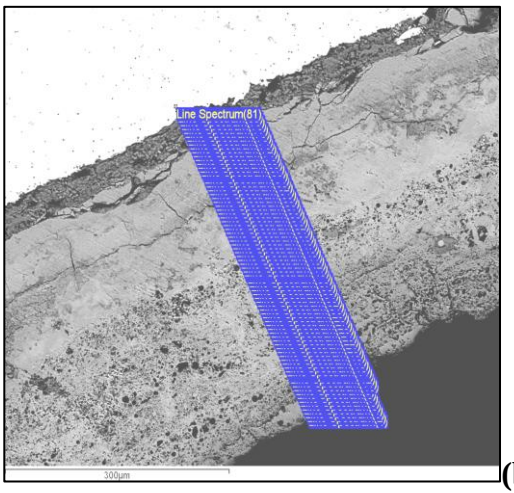

(b) 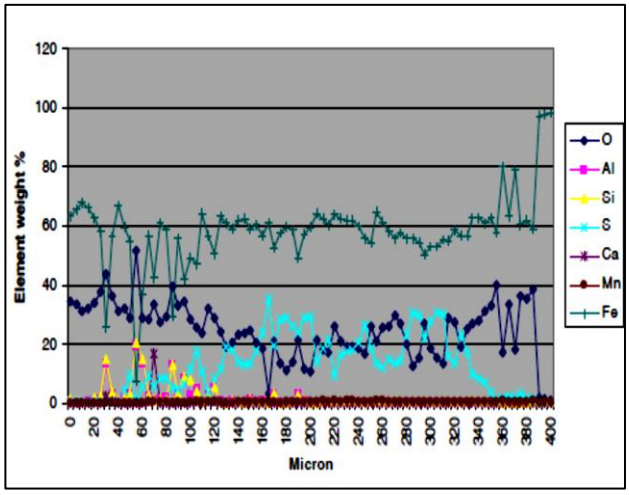

Figure E.2: SEM analysis of Station A Unit 3 – GB-24-32 showing (a) EDS line map of the fireside deposit, (b) Elemental composition of the fireside deposit as per EDS line map.

E.2 STATION B

(a) 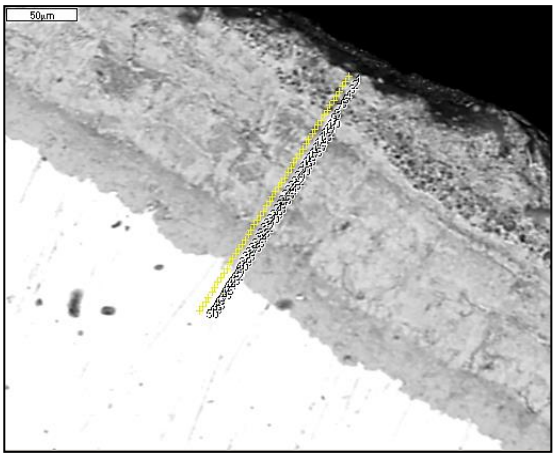

(b) 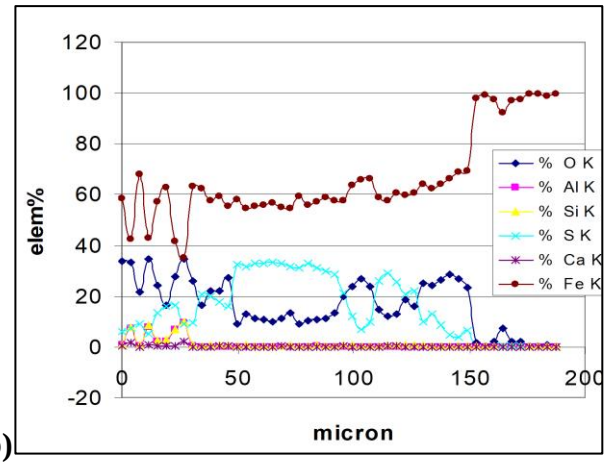

Figure E.3: SEM analysis of Station B Unit 1 – Sample 1 showing (a) EDS line map of the fireside deposit, (b) Elemental composition of the fireside deposit as per EDS line map.

(a) 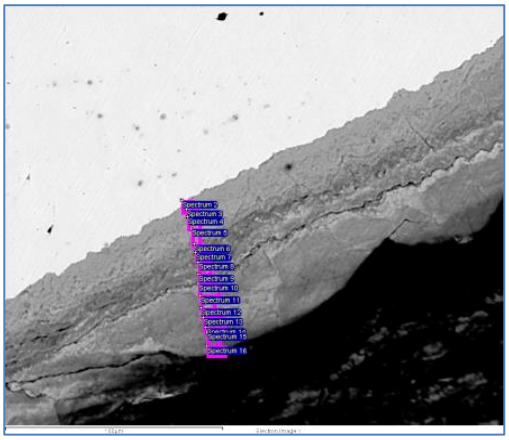

(b) 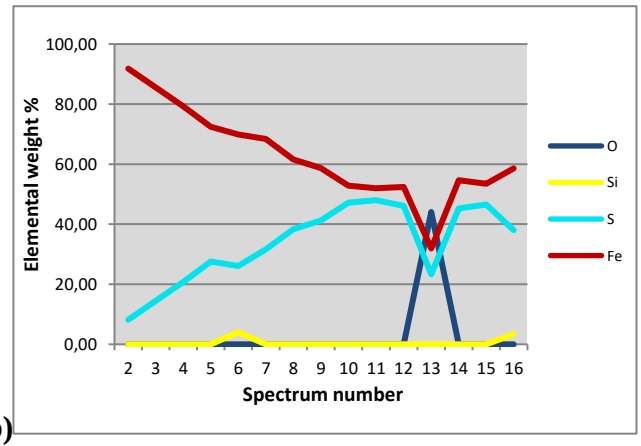

Figure E.4: SEM analysis of Station B Unit 3 – Sample U3-B1 showing (a) EDS line map of the fireside deposit, (b) Elemental composition of the fireside deposit as per EDS line map.

E.3 STATION C – UNIT 4

(a) 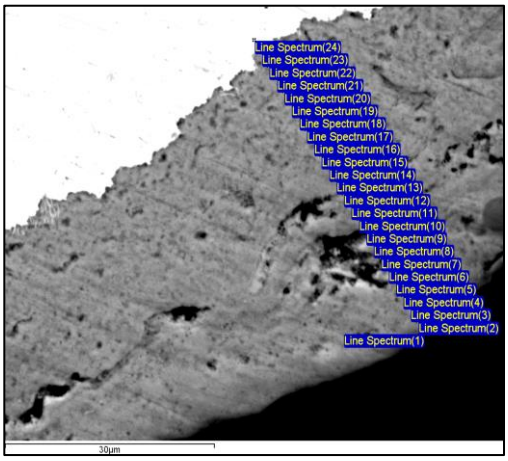

(b) 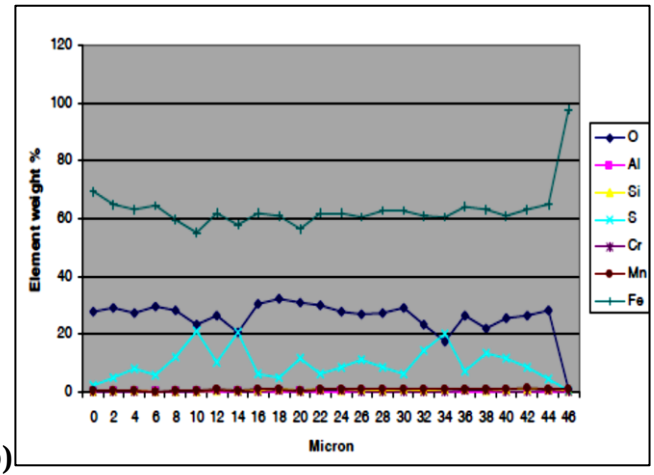

Figure E.5: SEM analysis of Station C Unit 4 (SW 2.1A) Ashowing (a) EDS line map of the fireside deposit, (b) Elemental composition of the fireside deposit as per EDS line map.

(a) 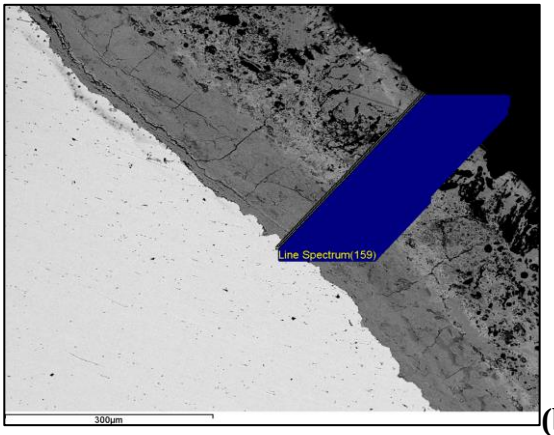

(b) 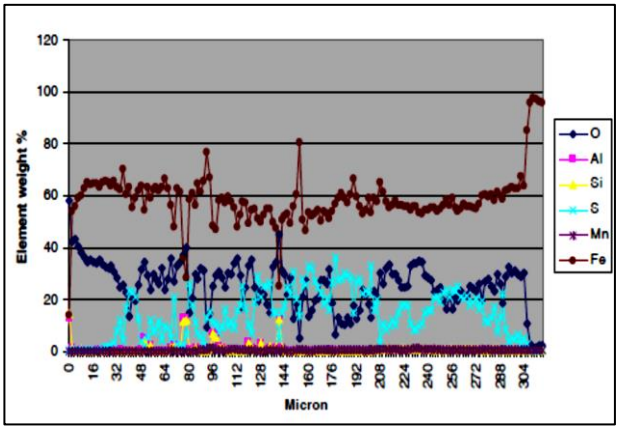

Figure E.6: SEM analysis of Station C Unit 4 (SW 1.7) showing (a) EDS line map of the fireside deposit, (b) Elemental composition of the fireside deposit as per EDS line map.

APPENDIX F – QEMSCAN ANALYSIS OF THE FIRESIDE DEPOSIT

F.1 STATION A

Samples A, B and C were taken from the fireside and sample D from the coldside of the tubes.

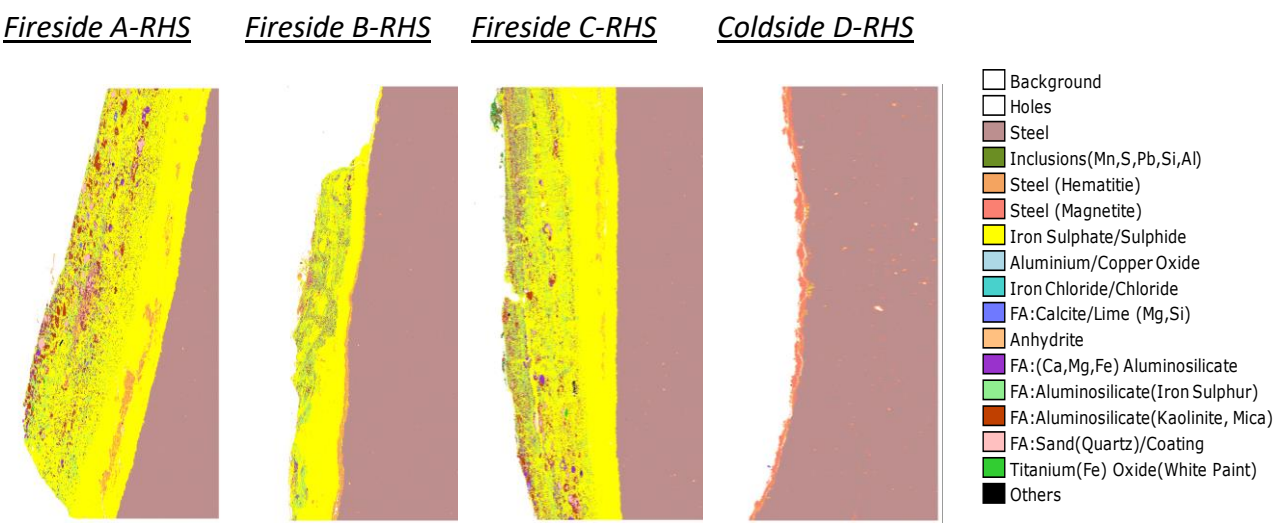

Figure F.1: Mineralogy analysis of Station A Unit 1- RHS fireside scale.

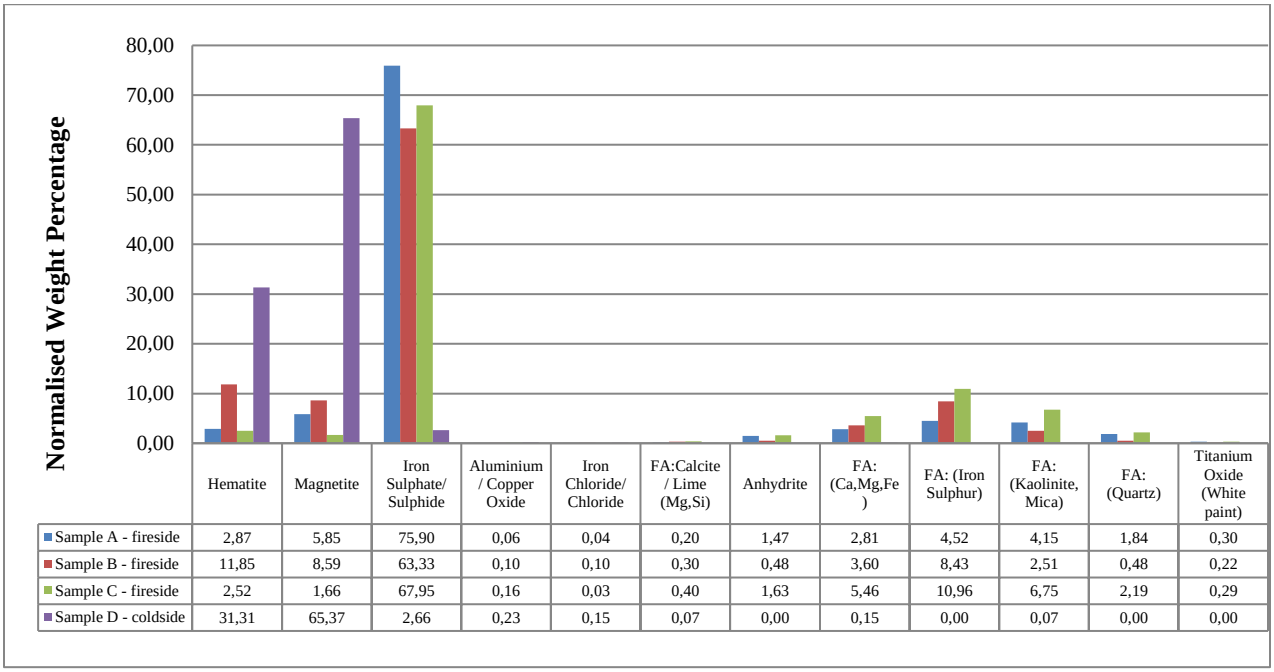

	Hematite	Magnetite	Iron Sulphate/ Sulphide	Aluminium / Copper Oxide	Iron Chloride/ Chloride	FA:Calcite / Lime (Mg,Si)	Anhydrite	FA: (Ca,Mg,Fe)	FA: (Iron Sulphur)	FA: (Kaolinite, Mica)	FA: (Quartz)	Titanium Oxide (White paint)
Sample A - fireside	2,87	5,85	75,90	0,06	0,04	0,20	1,47	2,81	4,52	4,15	1,84	0,30
Sample B - fireside	11,85	8,59	63,33	0,10	0,10	0,30	0,48	3,60	8,43	2,51	0,48	0,22
Sample C - fireside	2,52	1,66	67,95	0,16	0,03	0,40	1,63	5,46	10,96	6,75	2,19	0,29
Sample D - coldside	31,31	65,37	2,66	0,23	0,15	0,07	0,00	0,15	0,00	0,07	0,00	0,00

Figure F.2: Mineralogical Constituency of Station A Unit 1 fireside (A, B, C) and coldside (D) surfaces.

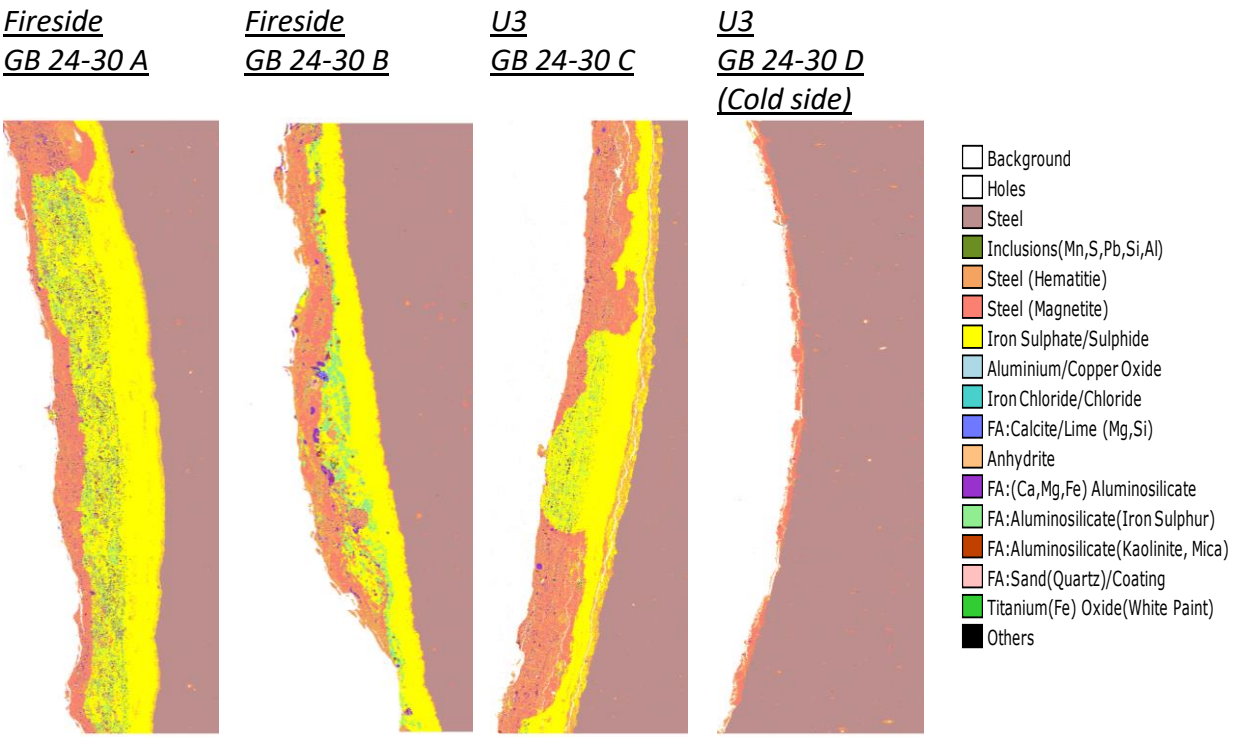

Figure F.3: Mineralogy analysis of Station A Unit 3- GB 24-30 fireside scale and coldside.

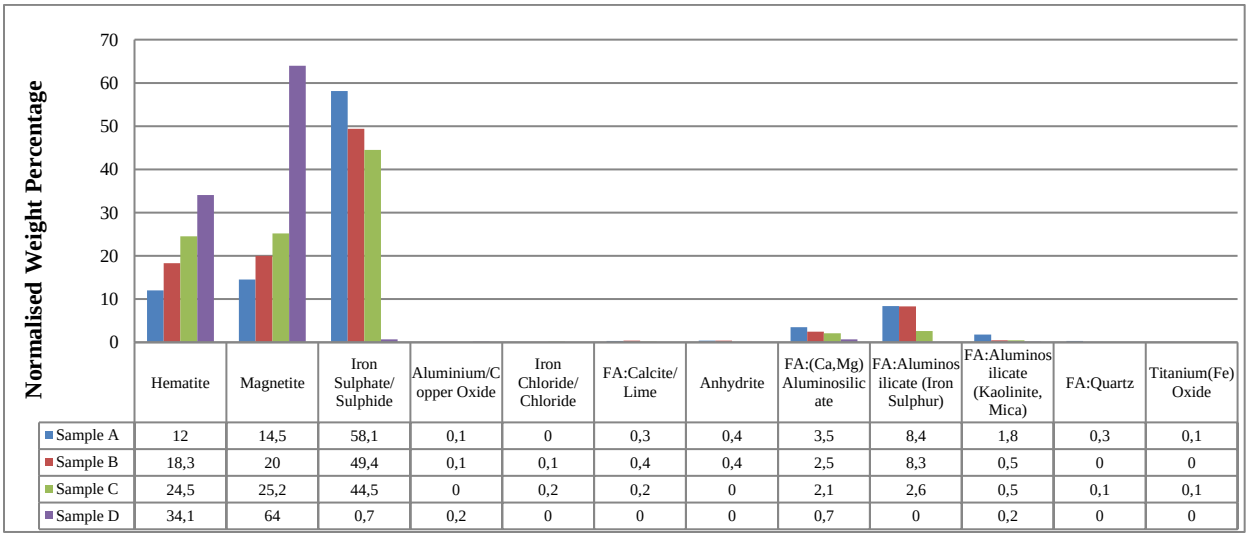

	Hematite	Magnetite	Iron Sulphate/ Sulphide	Aluminium/Copper Oxide	Iron Chloride/ Chloride	FA:Calcite/ Lime	Anhydrite	FA:(Ca,Mg) Aluminosilicate	FA:Aluminosilicate (Iron Sulphur)	FA:Aluminosilicate (Kaolinite, Mica)	FA:Quartz	Titanium(Fe) Oxide
Sample A	12	14,5	58,1	0,1	0	0,3	0,4	3,5	8,4	1,8	0,3	0,1
Sample B	18,3	20	49,4	0,1	0,1	0,4	0,4	2,5	8,3	0,5	0	0
Sample C	24,5	25,2	44,5	0	0,2	0,2	0	2,1	2,6	0,5	0,1	0,1
Sample D	34,1	64	0,7	0,2	0	0	0	0,7	0	0,2	0	0

Figure F.4: Mineralogical Constituency of Station A Unit 3 fireside and coldside (D) surfaces.

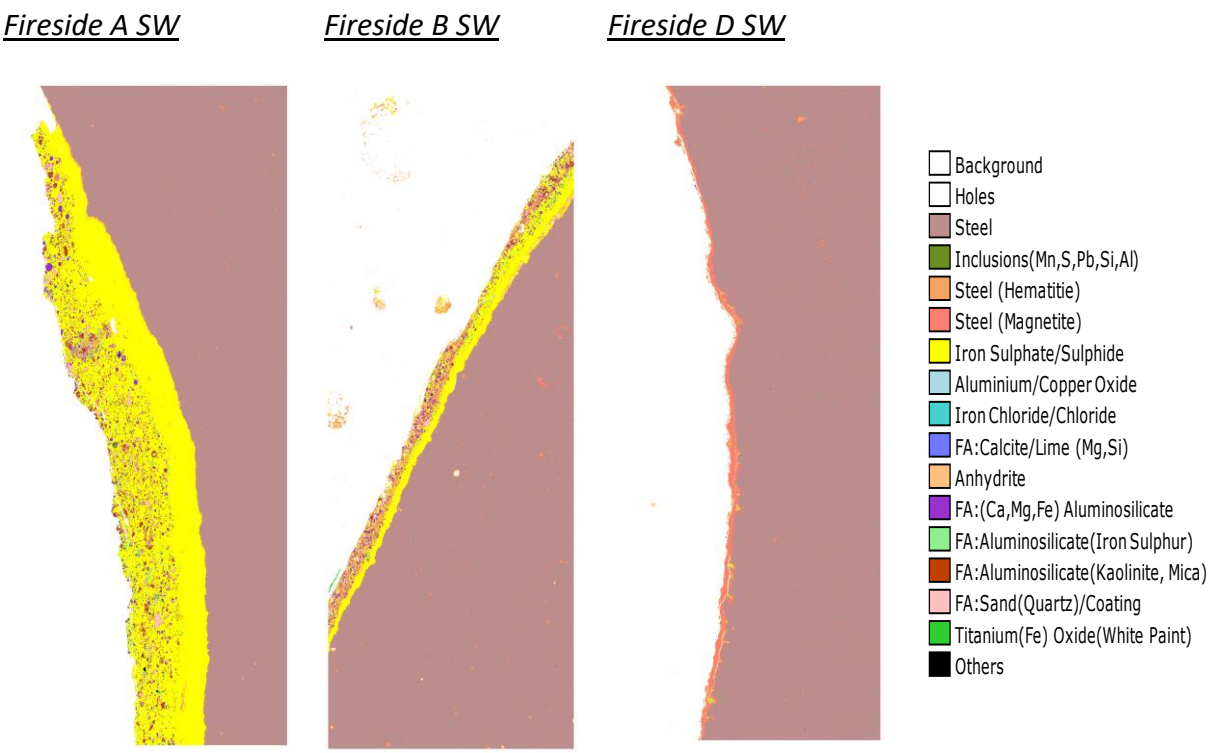

Figure F.5: Mineralogy analysis of Station A Unit 4 fireside scale.

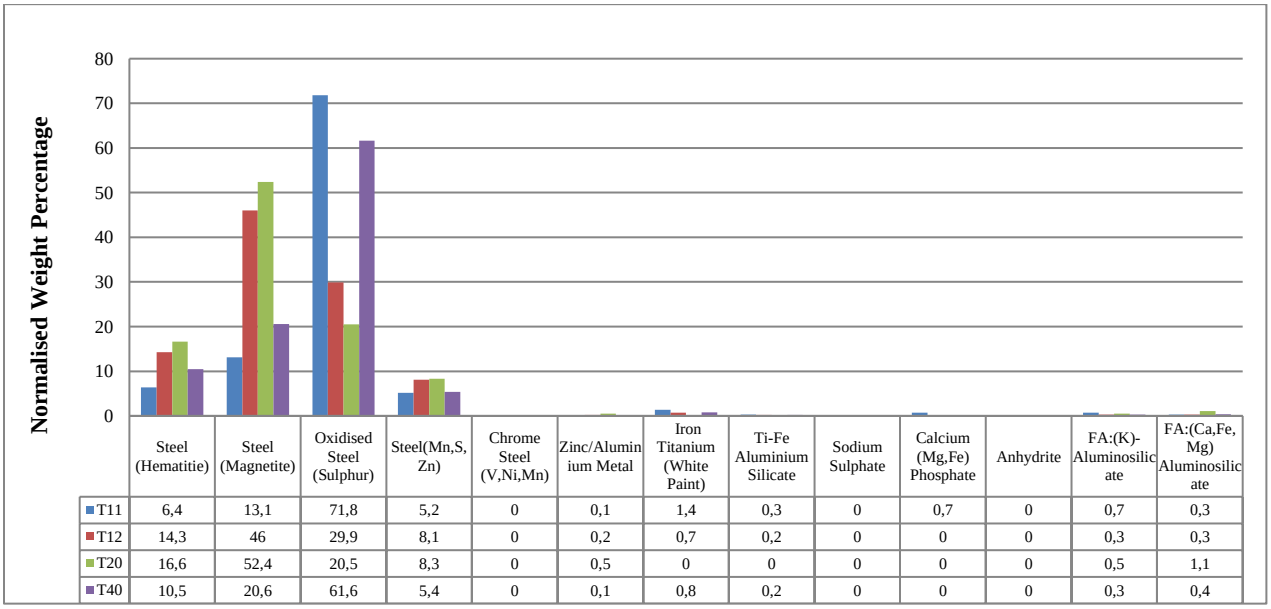

	Steel (Hematitie)	Steel (Magnetite)	Oxidised Steel (Sulphur)	Steel(Mn,S, Zn)	Chrome Steel (V,Ni,Mn)	Zinc/Aluminium Metal	Iron Titanium (White Paint)	Ti-Fe Aluminium Silicate	Sodium Sulphate	Calcium (Mg,Fe) Phosphate	Anhydrite	FA:(K)-Aluminosilicate	FA:(Ca,Fe, Mg) Aluminosilicate
T11	6,4	13,1	71,8	5,2	0	0,1	1,4	0,3	0	0,7	0	0,7	0,3
T12	14,3	46	29,9	8,1	0	0,2	0,7	0,2	0	0	0	0,3	0,3
T20	16,6	52,4	20,5	8,3	0	0,5	0	0	0	0	0	0,5	1,1
T40	10,5	20,6	61,6	5,4	0	0,1	0,8	0,2	0	0	0	0,3	0,4

Figure F.6: Mineralogical constituency of Station A Unit 4 tubes fireside.

F.2 STATION C

F.2.1 Unit 4 - RHS SW

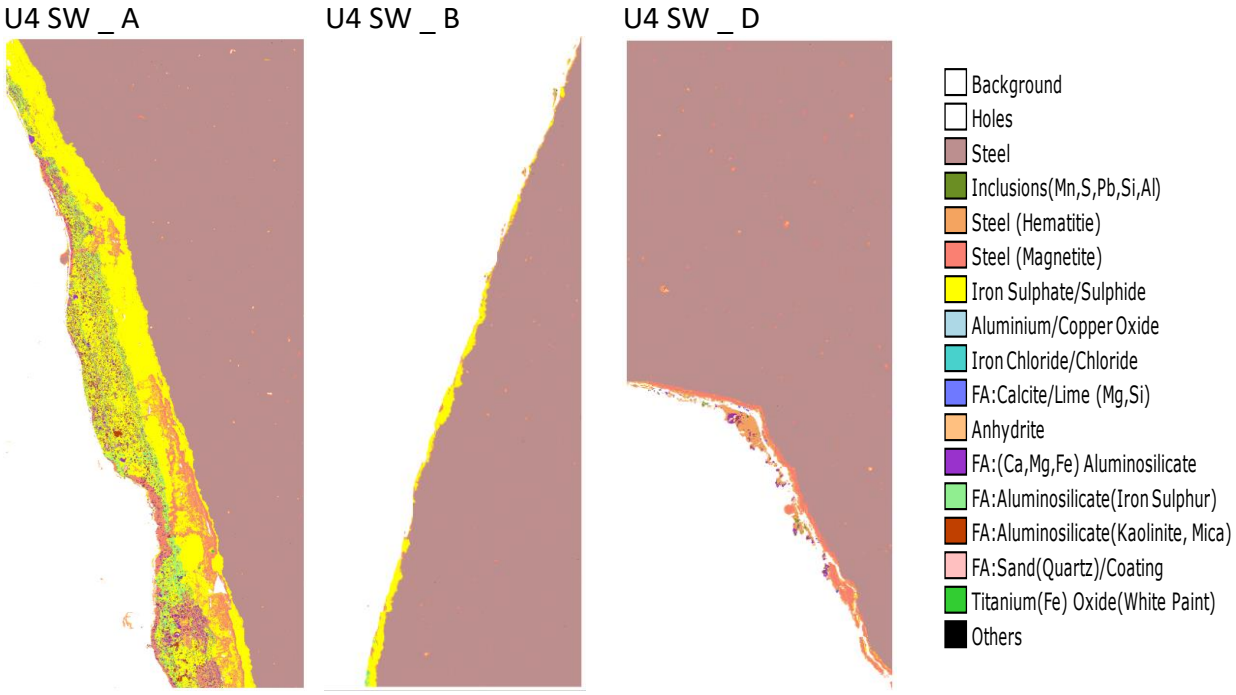

Figure F.7: Mineralogy analysis of Station C Unit 4 RHS SW fireside scale (A, B) and coldside (D).

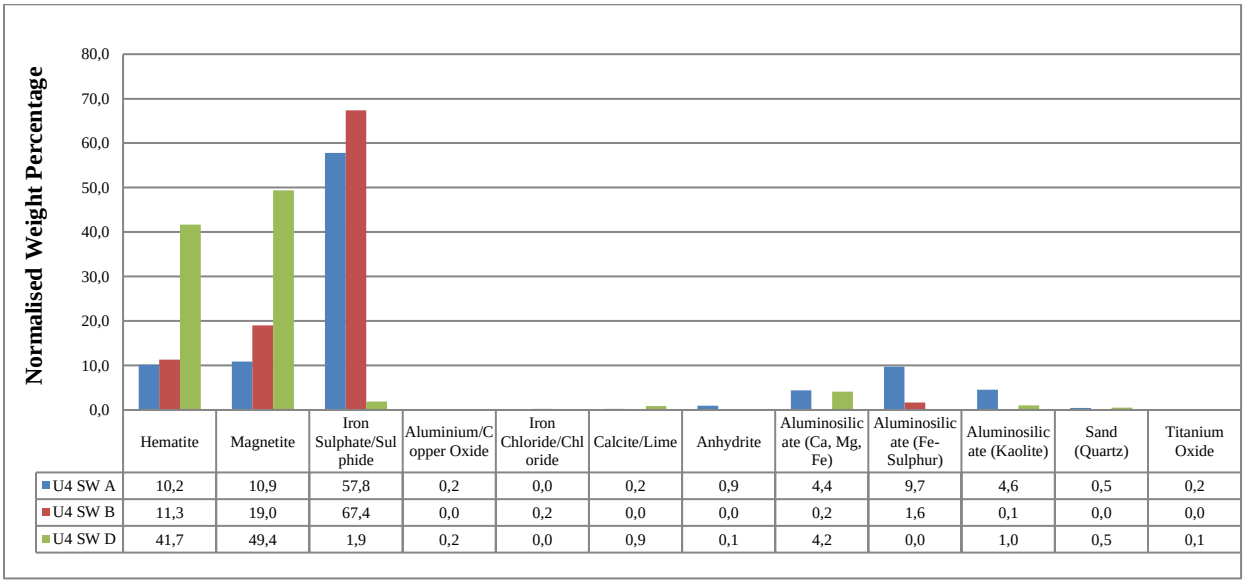

	Hematite	Magnetite	Iron Sulphate/Sulphide	Aluminium/Copper Oxide	Iron Chloride/Chloride	Calcite/Lime	Anhydrite	Aluminosilicate (Ca, Mg, Fe)	Aluminosilicate (Fe-Sulphur)	Aluminosilicate (Kaolite)	Sand (Quartz)	Titanium Oxide
U4 SW A	10,2	10,9	57,8	0,2	0,0	0,2	0,9	4,4	9,7	4,6	0,5	0,2
U4 SW B	11,3	19,0	67,4	0,0	0,2	0,0	0,0	0,2	1,6	0,1	0,0	0,0
U4 SW D	41,7	49,4	1,9	0,2	0,0	0,9	0,1	4,2	0,0	1,0	0,5	0,1

Figure F.8: Mineralogical constituency of Station A Unit 4 tubes fireside.

G. APPENDIX F: X-RAY DIFFRACTION (XRD) ANALYSIS

G.1 STATION A

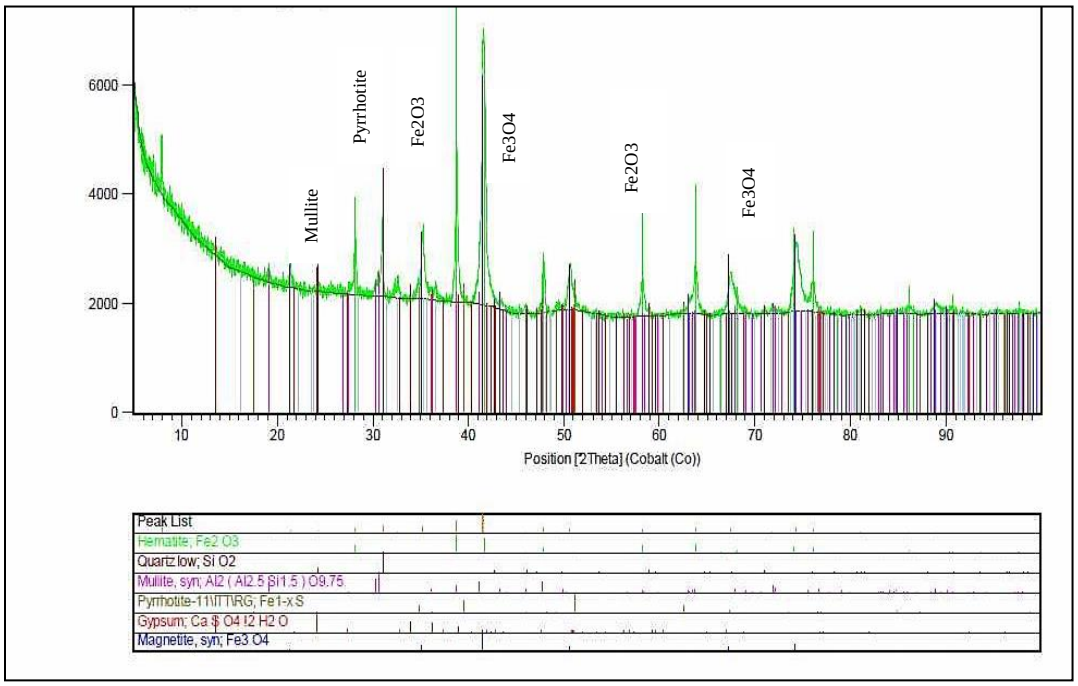

Figure G.1: XRD analysis of side wall tube (SW2) fireside deposit from Unit 1 of Station A.

Table G1: Mineralogical composition of SW2 fireside deposit from Station A

Component	Weight %	% Error	Corrected weight %
Gypsum	1.49	0.63	0.86
Hematite	31.47	1.08	30.39
Iron-alpha	0.71	0.19	0.52
Magnetite	49.11	1.41	47.7
Mullite	9.91	1.86	8.05
Pyrrhotite	1.4	0.39	1.01
Quartz	4.23	0.99	3.24
Wuestite	1.69	0.36	1.33

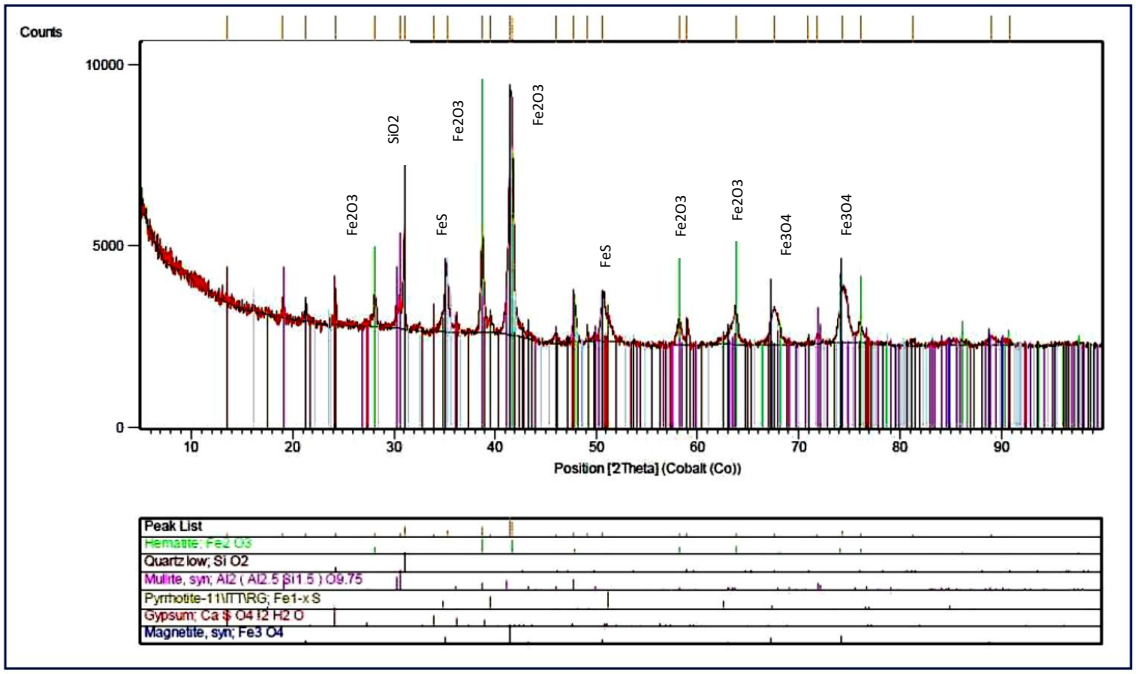

Figure G.2: XRD analysis of sidewall tube (SW_2009) fireside deposit from Unit 3 of Station A.

Table G2: Mineralogical composition of SW_2009 fireside deposit from Station A

Component	Weight %	% Error	Corrected weight%
Gypsum	2.51	0.69	1.82
Hematite	21.74	0.72	21.02
Iron-alpha	0.7	0.17	0.53
Magnetite	48.45	1.08	47.37
Mullite	15.64	1.2	14.44
Pyrrhotite	3.71	0.33	3.38
Quartz	6.7	0.81	5.89
Wuestite	0.56	0.15	0.41

G.2 STATION B

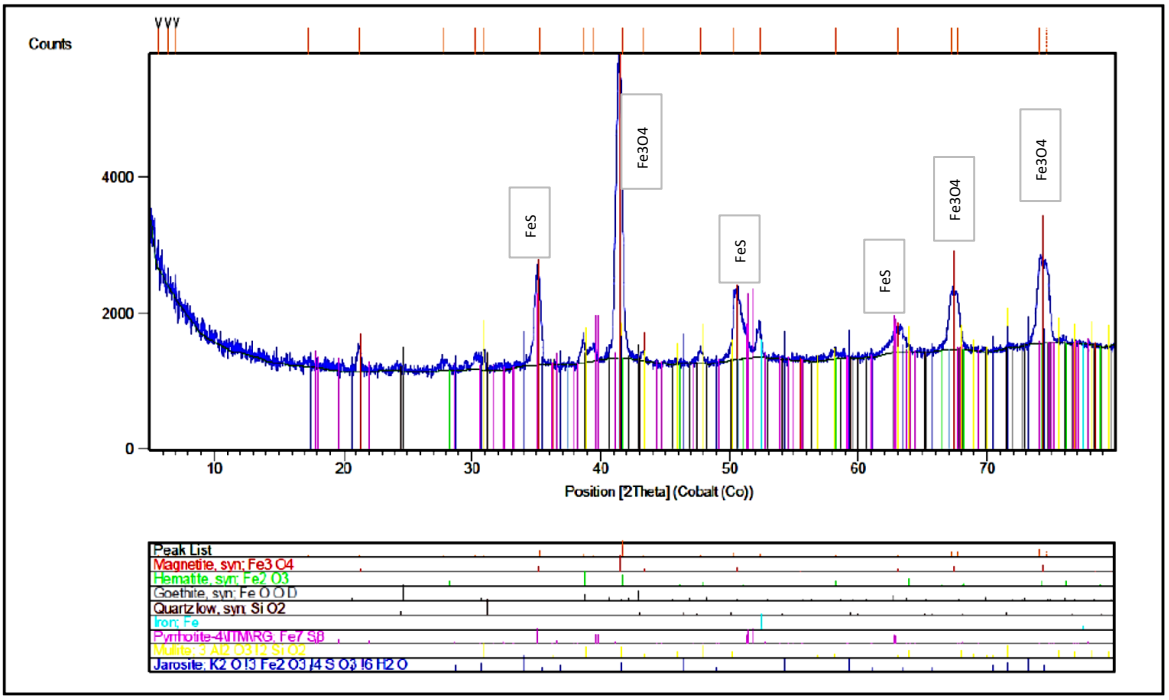

Figure G.3: XRD analysis of the division wall tube (DW2) fireside deposit from Unit 1 of Station B.

Table G3: Mineralogical composition of DW2 fireside deposit from U1 of Station B

Component	Weight %	Error	Corrected weight %
Goethite	3.65	1.11	2.54
Hematite	6.03	0.78	5.25
Iron alpha	3.31	0.27	3.04
Jarosite	0.93	0.9	0.03
Magnetite	71.57	1.92	69.65
Mullite	7.4	1.59	5.81
Pyrrhotite	5.61	0.48	5.13
Quartz	1.49	0.54	0.95

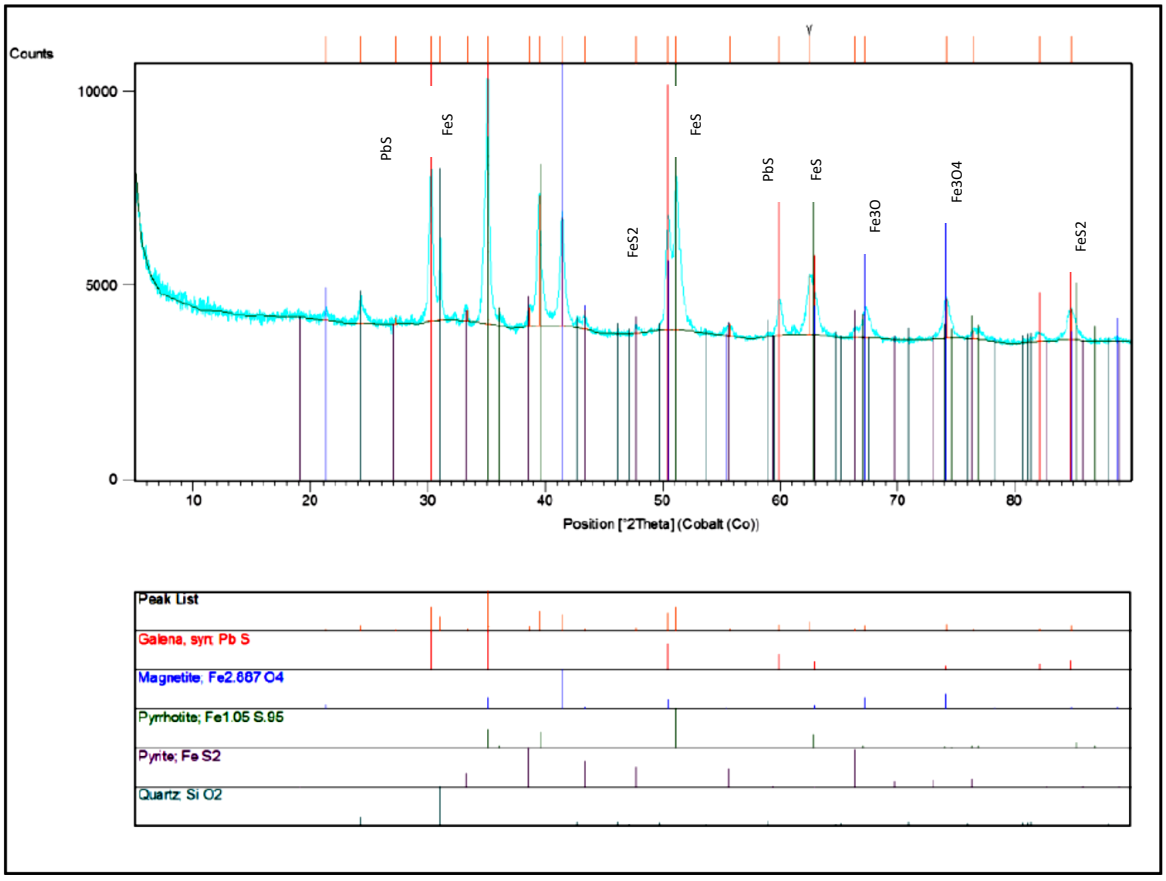

Figure G.4: XRD analysis of the side wall tube (T70) fireside deposit from Unit 3 of Station B.

Table G4: Mineralogical composition of T70 fireside deposit from U3 of Station B

Component	Weight%	Error	Corrected weight%
Galena	5.84	0.24	5.6
Magnetite	32.97	1.11	31.86
Pyrite	3.72	0.51	3.21
Pyrrhotite	50.03	1.38	48.65
Quartz	7.44	1.59	5.85

F.3 STATION C

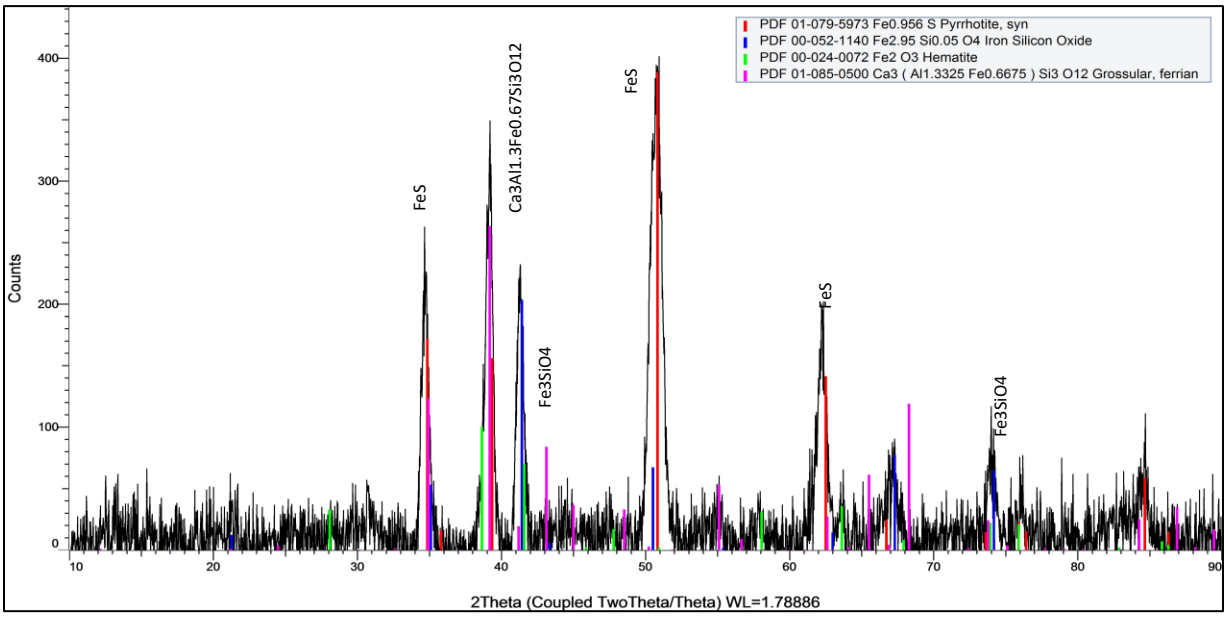

Figure G.5: XRD analysis of sidewall tube fireside deposit from Unit 4 of Power Station C.

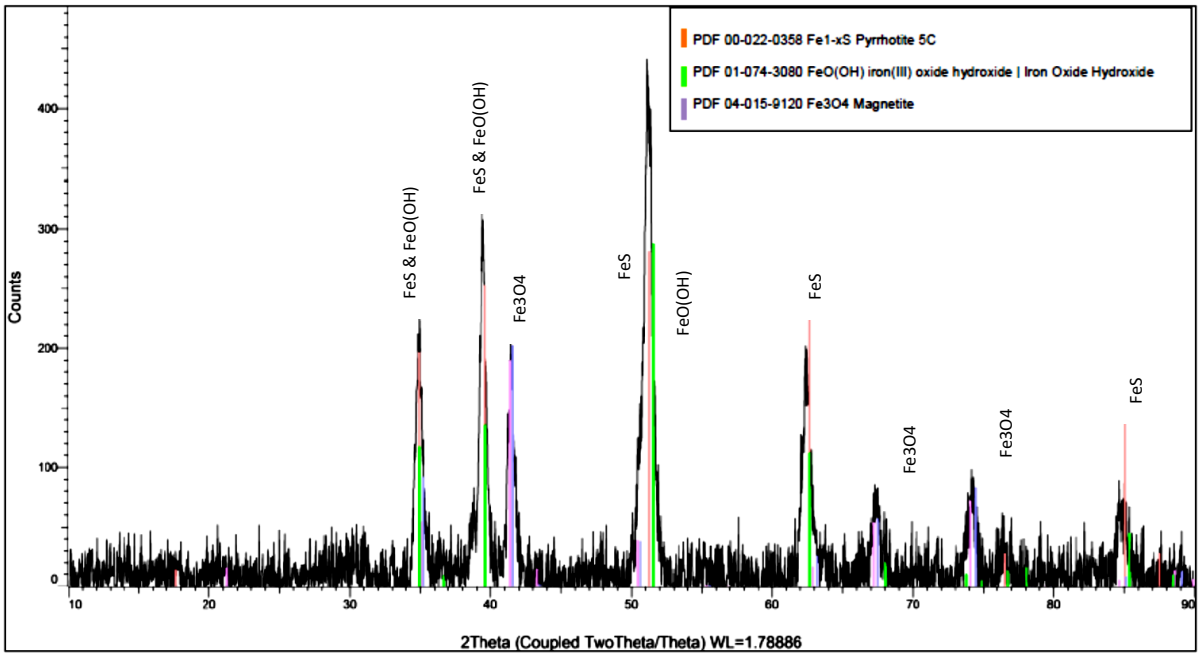

FigureG.6: XRD analysis of sidewall tube fireside deposit from Unit 6 of Power Station C.

APPENDIX H: COAL COMPOSITES FOR STATIONS A, B, and C

Table H1: Properties of coal used at Station A from year 2010 to 2017

	Abrasive Index	Ash %	Volatile Matter	Fixed Carbon	Total Sulphur	Total CO2	Calorific Value	Carbon	Hydrogen	Nitrogen	Oxygen
2010	2.25	30.31	21.16	46.28	**0.94**	1.71	22.14	55.35	2.65	1.22	5.53
2011	2.38	29.13	20.73	48.09	**0.85**	2.54	22.00	56.47	2.63	1.25	5.00
2012	2.24	29.40	20.59	47.77	**0.85**	2.77	22.00	54.89	2.62	1.14	6.10
2013	2.14	29.37	20.89	47.60	**0.91**	2.85	22.14	55.90	2.92	1.26	4.53
2014	2.36	29.41	20.42	47.81	**0.85**	2.80	22.05	55.51	2.80	1.33	4.86
2015	2.03	29.01	20.47	48.49	**0.89**	2.82	22.22	56.35	2.99	1.37	4.48
2016	2.02	29.88	21.18	46.93	**0.95**	2.76	21.94	55.23	2.74	1.34	4.93
2017	2.38	28.86	23.29	45.47	**1.00**	2.73	22.14	55.78	2.80	1.39	4.97

Table H2: Properties of the coal used at Station B from year 2010 to 2017

	Abrasive Index	Ash %	Volatile Matter	Fixed Carbon	Total Sulphur	Total CO2	Calorific Value	Carbon	Hydrogen	Nitrogen	Oxygen
2010	1.90	27.61	24.59	45.90	**1.18**	1.07	22.42	57.31	2.97	1.34	6.14
2011	2.40	27.78	20.08	46.23	**1.13**	1.07	22.38	56.57	2.78	1.31	5.96
2012	2.46	27.53	23.10	46.98	**1.19**	1.07	22.10	56.33	2.87	1.30	5.60
2013	2.54	28.28	21.98	47.20	**1.17**	1.07	21.79	55.44	2.91	1.27	5.58
2014	2.73	28.20	22.89	46.18	**1.10**	1.07	21.79	54.31	2.95	1.29	6.04
2015	2.57	27.83	24.24	45.36	**1.09**	1.07	22.60	55.82	3.12	1.36	5.41
2016	2.87	26.03	24.88	46.23	**1.04**	1.07	22.77	56.79	3.07	1.42	5.93
2017	3.46	24.73	24.67	47.14	**0.92**	1.07	23.02	57.78	2.96	1.46	5.93

Table H3: Properties of coal used at Station C from year 2010 to 2017

	Abrasive Index	Ash %	Volatile Matter	Fixed Carbon	Total Sulphur	Total CO2	Calorific Value	Carbon	Hydrogen	Nitrogen	Oxygen
2010	4.36	28.92	23.19	43.53	0.79	2.18	19.94	47.50	2.60	1.21	7.49
2011	4.64	29.73	22.25	43.25	0.86	2.60	18.21	51.24	2.49	1.16	7.14
2012	4.68	27.84	22.72	44.76	0.95	2.71	20.49	53.45	2.51	1.22	6.64
2013	4.51	28.01	22.31	45.17	0.90	2.68	20.16	52.98	2.77	1.23	6.76
2014	4.42	28.88	20.46	40.63	0.75	2.43	18.42	47.90	2.50	1.16	6.57
2015	3.93	31.76	21.57	42.74	0.71	2.53	19.32	50.04	2.68	1.26	7.10
2016	4.13	31.68	21.88	42.33	0.79	2.53	19.81	50.19	2.48	1.29	6.88
2017	4.30	57.34	21.65	44.97	0.97	2.65	20.55	52.70	2.53	1.34	6.23